Doctoral Dissertation

# Nanofocusing of X-ray Free-Electron Lasers Using Multilayer Kirkpatrick-Baez Mirrors

**Jangwoo Kim**

January 2016

*Department of Precision Science & Technology*

*Graduate School of Engineering*

*Osaka University*

# ABSTRACT

X-ray free-electron lasers (XFELs) produce unprecedented high brilliance, excellent spatial coherence, and ultrafast pulse durations. In recent years, several XFEL facilities have achieved lasing in the hard X-ray regime. The use of focusing optics enables enhancement of X-ray intensity, which expands the range of possible XFEL applications. Several optical devices, such as Fresnel zone plates, refractive lenses, and reflective mirrors, have been utilized for this purpose. Amongst these devices, reflective mirrors can achieve the highest focusing efficiencies with long working distances; therefore, they provide significant advantages for various applications.

The principle aim of the investigation described herein was to generate an extremely intense X-ray field to explore nonlinear phenomena in the hard X-ray regime. To meet this requirement, the usage of an XFEL and its focusing are critically important. To achieve power densities of around $10^{22}$ W/cm$^2$, a XFEL sub-10-nm focusing system was developed in this study using two-stage reflective focusing optics. The development of this system required studies of the fabrication and measurement of mirror substrates with steeply curved surfaces, deposition of multilayers with high reflectivities and sufficient X-ray irradiation tolerances, and techniques for single-shot measurement of focused wavefronts.

XFEL sub-10-nm focusing mirrors have steeply curved surfaces that are difficult to measure using conventional shape testing methods. The minimum radius of curvature is a few meters, and the slope range is several dozen milliradians. Furthermore, the required accuracy, or Rayleigh criterion, of the mirror surface is 1 nm peak-to-valley. A laser autofocus microscope system featuring a position correction mechanism utilizing three heterodyne interferometers was developed to provide measurements at this level of accuracy. This apparatus successfully measured the surface shapes of sub-10-nm focusing mirrors with the accuracy required by the Rayleigh criterion.

In XFEL optical design, the utilization of multilayer mirrors may be considered, since the

grazing incidence angle is much greater than the critical angle at which total reflection occurs. However, one of the critical requirements of the optical elements used in XFELs is sufficient tolerance to intense X-ray irradiation. Therefore, we investigated the X-ray damage thresholds of multilayer films consisting of Pt and C, a suitable combination for this optical design, in grazing incidence conditions. We determined that the threshold value was 0.051 μJ/μm$^2$, which is sufficiently higher than the energy densities that are practically employed. Additionally, the focusing efficiency is related to the X-ray reflectivity of the multilayer film. We improved the X-ray reflectivity of a Pt/C multilayer by approximately 10% through slight C-doping into the Pt layers.

To investigate the focused state of the XFEL nanobeam, a wavefront measurement method was developed, utilizing single-grating interferometry based on the Talbot effect. This method can be used to measure the wavefront phase error, which includes the alignment and surface shape errors of the mirror optics, from a single image. Correct mirror alignment was achieved using this method, and the residual errors could be corrected through deferential deposition with sub-nanometer accuracy.

Use of the above results facilitated initial commissioning of the XFEL sub-10-nm focusing optics at SPring-8 Angstrom Compact free-electron LAser. We found that phase errors of several radians were caused by the shape error of the multilayer mirror, and the focused beam size was approximately 10 nm, which is the smallest reported to date in XFEL focusing. Then, we endeavor to focus the XFEL to sub-10-nm size with a power density greater than $10^{22}$ W/cm$^2$, by using shape-error-corrected multilayer mirrors. Such X-ray field intensities will enable the exploration of nonlinear phenomena in the hard X-ray regime.

# ACKNOWLEDGEMENT

Completing this Ph.D. has been a collaborative process, and I would like to thank the following people for their gracious help and support.

First and foremost, I would like to express sincere gratitude to my supervisor Prof. Kazuto Yamauchi of Osaka University for his advice, constant support, and encouragement throughout the course of my studies. I would also like to express my great appreciation to Assist. Prof. Satoshi Matsuyama, Assoc. Prof. Yasuhisa Sano, and Assoc. Prof. Yukio Takahashi of Osaka University for their suggestions and discussions. I would additionally like to thank Prof. Kiyoshi Yasutake, Prof. Mizuho Morita, Prof. Yuji Kuwahara, Prof. Yoshitada Morikawa, Prof. Heiji Watanabe, and Prof. Katsuyoshi Endo, and all of the other professors and technicians of the Department of Precision Science & Technology, Osaka University.

I would like to express my sincere acknowledgements to Director Dr. Tetsuya Ishikawa, Group Director Dr. Makina Yabashi, Team Leader Dr. Kenji Tamasaku, Unit Leader Dr. Yoshiki Kohmura, and Researcher Dr. Yuichi Inubushi of the RIKEN SPring-8 Center (RSC), and Division Director Dr. Shunji Goto, Group Reader Dr. Haruhiko Ohashi, Team Reader Dr. Kensuke Tono, and Researcher Dr. Takahisa Koyama, Dr. Hirokatsu Yumoto, and Dr. Yasunori Senba of the Japan Synchrotron Radiation Research Institute (JASRI), for their valuable and effective advice and suggestions in preparing this thesis.

In particular, I would like to express my gratitude to Prof. Hidetsugu Yagi of Ehime University for his guidance and encouragement throughout my overseas studies in Japan. I would also like to express my appreciation to Prof. Keiji Ogi of Ehime University for his advice throughout my undergraduate years.

I am grateful to Ayaka Nagahira, Hikaru Yokoyama, Ryosuke Fukui, Akihiko Nishihara, and Shogo Kawai of the X-ray focusing group, and all the members of Ultra-Precision Machining Laboratory. Also, I am grateful to the secretaries; Yumiko Tachibana, Eriko Kubo, and Kanako Terai for their administrative and clerical support. I also heartily thank Ph.D.

candidate Taito Osaka and Ph.D. candidate Akihiro Suzuki for their friendship, kindness, support, and encouragement during our time studying together.

I would like to express appreciation to JTEC Corporation, Motion Trust Co., Ltd., and Mitaka Kohki Co., Ltd. for developing surface shape measurement system.

This research was mainly supported by a Grant-in-Aid for Scientific Research (S) no. 2322604, a Grant-in-Aid for JSPS Fellows no. 25-129, and the Global COE program (H08) from the Ministry of Education, Sport, Culture, Science and Technology, Japan. It was also supported by CREST from the Japan Science and Technology Agency. The use of BL29XUL at SPring-8 and BL3 at SPring-8 Angstrom Compact free-electron LAser (SACLA) was supported by RSC and JASRI. I am grateful to the staff at SPring-8 and SACLA beamline for their help during the beam time. I also heartily appreciate scholarships granted by Korea-Japan Joint Government Scholarship Program and Kato Asao International Scholarship Foundation.

Finally, I would like to express my gratitude to my family for their lasting love and support. In particular, I would like to thank my lovely wife and my cute daughter for always being there for me, and for helping me improve. Without their love and support, I would not be here completing this study. Thank you for being there.

**Jangwoo Kim**

January 2016

# CONTENTS

# LIST OF FIGURES

# LIST OF TABLES

# Chapter 1

# INTRODUCTION

In 1895, a new form of radiation was discovered by W. C. Röntgen [1], when he experimentally discharged a Crookes tube [2] to produce radiation of a wavelength that had not been observed previously. This new radiation was subsequently named “X-ray” to signify its unknown nature. Röntgen went on to research his discovery further and was able to ascertain some of the typical characteristics of X-rays, such as their deep penetration abilities, their fluorescence, and that their trajectories are unaffected by electric and magnetic fields. Then, in 1912, M. von Laue discovered the diffraction of X-rays by atoms in a crystal structure [3,4]. Moreover, in 1913, W. H. Bragg and W. L. Bragg observed the diffraction of X-rays by crystal planes and determined the relationship between X-ray reflection angle and crystal lattice spacing, called Bragg’s law [5]. Since these discoveries, X-rays have played important roles in a wide range of scientific fields, including the physical sciences, the medical sciences, and engineering. In the fields of materials and life sciences, the high penetration of X-rays through materials and their mutual interactions with crystals and atoms have been effectively utilized, and they have been instrumental in groundbreaking discoveries such as that of the double helix structure of DNA [6]. Consequently, X-rays are widely recognized as irreplaceable analytical tools.

However, X-ray sources remained essentially explored until the 1960s. Synchrotron radiation was theoretically predicted in 1946 [7] and was observed using an electron accelerator in 1947 [8]. However, at that time, synchrotron radiation, which was produced by first-generation facilities, was considered to be only the energy lost from accelerators in elementary particle experiments. In the 1970s, a second-generation synchrotron radiation facility was built, which was designed primarily as an X-ray source. It was then found that synchrotron radiation is much more powerful and more widely applicable than radiation from conventional X-ray

sources.

In recent years, various advanced analytical technologies have been developed by utilizing the high-brilliance and low-emittance properties of third-generation synchrotron radiation sources [9], which began operation in the 1990s. The increase in the peak brilliances of the X-ray sources over time is shown in Fig. 1.1. The development of X-ray free-electron lasers (XFELs) [9] is expected to enable further advances in the field of X-ray analytical technology. High-brilliance X-ray sources are effective for providing high photon densities at their focal points and can yield both high spatial resolution and high throughput when used in scanning-type X-ray microscopes. Therefore, the competition to improve focusing states via advances in optical element performance has intensified since the 2000s, and the use of Fresnel zone plates, refractive lenses, reflective mirrors, and various other X-ray optical elements has yielded focus spot sizes of 100 nm or less [10–16]. Of these optical elements, mirrors greatly surpass the others due to their high focusing efficiencies, long working distances, and small chromatic aberrations. Furthermore, since ablation damage induced by intense X-rays, such as those

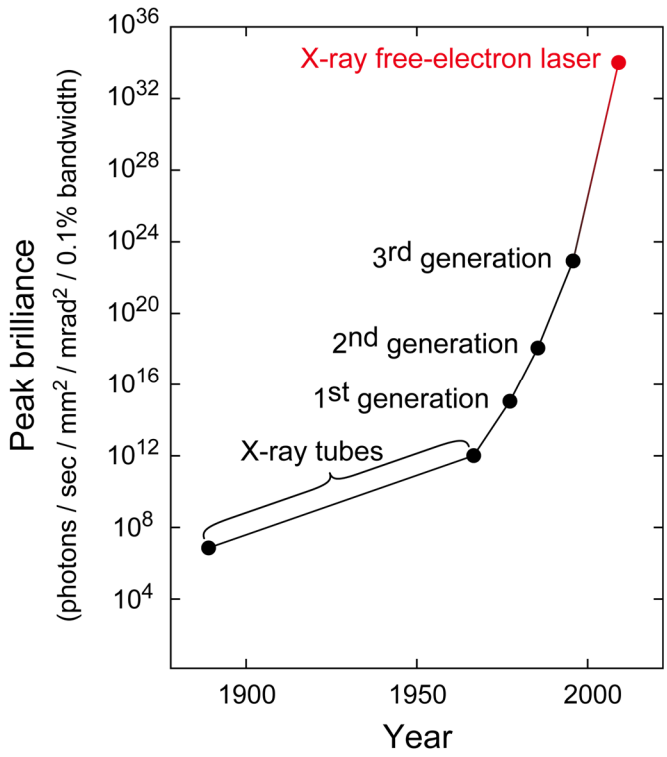


Fig. 1.1. Peak brilliances of X-ray sources.

produced by XFELs, cannot be avoided in normal incidence optical elements, the use of mirrors in grazing incidence optics is advantageous.

The principle aim of this study was to generate an extremely intense X-ray field to explore nonlinear phenomena in the hard X-ray regime. To meet this requirement, the usage of an XFEL and the control of its focusing are critically important. In SPring-8 Angstrom Compact free electron LAser (SACLA) [17], a 50 nm focusing beam with a power density of $10^{20}$ W/cm$^2$ has been achieved using total reflection mirror optics [18]. This focused beam has been applied to studies of nonlinear X-ray optical phenomena such as two-photon absorption [19], saturable absorption [20], and Cu-atomic inner-shell lasers [21]. To achieve higher power densities of around $10^{22}$ W/cm$^2$, XFEL sub-10-nm focusing is needed. With the objective of developing such a focusing system, we performed studies of the fabrication and measurement of mirror substrates with steeply curved surfaces, deposition of multilayers with high reflectivities and sufficient X-ray irradiation tolerances, and development of a technique for single-shot measurement of focused wavefronts.

The remainder of this thesis is organized as follows.

In Chapter 2, the fundamentals of reflective X-ray focusing optics are described. The focal spot sizes achievable by reflective optics, the limitations of total reflection, and the need for multilayer films to overcome their limitations are described. Then, the existing reflective XFEL focusing optics at SACLA are introduced.

In Chapter 3, the mirror substrate fabrication and measurement methods used to produce the sub-10-nm focusing mirrors for this study are described. To create the desired mirror shapes accurately, precise shape measurements were necessary; therefore, a new measurement system was developed, as explained in this chapter.

In Chapter 4, the thin film deposition system developed to fabricate Pt/C multilayers and its tolerance to XFEL irradiation are described. Then, evaluations of the Pt/C multilayers obtained using focused and unfocused XFEL beams are described.

In Chapter 5, various methods of improving the reflectivities of Pt/C multilayers are discussed, and the results of Pt layer thinning and C-doping tests are presented.

In Chapter 6, XFEL sub-10-nm focusing optics and focusing strategies are described, and the wavefront measurement method developed to examine the focused state of the XFEL nanobeam is discussed. The results of using this method for accurate mirror alignment and the

measured residual surface shape errors of the mirror optics are presented. Then, the initial commissioning of the XFEL sub-10-nm focusing optics at SACLA is described.

Finally, in Chapter 7, the conclusions of this study are summarized.

# Chapter 2

# REFLECTIVE FOCUSING OPTICS FOR X-RAY FREE-ELECTRON LASERS

*XFELs produce unprecedented high brilliance, excellent spatial coherence, and ultrafast pulse duration. The Linac Coherent Light Source [22] in the USA and SACLA [17] in Japan have recently achieved lasing in the hard X-ray regime. Additional hard XFEL facilities are under construction in many countries, e.g., the European XFEL in Germany, the Pohang Accelerator Laboratory XFEL in South Korea, and the SwissFEL in Switzerland. These X-ray sources, in conjunction with analysis methods, provide unique capabilities, and their application to exploring new frontiers of science can be advanced by using focusing optics.*

## 2.1 X-ray Focusing with Reflective Optics

The use of focusing optics enables further enhancement of X-ray intensity, expanding the range of applications of XFELs. Several optical focusing devices, such as Fresnel zone plates [23,24], refractive lenses [25], and reflective mirrors [18,26], have been utilized in XFEL facilities. Amongst these, reflective mirrors achieve the highest focusing efficiencies with long working distances; therefore, they provide significant advantages in various applications. In this section, X-ray focusing with reflective optics and the focal spot sizes achievable by using this method are described.

X-rays are high-frequency electromagnetic waves. Therefore, the diffraction-limited focal

spot size $D$ of an X-ray beam, based on Fraunhofer diffraction theory [27], is given by

$$D = \frac{\lambda}{2NA}, \tag{2.1}$$

in the case of a rectangular aperture, where $\lambda$ and $NA$ are the X-ray wavelength and numerical aperture of the incoming beam, respectively. $NA$ is given by

$$NA = n\sin\theta, \tag{2.2}$$

where $\theta$ and $n$ are the convergent angle of the incoming beam and the refractive index ($n \leq 1$ usually in the X-ray regime), respectively. If the spot size is defined by the full width at half maximum (FWHM) of the intensity on the focal plane, the spot size $D_{\mathrm{FWHM}}$ is given by

$$D_{\mathrm{FWHM}} = 0.44\frac{\lambda}{NA}. \tag{2.3}$$

The essential lower limit of the spot size is comparable to $\lambda$, since $NA$ is generally smaller than 1.

However, large convergent angles, $NA \approx 1$, are currently impossible to attain in the X-ray regime, since transmission without reflection occurs when the incidence angle becomes large. Therefore, the fundamental upper limit of $NA$ is severely restricted by the effective value of $NA$, which is optical-element dependent. Attempts to estimate the theoretically available lower limit of the focal spot size, *i.e.*, the upper limit of $NA$, in diffraction-limited conditions have been reported. For example, in the Kirkpatrick–Baez (KB) optical system [28] (see Fig. 2.1), which is the typical X-ray reflective focusing system, the upper limit of $NA$ is the equivalent to the critical angle of the surface material of the total reflection mirror. Therefore, $D$ is given by

$$D \geq \frac{\lambda}{2\theta_{\mathrm{c}}}, \tag{2.4}$$

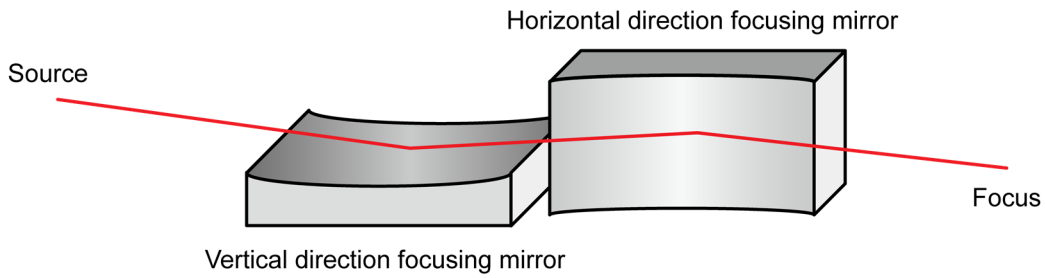


Fig. 2.1. Schematic of KB mirror geometry, where two concave mirrors are arranged orthogonally.

since the critical grazing incidence angle is sufficiently small, $\sin\theta_c \approx \theta_c$. In the total reflection condition, $\theta_c$ is restricted by the surface material. Even for high-density materials, such as Pt (21.45 g/cm$^3$), $\theta_c$ is only 8 mrad at a photon energy of 10 keV. In contrast, employing a multilayer coating enables the use of a large grazing incidence angle 3–4 times larger than the critical angle at which total reflection occurs, thus allowing spot sizes 3–4 times smaller according to Eq. (2.4).

The geometry of an ellipsoidal focusing mirror is depicted in Fig. 2.2, showing that the two focal points of the ellipse become the source and the focus. Typically, the major and minor axes are several tens of meters and several tens of millimeters long, respectively. The grazing incidence angle on the optical axis is $\theta_2$, with $\theta_1 \sim \theta_3$, where $\theta_1 < \theta_3$.

A schematic of a multilayer mirror, and the difference between the total reflection condition of a single-layer mirror and the Bragg refraction condition of a multilayer mirror, are shown in Fig. 2.3. If the influence of refraction is ignored, the shape of each interface of the multilayer film follows part of the ellipse, each with a slightly different eccentricity. Moreover, to design multilayer mirrors, it is necessary for the difference of each optical path to be an integral multiple of the X-ray wavelength. The light impinging on each interface will then be reflected towards the focal point, and the ideal diffraction-limited focusing conditions, such as constructive interference at the focal point, will be satisfied. The multilayer period is non-uniform at each point on the mirror surface since the incidence angle changes, resulting in a laterally graded multilayer mirror. The advantage of replacing the single-layer mirror with a multilayer mirror is the large convergent angle of the incident X-rays, as shown in Fig. 2.3(b).

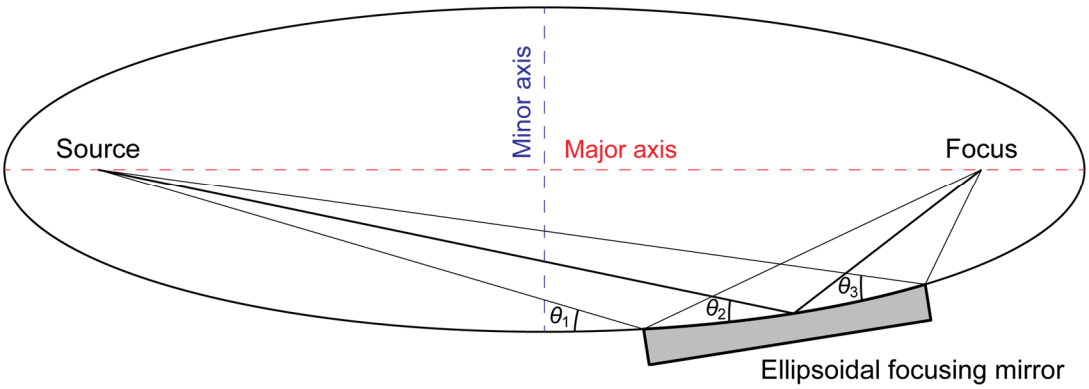


Fig. 2.2. Ellipsoidal focusing mirror geometry.

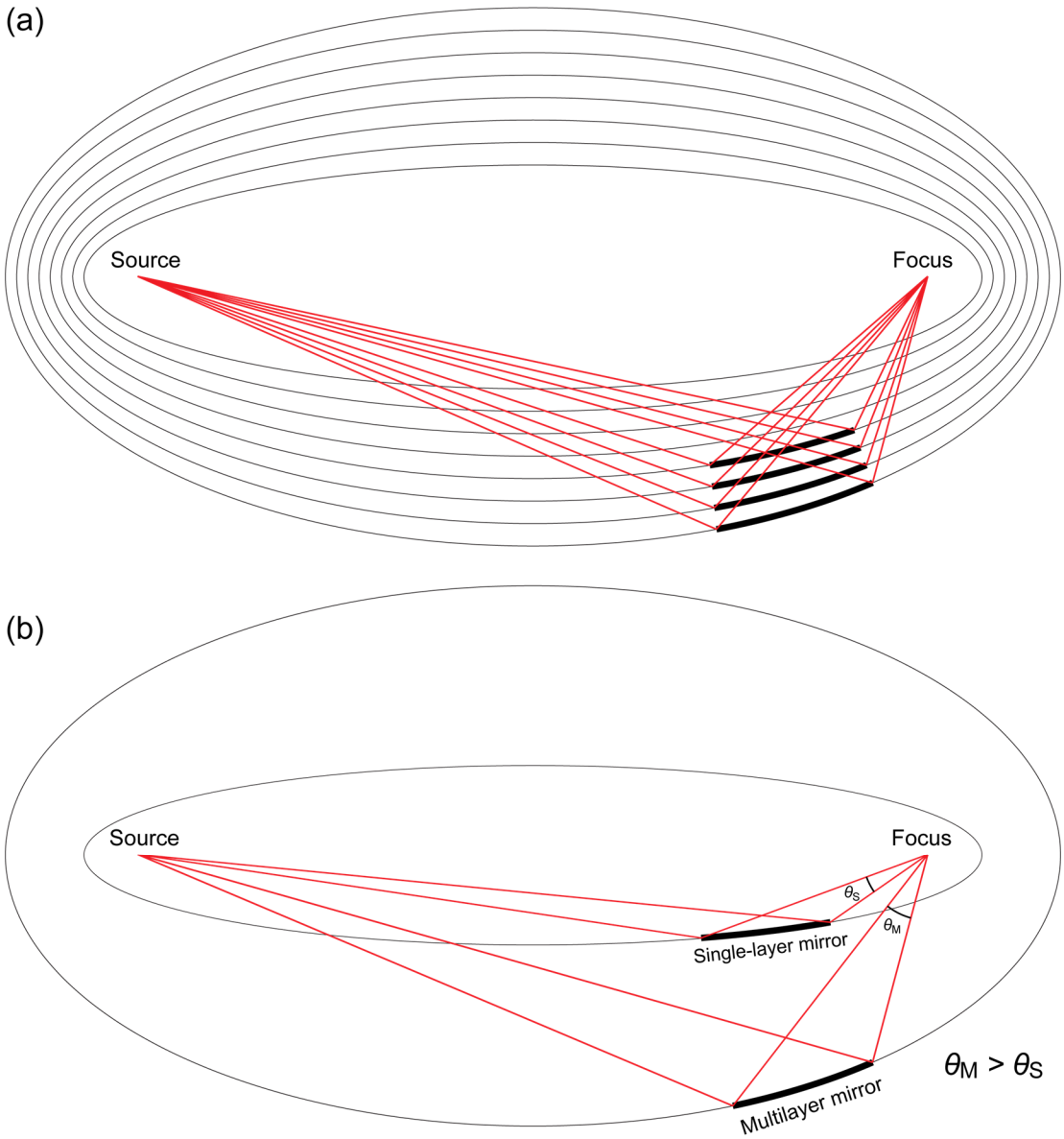


Fig. 2.3. (a) Multilayer mirror schematic: thick black lines represent multilayer interfaces. (b) Differences between total reflection from single-layer mirror and Bragg reflection from multilayer mirror.

## 2.2 Multilayer Films for X-ray Focusing

A multilayer film is an X-ray optical element utilizing Bragg diffraction from an artificial periodic structure consisting of alternating layers of two or more optically dissimilar components. Bragg diffraction from the constructive interference of the multilayer film can occur at large grazing incidence angles, which are sufficiently larger than the critical angle at which total reflection occurs.

X-rays can penetrate substances easily when the incidence angle is larger than the critical angle. Therefore, periodically layered structures inside the material will cause reflected waves to interfere with each other. When the optical path difference between the reflected waves is equal to an integer multiple of the wavelength, a high reflectivity will be obtained. This condition is Bragg's law [5] and can be written as

$$m\lambda = 2d\sin\theta\,, \tag{2.5}$$

where $m$, $\lambda$, $d$, and $\theta$ are the Bragg index, incident X-ray wavelength, multilayer period, and grazing incidence angle, respectively. Considering refraction inside the materials, Eq. (2.5) can be written as

$$m\lambda = 2d\sin\theta_m\sqrt{1-\frac{2\delta-\delta^2}{\sin^2\theta_m}}\,, \tag{2.6}$$

where $\theta_m$ is the $m$th-order grazing incidence Bragg angle, and $\delta$ is the real part of the complex refractive index $n$. Equation (2.7) defines $n$ to be

$$n = 1-\delta-i\beta\,, \tag{2.7}$$

where $\delta$ and $\beta$ are related to the real (refraction) and imaginary (absorption) parts of $n$, respectively, and are given by

$$\delta = \frac{r_e\lambda^2 N_A\rho_m f_1}{2\pi A} \tag{2.8}$$

and

$$\beta = \frac{r_e\lambda^2 N_A\rho_m f_2}{2\pi A}\,, \tag{2.9}$$

where $r_e$, $N_A$, $\rho_m$, and $A$ are the classical electron radius, Avogadro's constant, the material density, and the atomic weight, respectively. The variables $f_1$ and $f_2$ represent the real and

imaginary parts of the anomalous dispersion factors, respectively.

Multilayer films have artificial periodic structures, consisting of alternating layers of two optically dissimilar components. A material with a high atomic number (Z) is used to obtain a high reflectivity, and a low-Z material is used as the spacer. Various material combinations have been researched for use as focusing mirrors and monochromators in the hard X-ray regime. Predominately, Cr, Ni, Mo, W, and Pt have been used as high-Z materials, while $B_4C$, C, and Si have been used as low-Z materials [29–38]. In this study, Pt was used as the high-Z element because it exhibits adequate reflectivity and chemical stability, and C was used as the low-Z element because it possesses sufficiently low absorptivity in the hard X-ray regime and is resistant to thermal interdiffusion.

A brief theoretical background of X-ray reflection and X-ray standing waves (XSWs) in a periodical multilayer is as follows. The multilayer structure consists of $N$ bilayers of alternating high- and low-$Z$ materials, as shown in Fig. 2.4. A plane electromagnetic wave of frequency $\omega$ in the $j$th layer of a medium, at a position $\boldsymbol{r}$, can be described by [39]

$$\boldsymbol{E}_j(\boldsymbol{r}) = E_j \exp\left[-i\left(\boldsymbol{k}_j \cdot \boldsymbol{r} - \omega t\right)\right], \tag{2.10}$$

where $E_j$ is the field amplitude at the top of the $j$th layer, and $\boldsymbol{k}_j$ is the wave vector in the material of the $j$th layer. The $z$-component of the wave vector is given by

$$k_{jz} = \frac{2\pi}{\lambda}\sqrt{\varepsilon_j - \cos^2\theta}\,, \tag{2.11}$$

where $\theta$ is the grazing incidence angle, and $\lambda$ is the incident X-ray wavelength. The dielectric function in the $j$th layer, $\varepsilon_j$, is given by

$$\varepsilon_j = 1 - 2\delta_j - i2\beta_j\,. \tag{2.12}$$

Here, $\delta_j$ and $\beta_j$ are the real and imaginary parts of the complex refractive index of the $j$th layer, respectively.

In the X-ray regime, there is no significant difference between $s$ and $p$ polarizations [40]; thus, the expression for $s$ polarization can be adopted. The Fresnel equations for the reflection and transmission coefficients, $r_j$ and $t_j$, respectively, at the interface between layers $j$ and $j$+1 are given by

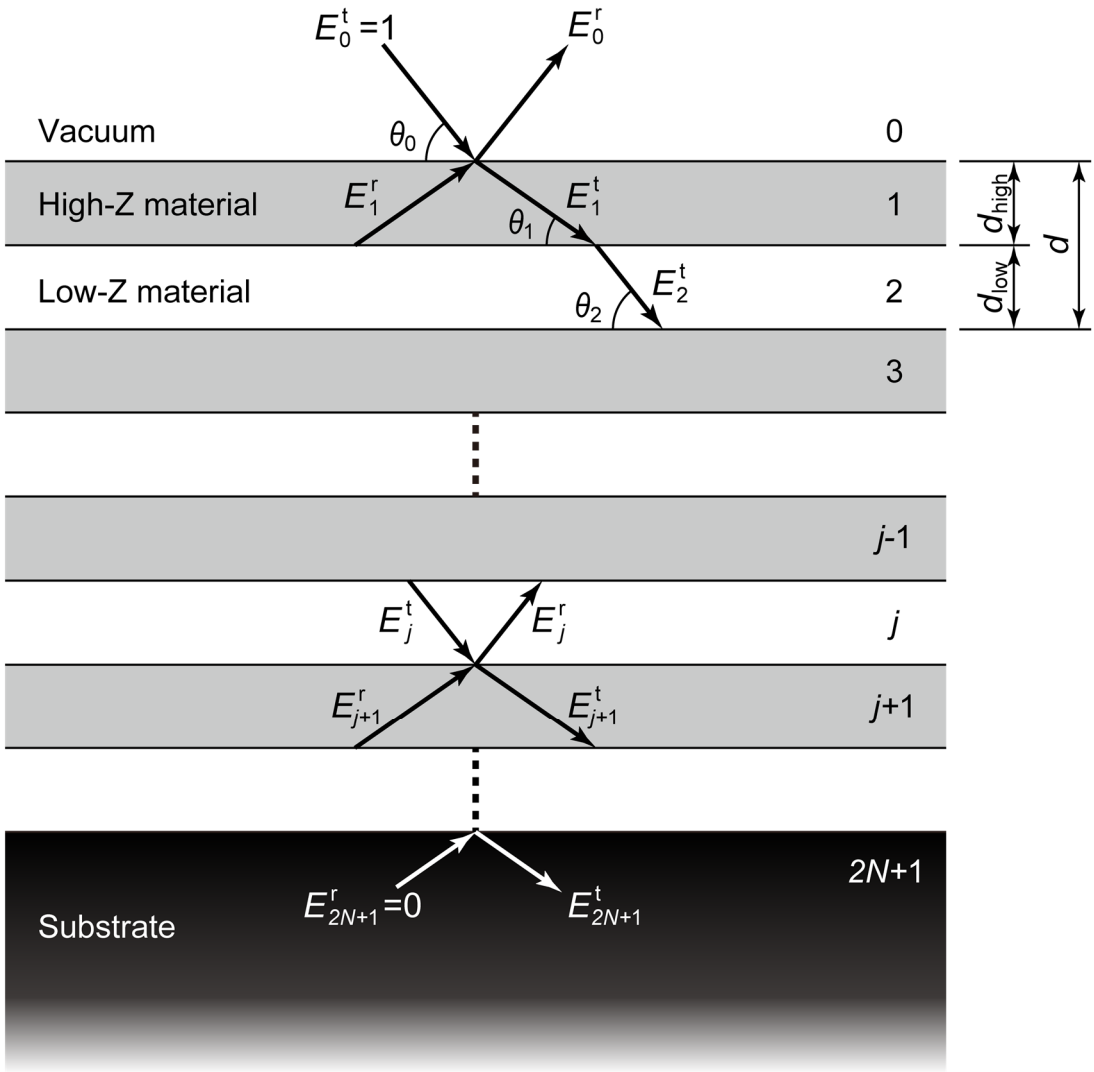


Fig. 2.4. Schematic of transmitted ($E^t$) and reflected ($E^r$) plane electromagnetic waves inside multilayer.

$$r_j = \frac{k_{jz} - k_{j+1,z}}{k_{jz} + k_{j+1,z}} \tag{2.13}$$

and

$$t_j = \frac{2k_{jz}}{k_{jz} + k_{j+1,z}}. \tag{2.14}$$

An expression to consider attenuation due to the interface roughness $\sigma_j$, the root-mean-square (RMS) deviation at the interface of layers $j$ and $j$+1, was previously derived [41,42]. Here, $r_j$ and $t_j$ are multiplied by factors $S_j$ and $T_j$, respectively, which are given by

$$S_j = \exp\left[-2\sigma_j^2 k_{jz} k_{j+1,z}\right] \tag{2.15}$$

and

$$T_j = \exp\left[\sigma_j^2 \left(k_{jz} - k_{j+1,z}\right)^2 / 2\right]. \tag{2.16}$$

The behavior of electromagnetic waves in a multilayer system consisting of multiple interfaces can be calculated by recursive [40,43] or matrix [42] methods. In the following derivation, the recursive method is used. The amplitudes of the transmitted and reflected plane waves at the top of the $j$th layer, $E^{\mathrm{t}}_j$ and $E^{\mathrm{r}}_j$, respectively, are given by

$$E^{\mathrm{r}}_j = \exp\left[-2ik_{jz}d_j\right] A_j E^{\mathrm{t}}_j \tag{2.17}$$

and

$$E^{\mathrm{t}}_{j+1} = \frac{\exp\left[-ik_{jz}d_j\right] E^{\mathrm{t}}_j t_j T_j}{1 + \exp\left[-2ik_{j+1,z}d_{j+1}\right] A_{j+1} r_j S_j}, \tag{2.18}$$

where

$$A_j = \frac{r_j S_j + \exp\left[-2ik_{j+1,z}d_{j+1}\right] X_{j+1}}{1 + \exp\left[-2ik_{j+1,z}d_{j+1}\right] A_{j+1} r_j S_j} \tag{2.19}$$

and $d_j$ is the thickness of the $j$th layer.

The X-ray reflectivity $R$ can be calculated from the ratio of the field amplitudes at the sample surface:

$$R(\theta)=\left|\frac{E_0^{\mathrm{r}}}{E_0^{\mathrm{t}}}\right|^2. \tag{2.20}$$

The XSW field intensity at each interface of the multilayer can be obtained using Eqs. (2.17)–(2.19), and the inside of the $j$th layer can be interpolated to be an interface between the transmitting and reflecting plane waves as [44,45]

$$I(\theta,z)=\left|E_j^{\mathrm{t}}\right|^2\exp\left[-2k_{jz}''z\right]+\left|E_j^{\mathrm{r}}\right|^2\exp\left[2k_{jz}''z\right]+2\left|E_j^{\mathrm{t}}\right|\left|E_j^{\mathrm{r}}\right|\cos\left(\nu+2k_{jz}'z\right), \tag{2.21}$$

where $z$ and $\nu$ are the depth from the top of the $j$th layer and the phase difference between $E^{\mathrm{r}}_j$ and $E^{\mathrm{t}}_j$, respectively. The variables $k'_{jz}$ and $k''_{jz}$ are the real and imaginary parts of the component $k_{jz}$, respectively.

The calculated X-ray reflectivities and XSW field intensities of the Pt/C multilayers are shown in Figs. 2.5–2.7 and Fig. 2.8, respectively, for an X-ray photon energy of 10 keV ($\lambda$ = 0.124 nm). The X-ray reflectivities were calculated as functions of three quantities: the grazing incidence angle (Fig. 2.5); $\gamma$ (= $d_{\mathrm{high}}/d$), the ratio of the thickness of the high-Z layer to the total thickness of the bilayer (Fig. 2.6); and the multilayer period (Fig. 2.7). In Fig. 2.5, it can be seen that high reflectivity peaks were obtained in the Bragg condition (Eq. (2.6)). The vibrations of the reflected intensity, which are called Kiessig fringes [46], enable determination of the

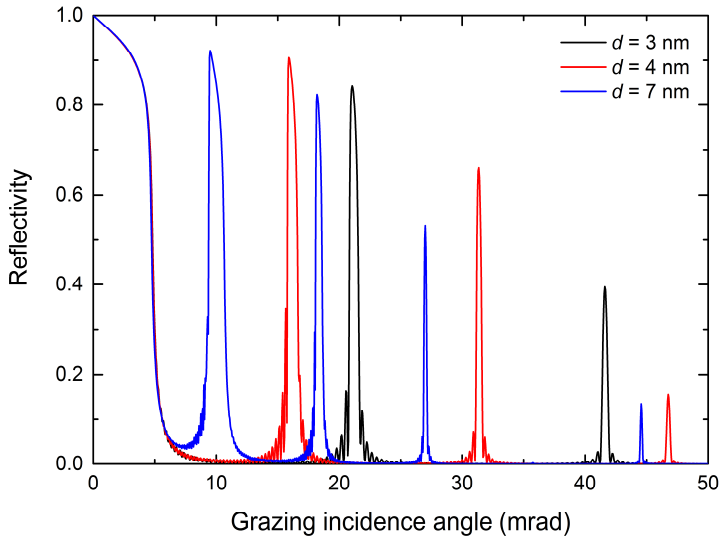


Fig. 2.5. Calculated X-ray reflectivities versus grazing incidence angle (fixed parameters $\gamma$ = 0.25, $N$ = 50).

thickness of the multilayer period. In Fig. 2.6, the $\gamma$ range from 0.2 to 0.5 is optimal for the first-order Bragg diffraction, with a small dependence on $N$. For the second-order diffraction, the reflectivity is approximately 0 at $\gamma = 0.5$. The XSW field intensities were calculated as functions of the grazing incidence angle and the depth of the multilayer medium, as shown in Fig. 2.8.

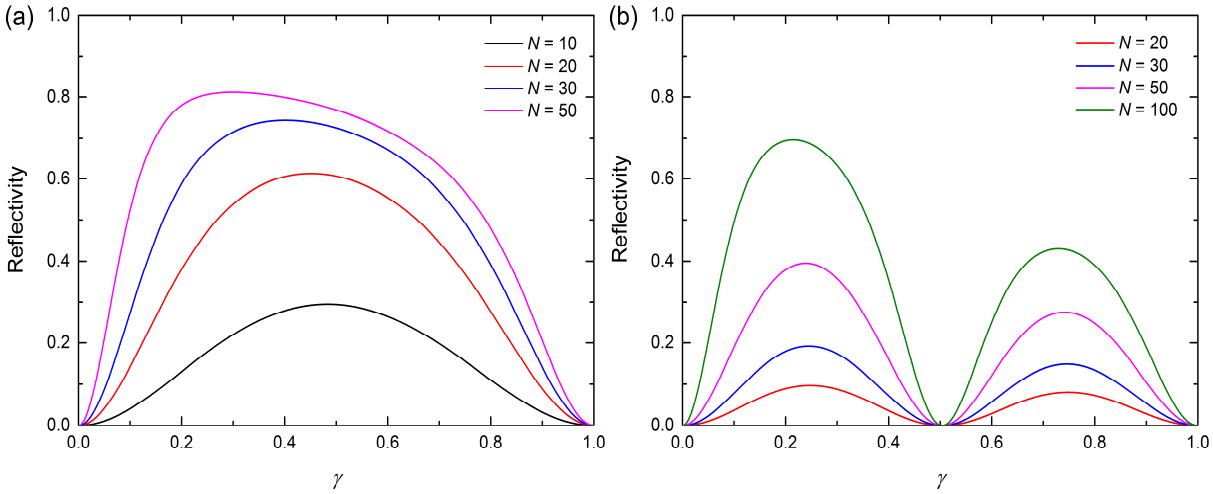


Fig. 2.6. Calculated X-ray reflectivities of (a) first- and (b) second-order Bragg diffractions versus $\gamma$ (fixed parameter $d$ = 3 nm).

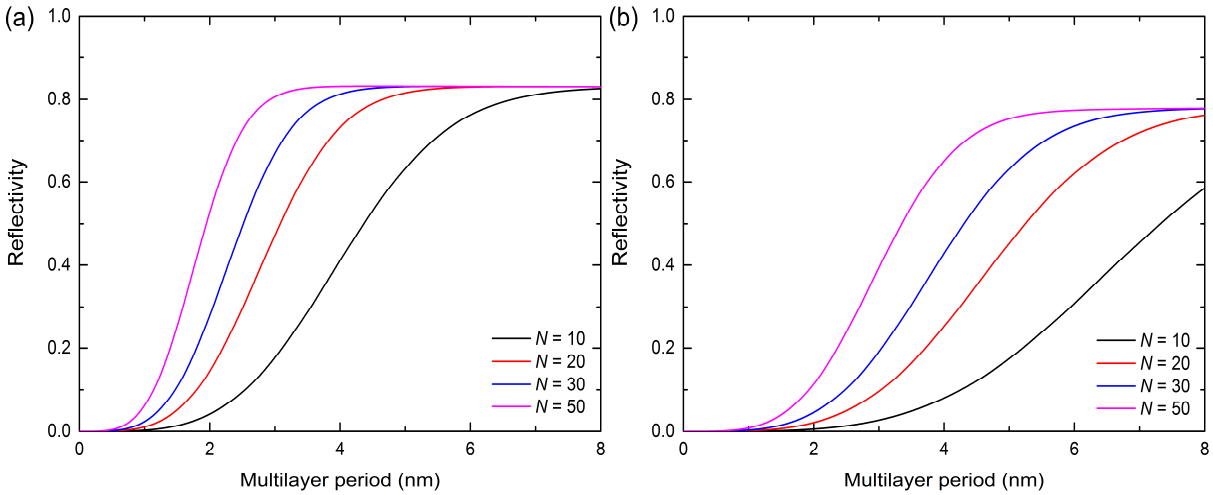


Fig. 2.7. Calculated X-ray reflectivities of (a) first- and (b) second-order Bragg diffractions versus multilayer period (fixed parameter $\gamma = 0.25$).

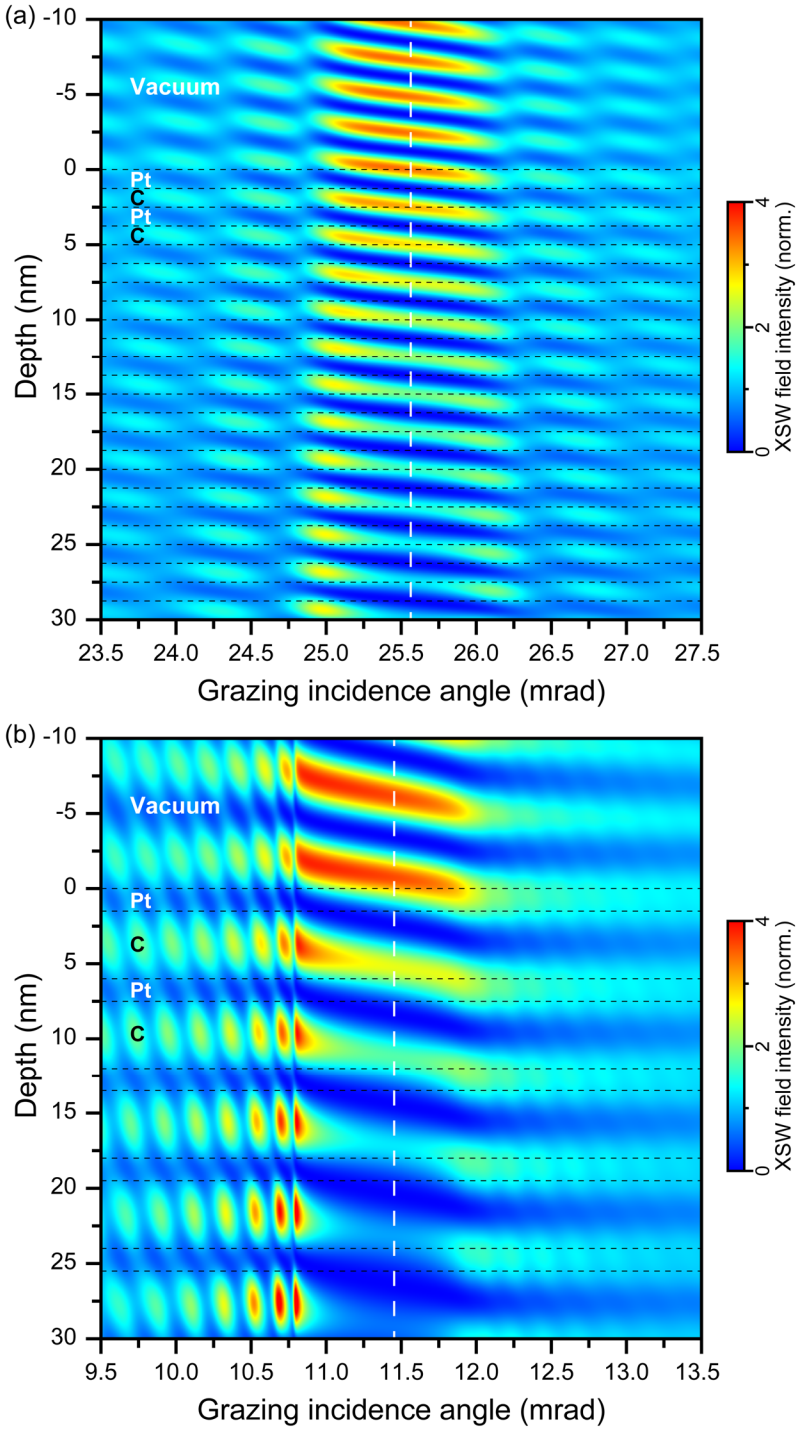


Fig. 2.8. Calculated XSW field-intensity distributions in multilayer structure, as functions of grazing incidence angle and depth of multilayer medium. Dashed white lines represent first-order Bragg angle. (a) $d = 2.5$ nm, $\gamma = 0.5$, $N = 40$; (b) $d = 6$ nm, $\gamma = 0.25$, $N = 40$.

## 2.3 Reflective Focusing Optics Used at SACLA

At SACLA, 1 μm [26] and 50 nm [18] XFEL focusing has previously been demonstrated by utilizing total reflection focusing mirrors. The schematics of the optical configurations and the optical design parameters used to obtain 1 μm and 50 nm focusing are shown in Fig. 2.9 and Table 2.1 and in Fig. 2.10 and Table 2.2, respectively.

The 1 μm focusing system [26] realized an FWHM beam size of 0.95 μm (horizontal direction, H) × 1.20 μm (vertical direction, V), at a photon energy of 10 keV. The photon flux density of the focused beam was $4 \times 10^4$ times higher than that of the unfocused beam. A peak power density of $6 \times 10^{17}$ W/cm$^2$ was achieved, at a pulse energy of 98 μJ and a pulse duration of 20 fs [47]. To reduce XFEL-induced irradiation damage, sufficiently long mirror substrates and small grazing incidence angles were utilized. The mirror surfaces were coated with 50 nm of C so that they would be highly reflective, since C and quartz have reflectivities of approximately 99.9% and 99%, respectively, up to photon energies of 20 keV. The resulting high-intensity focused beams are appropriately sized for various applications, such as X-ray coherent diffraction imaging [48–51] and observations of other physical phenomena [52,53].

The 50 nm focusing system [18] realized an FWHM beam size of 55 nm (H) × 30 nm (V) at a photon energy of 9.9 keV. The peak power density achieved was $1.2 \times 10^{20}$ W/cm$^2$, which is 200 times higher than that of the 1 μm focused beam, at a pulse energy of 11 μJ and a pulse duration of 7 fs [47]. To obtain a large NA, and a long working distance with small beam divergence, a two-stage reflective focusing system was used. In the first (upstream) stage, an uncoated total reflection KB mirror was used for beam expansion. In the second (downstream) stage, a single-layer metal-coated KB mirror focused the expanded beam. Beams focused using this method have been applied to studies of nonlinear X-ray optical phenomena, such as two-photon absorption [19], saturable absorption [20], and Cu-atomic inner-shell lasers [21].

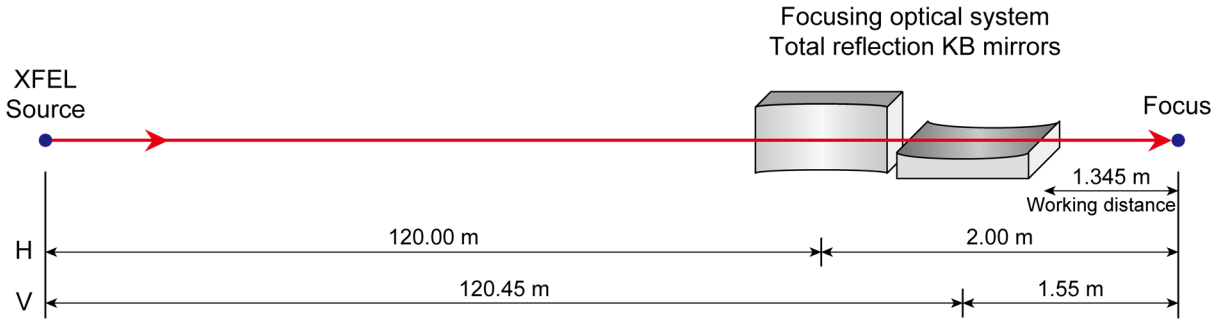


Fig. 2.9. Schematic of optical configuration of XFEL 1 μm focusing system at SACLA.

Table 2.1. Optical parameters of XFEL 1 μm focusing system at SACLA.

| | **Vertical direction focusing mirror** | **Horizontal direction focusing mirror** |
|---|---|---|
| Surface shape | Elliptical cylinder | Elliptical cylinder |
| Substrate material | Quartz | Quartz |
| Coating material | Carbon | Carbon |
| Coating thickness (nm) | 50 | 50 |
| Substrate size ($mm^3$) | 420 × 50 × 50 | 420 × 50 × 50 |
| Grazing incidence angle on mirror center (mrad) | 1.55 | 1.50 |
| Focal length (m) | 2.00 | 1.55 |
| Distance from source (m) | 120.00 | 120.45 |
| Semi-major axis (m) | 51 | 51 |
| Semi-minor axis (mm) | 21.9 | 18.7 |

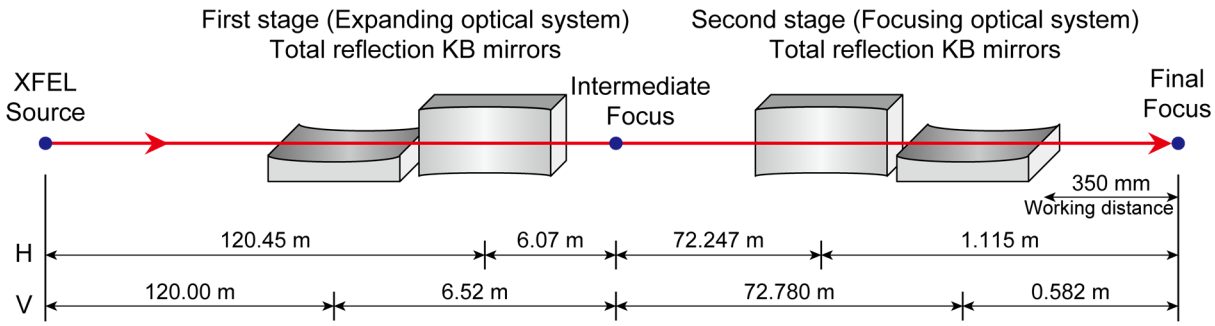


Fig. 2.10. Schematic of optical configuration of XFEL 50 nm focusing system at SACLA.

Table 2.2. Optical parameters of XFEL 50 nm focusing system at SACLA.

| | **Upstream focusing mirrors** | | **Downstream focusing mirrors** | |
|---|---|---|---|---|
| | **Vertical direction** | **Horizontal direction** | **Horizontal direction** | **Vertical direction** |
| Surface shape | Elliptical cylinder | Elliptical cylinder | Elliptical cylinder | Elliptical cylinder |
| Substrate material | Quartz | Quartz | Quartz | Quartz |
| Coating material | None | None | Platinum | Platinum |
| Coating thickness (nm) | None | None | 50 | 50 |
| Substrate size ($mm^3$) | 400×50×50 | 400×50×50 | 500×50×50 | 465×50×50 |
| Grazing incidence angle on mirror center (mrad) | 1.5 | 1.5 | 5.5 | 5.0 |
| Focal length (m) | 6.520 | 6.070 | 1.115 | 0.582 |
| Distance from source (m) | 120.00 | 120.45 | 72.247 | 72.780 |
| Semi-major axis (m) | 120.000 | 120.450 | 36.68 | 36.68 |
| Semi-minor axis (mm) | 42.0 | 40.6 | 49.4 | 32.6 |

# Chapter 3

# PREPARATION AND MEASUREMENT OF MIRROR SUBSTRATES

*Mirrors are among the most widely used optical devices, and the surface shape of a mirror significantly affects the quality of X-rays at the sample position. Planar or nearly planar surfaces can be measured using interferometry (e.g., microstitching interferometry (MSI) [56] and relative-angle determinable-stitching interferometry (RADSI) [57,58]), slope profilers (e.g., long trace profilers (LTPs) [59,60] and nanometer optical component measuring machines (NOMs) [61]), and coordinate measuring machines (CMMs) [62]. However, the focusing mirrors used for soft X-ray focusing and single-nanometer hard X-ray focusing have minimum radii of curvature of a few meters. Thus, it is difficult to measure the surfaces of these mirrors using conventional methods. We developed a new measurement system that uses a laser autofocus microscope as a probe to measure steeply curved mirrors.*

## 3.1 Reflective Mirrors for XFEL Focusing

Reflective mirrors are the most widely used optical elements in synchrotron radiation facilities and are employed to collimate and focus X-rays and to filter high-order light frequencies. The shapes of X-ray mirrors must be more accurate than those of visible light mirrors because X-rays have wavelengths much shorter than those of visible lights. Mirror surface shape errors are the factors that most significantly degrade the focusing of X-rays. The phase error $\varphi$ of a

reflected X-ray that originates from the shape error is

$$\varphi = 2hk\sin\theta, \tag{3.1}$$

where $h$ and $\theta$ are the peak-to-valley (PV) height shape errors of the mirror surface and the grazing incidence angle, respectively, and $k$ is the X-ray wavenumber, which is given by

$$k = \frac{2\pi}{\lambda}, \tag{3.2}$$

where $\lambda$ is the X-ray wavelength. The degree of constructive interference is significantly influenced by the phase error. According to Rayleigh's criterion [27], an image is not significantly degraded unless it has wavefront aberration of greater than $\lambda/4$ in the imaging optical system. The height error of a mirror surface corresponding to a $\lambda/4$ phase error (*i.e.* $\pi/2$ rad) is

$$h_{\lambda/4} = \frac{\lambda}{8\sin\theta}. \tag{3.3}$$

For example, in the case of an X-ray wavelength of 0.124 nm (*i.e.*, a photon energy of 10 keV), the required shape accuracy is as shown in Fig. 3.1.

The required shape accuracies of the 1 μm and 50 nm focusing mirrors whose optical

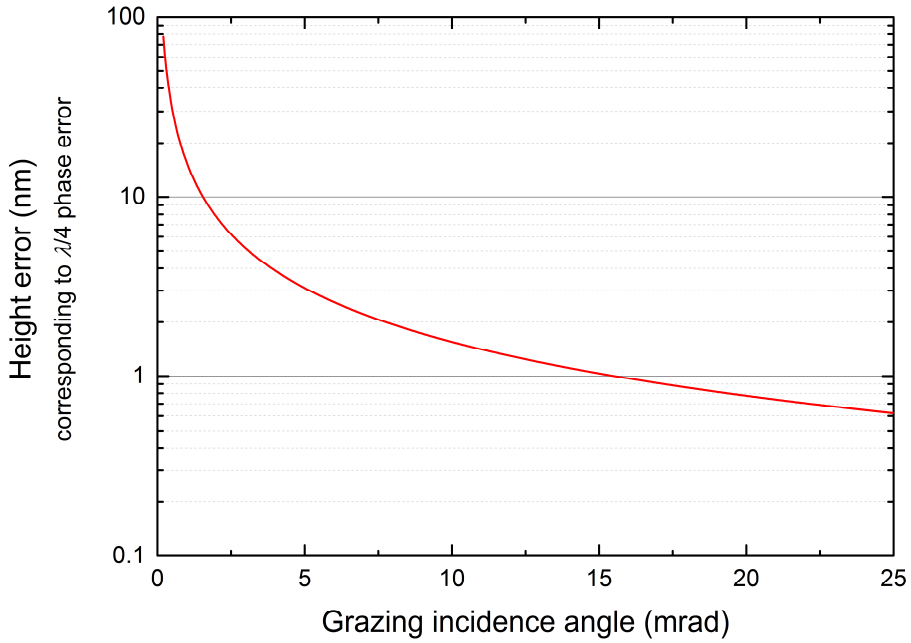


Fig. 3.1. Height error corresponding to $\lambda/4$ phase error at photon energy of 10 keV.

parameters were described in Tables 2.1 and 2.2 are approximately 10 nm and 2.8 nm (PV), respectively, because the grazing incidence angles are 1.5 mrad and 5.5 mrad, respectively. The designed optical parameters of XFEL sub-10-nm focusing mirrors, which were the target optical systems of this study, are shown in Table 3.1.

Table 3.1. Designed parameters of XFEL sub-10-nm focusing mirrors.

| | **Horizontal direction** | **Vertical direction** |
|---|---|---|
| Mirror length (mm) | 380 | 100 |
| Grazing incidence angle on mirror center (mrad) | 14.6 | 13.2 |
| Focal length (m) | 0.380 | 0.070 |
| Distance from source (m) | 79.072 | 72.372 |
| Semi-major axis (m) | 39.696 | 36.221 |
| Semi-minor axis (mm) | 73.438 | 29.710 |

The grazing incidence angles of the sub-10-nm focusing mirrors are greater than those for other optics. Correspondingly, the required shape accuracy is ~1 nm (PV), which is higher than the accuracies required by the other optics. Furthermore, as the surface shape steepness increases, measurement becomes more difficult. The surfaces of the sub-10-nm focusing mirrors are the steepest among the three optical systems shown in Fig. 3.2.

The surface shape profiles of the sub-10-nm focusing mirrors are shown in Fig. 3.3. The lengths of the horizontal and vertical mirrors are 100 mm and 380 mm, respectively. In Fig. 3.3, the black, red, and blue lines represent the heights, radii of curvature, and slopes of these mirrors, respectively. The vertical focusing mirror has a wide slope range of 14 mrad and a small radius of curvature of 1.62 m. The horizontal focusing mirror also has a wide slope range of 11 mrad over a long range of 380 mm. Therefore, a new system is necessary that can measure a wide slope range and small radius of curvature with an accuracy of nearly 1 nm.

The typical measurement methods for X-ray mirrors involve using slope profilers, stitching interferometers, and CMMs. Recently, slope profilers [59–61] and stitching interferometers [56–58] have been primarily used. Slope profilers can perform highly accurate measurements

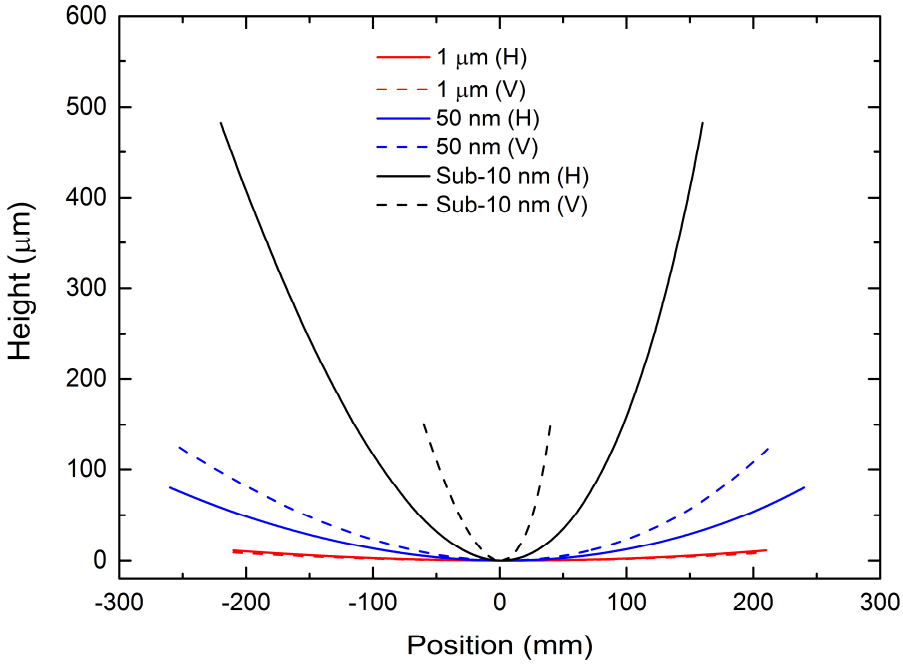


Fig. 3.2. Surface shape profiles of 1 μm, 50 nm, and sub-10-nm XFEL focusing mirrors, whose optical parameters are given in Tables 2.1, 2.2, and 3.1, respectively.

because they do not have reference planes. Interferometers are used to measure high spatial frequencies in two dimensions. On the other hand, CMMs are not currently used to measure X-ray optics, as their accuracies are insufficient to determine shape errors with the accuracy required in X-ray mirror substrate measurements. However, if their accuracies are improved and become acceptable, CMMs could be very useful for measuring steeply and two-dimensionally curved mirrors, since their dynamic ranges are more extensive than those of the other methods. Therefore, we are developing a new system that uses the CMM method. Additionally, after developing this system, we will cross-check its results with those obtained using other methods in order to advance X-ray optics measurements.

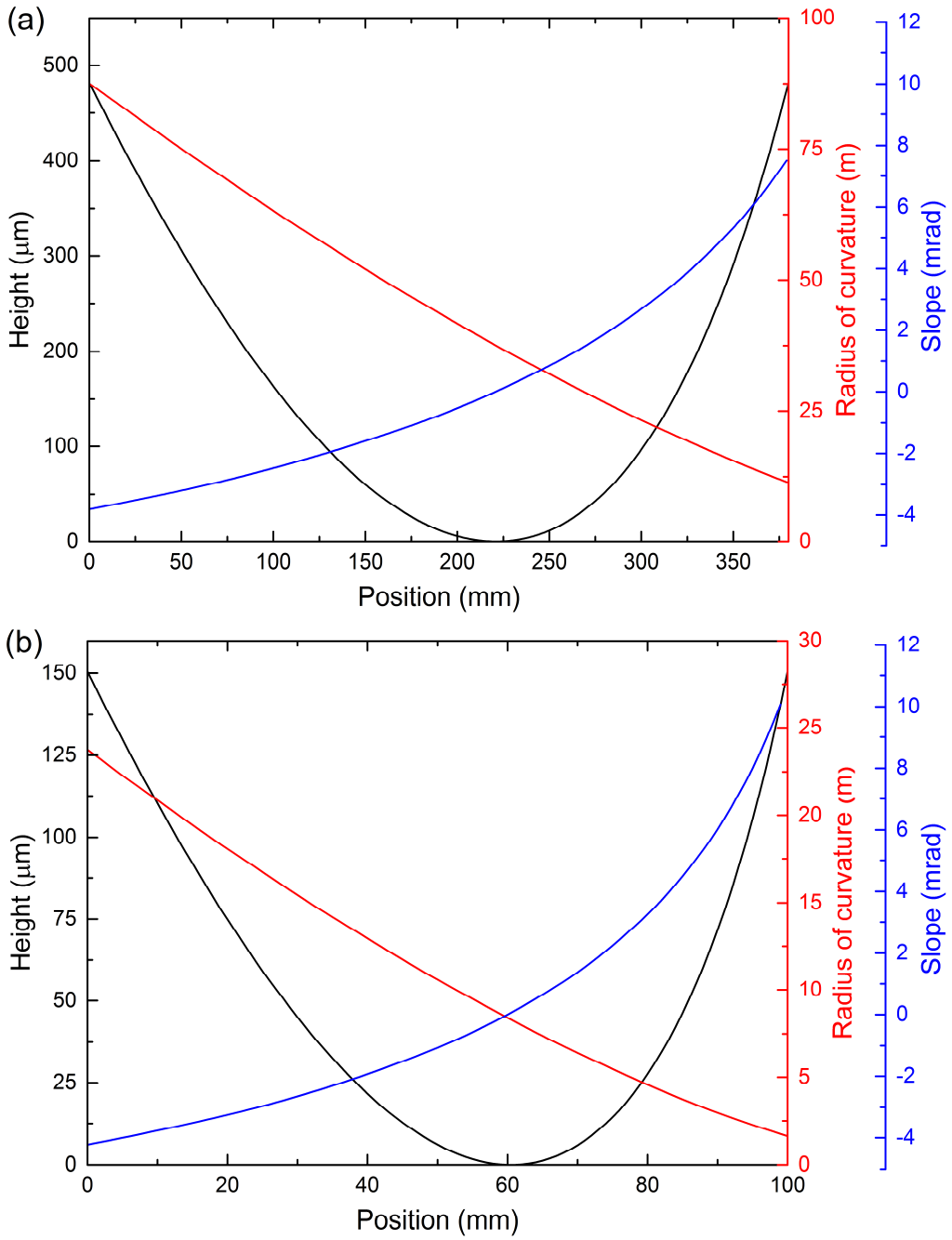


Fig. 3.3. Surface shape profiles of XFEL sub-10-nm focusing mirrors of the (a) horizontal and (b) vertical directions.

## 3.2 Development of Surface Shape Measurement System

### 3.2.1 Apparatus Overview

The surface shape measurement system developed to measure steeply curved surfaces is shown in Fig. 3.4. The main components of this apparatus are a main probe to perform steeply curved surface measurements, sub-probes to measure the posture error of the main probe, and a kinematic stage. In this study, the apparatus was placed in a temperature-controlled room inside a class-1 cleanroom, whose temperature was also controlled. The graph in Fig. 3.4(b) depicts the temperatures outside and inside the room, both of which are very stable. In particular, the temperature stability inside is very high, exhibiting variations of less than ±0.01 °C. A counter-balance is used to prevent center-of-gravity movement and to suppress the elastic deformation of the metrology frame.

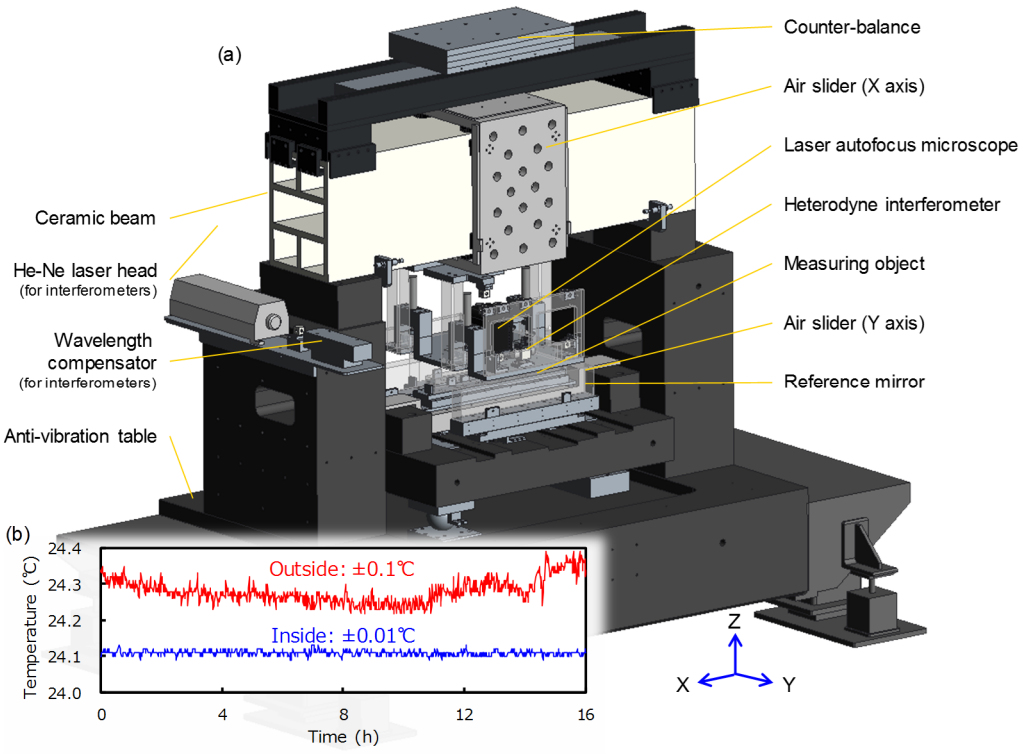


Fig. 3.4. Schematic of shape measurement apparatus.

A laser autofocus microscope (MP-3P, Mitaka Kohki), which is optimal for measuring steeply curved surfaces, is used as the main probe in this system. A principle diagram is shown in Fig. 3.5. First, light emitted from the laser irradiates the sample surface through an objective lens. Then, the light reflected from the sample surface goes to the center of an auto-focus (AF) sensor through the objective and imaging lenses. If the distance between the objective lens and the sample is varied, the position of the light on the AF sensor also varies. To maintain the position of the light on the sensor, the objective lens moves upwards and downwards. The surface shape is determined based on the magnitude of movement of the objective lens. The elemental parts were upgraded from the commercially available machine (MP-3, Mitaka Kohki [63]) to increase the sensitivity of the AF sensor. The linear scale was also upgraded to a resolution of 0.034 nm. The angular dependence of the laser autofocus microscope is measured by MP-3. In this study, the sample was a 5-mm-diameter glass sphere, whose measured surface profile is shown in Fig. 3.6(a). The error with respect to an ideal spherical surface is shown in Fig. 3.6(b), as a function of the surface angle. There is no angular dependence within ±30° (~0.5 rad), which is sufficiently large to measure the surfaces of focusing mirrors (Fig. 3.3).

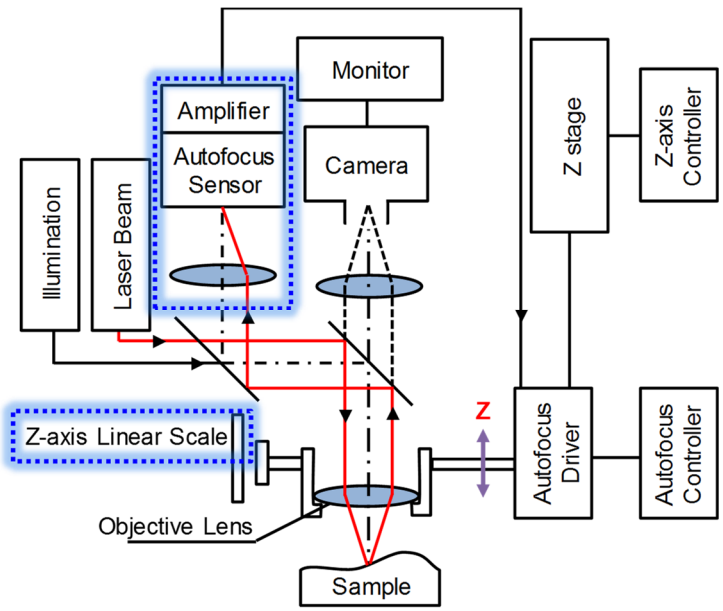


Fig. 3.5. Principle diagram of laser autofocus microscope.

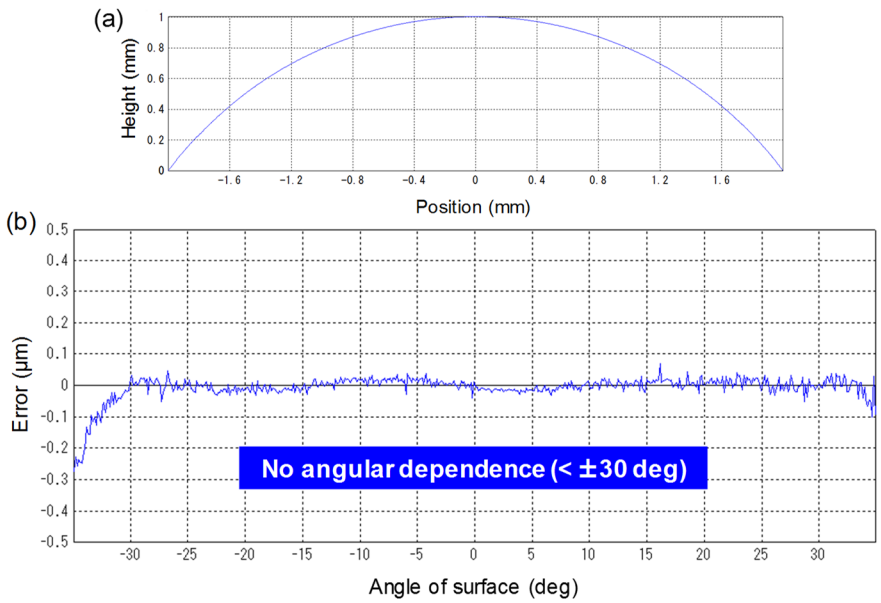


Fig. 3.6. Angular dependence of laser autofocus microscope measured using 5-mm-diameter glass sphere: (a) measured surface profile and (b) error compared to ideal spherical surface.

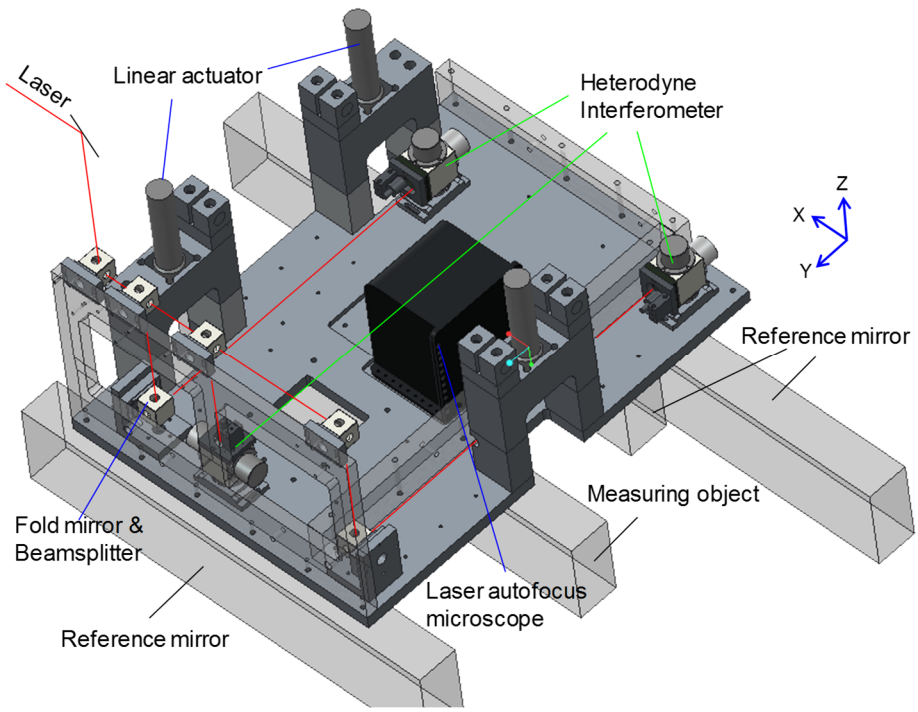


Fig. 3.7. Schematic of probe table.

Three heterodyne interferometers (Zygo ZMI 4000) are used as sub-probes and are located on the same table as the main probe to measure the posture of the main probe. The schematic of the probe table is shown in Fig. 3.7. The laser autofocus microscope is positioned at the center of the table, and the heterodyne interferometers are positioned at the three indicated locations. A reference mirror is placed under each heterodyne interferometer. The heterodyne interferometers are used to measure the posture of the probe table and to correct the value measured by the main probe accordingly.

### 3.2.2 Repeatability Test using Planar Mirror

The measurement repeatability of the shape-measurement apparatus was tested using a nearly flat surface mirror as a measurement object. The size of the mirror was 400 mm (length) × 50 mm (width) × 50 mm (height), and it was composed of Si. The testing conditions are shown in Table 3.2.

Table 3.2. Conditions for testing measurement repeatability using planar mirror.

| Step length | Number of steps | Speed | Averaging |
|---|---|---|---|
| 1 mm | 380 | 1 mm/s | 50 at each point<br>20 lines |

The average number of measurements at each point was 50, and the average number of lines was 20. Therefore, the total number of measurements taken and averaged at each point was 1,000. The repeatability was tested by comparing two independent measurements, and the results are shown in Fig. 3.8. The solid and dashed black lines represent the first and second measurements, respectively, and the solid red line represents the difference between the first and second measurements. Figure 3.8(a) is the result measured using only the laser autofocus microscope. This profile includes the surface profiles of the measured object and the posture error of the probe table due to the bending of the stage guide, etc. Figure 3.8(b) shows the measurements made using only the heterodyne interferometers. This profile includes the surface profiles of the reference mirrors and the posture error of the probe table due to the same factors.

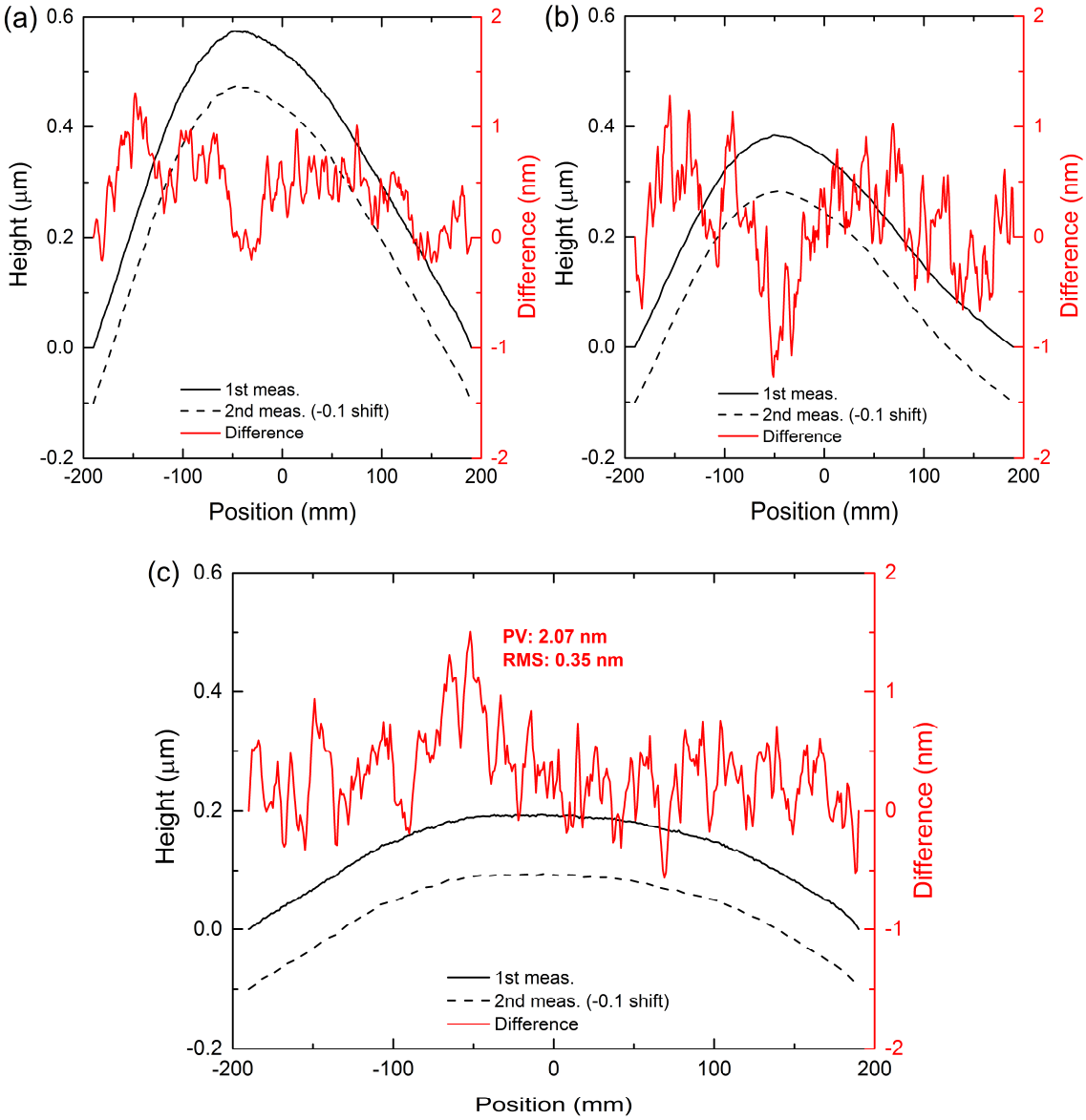


Fig. 3.8. Results of repeatability test: (a) surface profile of measured object, (b) surface profiles of reference mirrors, and (c) repeatability error.

Both figures show the same posture error. Therefore, the error could be eliminated by subtracting the results in Fig. 3.8(b) from those in Fig. 3.8(a). If the errors of the results shown in Figs. 3.8(a) and 3.8(b) were equal, the repeatability error would become zero. Figure 3.8(c) shows conclusive evidence that the developed apparatus can achieve measurements that are repeatable to within ~2 nm (PV). This value is not small; however, high-frequency fluctuations can be reduced by the interferometer.

## 3.3 Fabrication and Measurement of XFEL Sub-10-nm Focusing Mirrors

To fabricate XFEL sub-10-nm focusing mirrors with highly precise elliptical shapes, numerical control machining was performed by using elastic emission machining (EMM) [64–66], stitching interferometers (MSI [56] and RADSI [57]), and the newly developed instrument.

EEM is a processing method utilizing a solid chemical reaction between particles, such as metal oxides, and the workpiece surface. Figure 3.9 shows a conceptual diagram of EEM. When the reactive particles are supplied to the surface by a flow of ultrapure water, the atoms of the workpiece surface and the particles are chemically coupled via oxygen. Atom-by-atom removal can be realized by carrying away the particles using ultrapure water, which can chemically couple to the atoms of the workpiece surface. Figure 3.10 presents schematic diagrams of processes using nozzle-type and rotating-ball-type machining heads. In nozzle-type EEM, the workpiece is processed by using slurry jet from the nozzle with an appropriate pressure, such as 0.2 MPa. The removal spot shape can be easily controlled in this type of machining by changing the nozzle shape, supply pressure, and particle size. In rotating-ball-type EEM, by generating physically stable elastohydrodynamic lubrication conditions between the workpiece and the surfaces of the rotating spheres, the particles are fed to the workpiece surface. By utilizing the parallel flow generated in this area, rotating-ball-type EEM was found to be suitable for automatic smoothing of regions with the spatial wavelengths shorter than 0.1 mm.

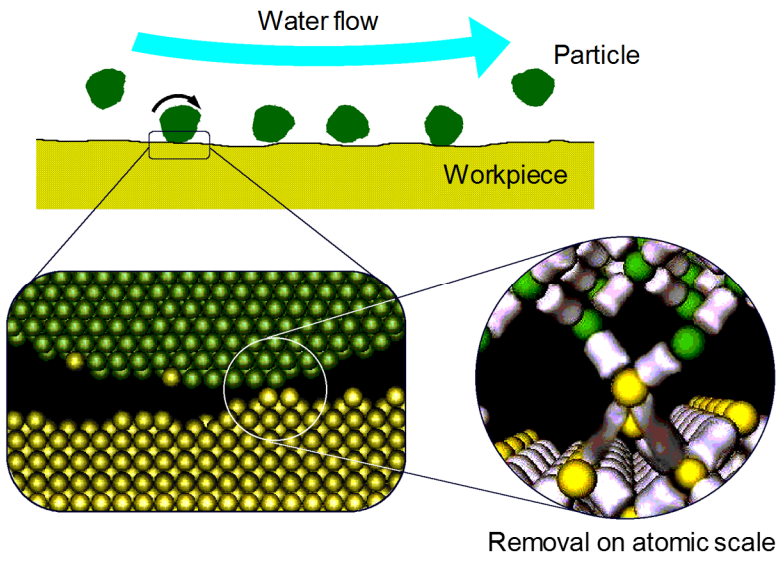


Fig. 3.9. Conceptual diagram of EEM.

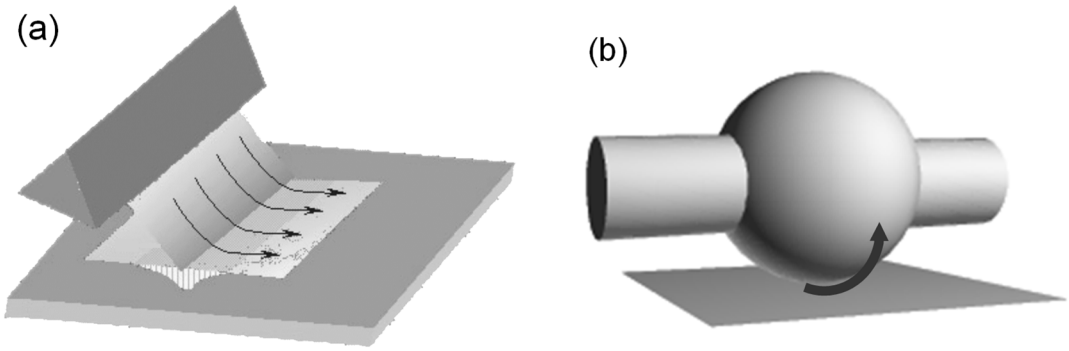


Fig. 3.10. Schematic diagrams of processes using (a) nozzle-type and (b) rotating-ball-type machining heads. Arrows indicate direction of water flow.

To perform the surface shape measurements, MSI using a Michelson-type white light interferometer (Zygo NewView 5000) was employed in the high spatial frequency range, and RADSI using a Fizeau-type phase-shifting interferometer (Zygo GPI-XD/D) and the newly developed instrument were employed in the low spatial frequency range. The residual shape errors obtained after deterministic figuring are shown in Fig. 3.11. The obtained shape accuracy is ~3 nm (PV) and includes some ambiguity because of the high curvature of the surface. We confirmed the final shape using wavefront measurements, which will be described later.

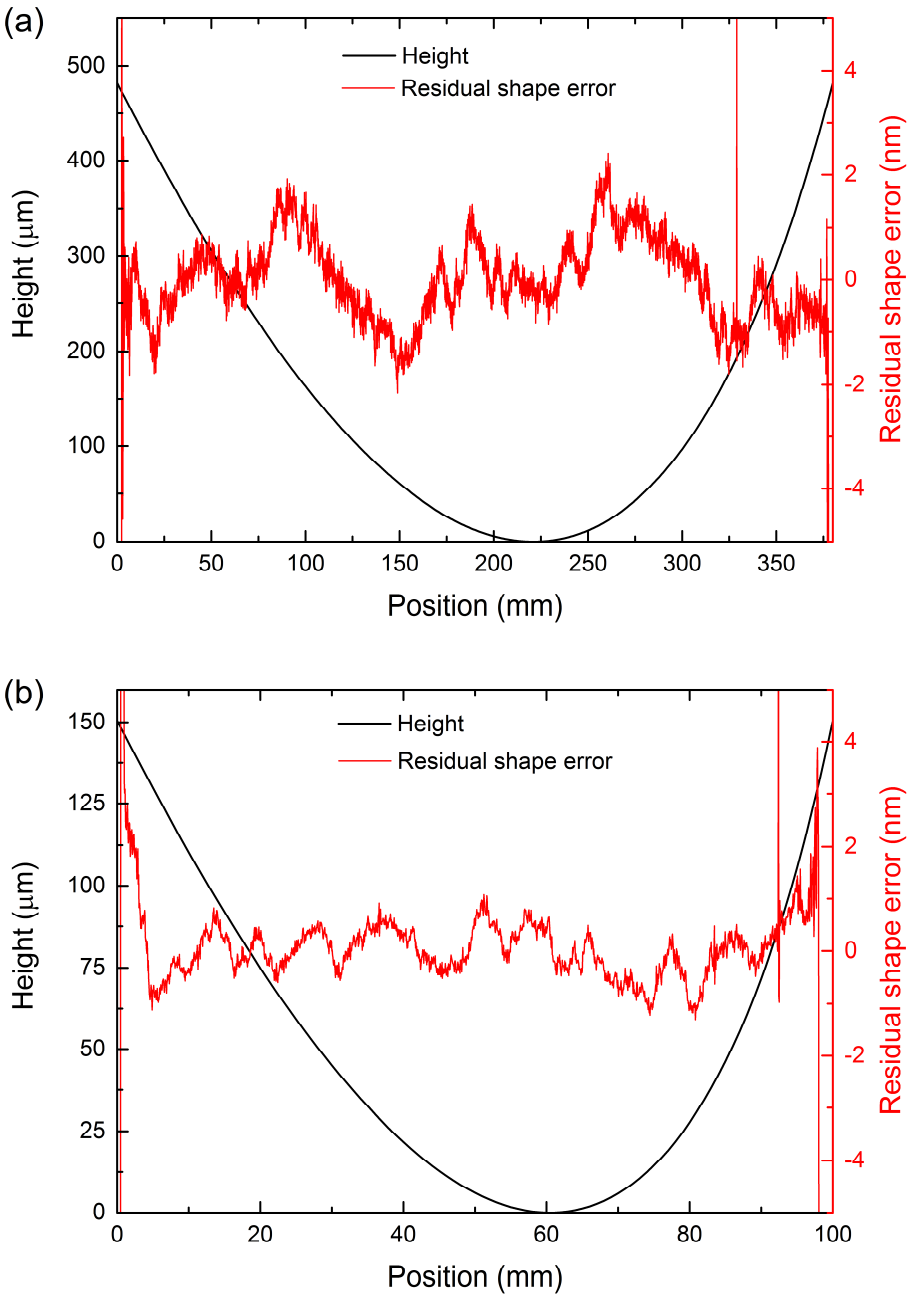


Fig. 3.11. Residual shape errors of (a) horizontal and (b) vertical direction focusing mirrors.

## 3.4 Summary

XFEL sub-10-nm focusing mirrors have steeply curved surfaces that are difficult to measure using conventional shape measurement methods. Their minimum radii of curvature are a few meters, and their slope ranges are several dozen milliradians. Furthermore, the required accuracy, or Rayleigh criterion, of the surfaces of such mirrors is ~1 nm (PV). Therefore, we developed a laser autofocus microscope system featuring a position correction mechanism utilizing three heterodyne interferometers to provide measurements at this level of accuracy. The apparatus could be consistently adjusted to within 2 nm (PV), as demonstrated by a repeatability test.

The sub-10-nm focusing mirrors used in this study were fabricated by EEM and measured by MSI, RADSI, and the newly developed instrument. The residual shape errors typically obtained after deterministic figuring of the sub-10-nm focusing mirrors were ~3 nm (PV). These errors are somewhat high; however, we confirmed the final shape using wavefront measurements, which will be described later.

# Chapter 4

# TOLERANCE OF MULTILAYER FILMS TO X-RAY FREE-ELECTRON LASER IRRADIATION

*One of the critical requirements of the X-ray optical elements for XFELs is sufficient tolerance to intense X-ray irradiation. Therefore, the X-ray damage thresholds of various optical materials in normal and grazing incidence conditions have been extensively investigated. The damage threshold in the normal incidence condition was theoretically estimated using the amount of absorption energy per atom, while in the grazing incidence condition, it was evaluated by considering the energetic photoelectrons that can remove deposited energy from an interaction region [68]. These models have been experimentally verified [69–77]. However, the damage to multilayers induced by XFEL exposure has not been investigated in the hard X-ray regime. In order to investigate this damage in this study, focused and unfocused XFELs were used at a photon energy of 10 keV to provide a sufficiently high intensity and actual operating conditions.*

## 4.1 Development of Thin Film Deposition System

### 4.1.1 Apparatus Overview

The thin film deposition system developed to fabricate a laterally graded multilayer is shown in Figs. 4.1 and 4.2. Our X-ray focusing mirror design requires optical thin film deposition in a region elongated in the longitudinal direction of the mirror substrate. A mirror substrate that is long in the longitudinal direction is required to allow for the small divergence of the XFEL. The deposition apparatus was therefore designed for deposition over an elongated area of 500 mm (length) × 50 mm (width), sufficient to produce XFEL focusing mirrors.

As shown in Fig. 4.1, three direct current (DC) magnetron sputtering cathodes (Kurt J. Lesker Company) with 2-inch targets were mounted in this apparatus. Magnetron sputtering is a widely used deposition method and is generally considered to enable reproducible sub-nanometer control of the deposition thickness [78]. Two targets can be used concurrently in one deposition area to allow the mixing of two materials. The mixing ratio is controlled by adjusting the sputtering cathode power, since the deposition rates are proportional to the input power. Slits and shutters were mounted between the substrate and the sputtering cathode to limit the particle flux to a local deposition area. The substrate was placed on a speed-controlled horizontal scanning stage, and the distance from the target to the substrate was approximately 100 mm.

The elemental performance of the deposition apparatus was tested by depositing Pt and C single-layer thin films. To achieve highly accurate thickness control, it was necessary to determine the spatial distributions of the sputtered atoms accurately. The thickness distributions of the deposited Pt and C films were measured precisely under predetermined conditions by a Fizeau interferometer (ZYGO GPI XP/D). The interferometer method is not suitable for direct measurements of the thickness distributions of thin films, but rather is intended for measurements of the surface shapes of homogeneous substrates. The shape profiles obtained might not accurately represent the shape of the outermost surface, due to the influences of the difference between the reflectivities of the thin film and the substrate and the light reflected from the interface between the thin film and the substrate. To overcome these problems, a sufficiently thick Pt film of ~50 nm was deposited on the substrate in advance.

A spatially limited Pt film was deposited thereon, and the surface shape was then precisely measured by the interferometer. The deposition thickness distribution was calculated from the difference between the surface shape profiles before and after film deposition. Measurement of the C film was performed after deposition of another sufficiently thick Pt film on the C surface.

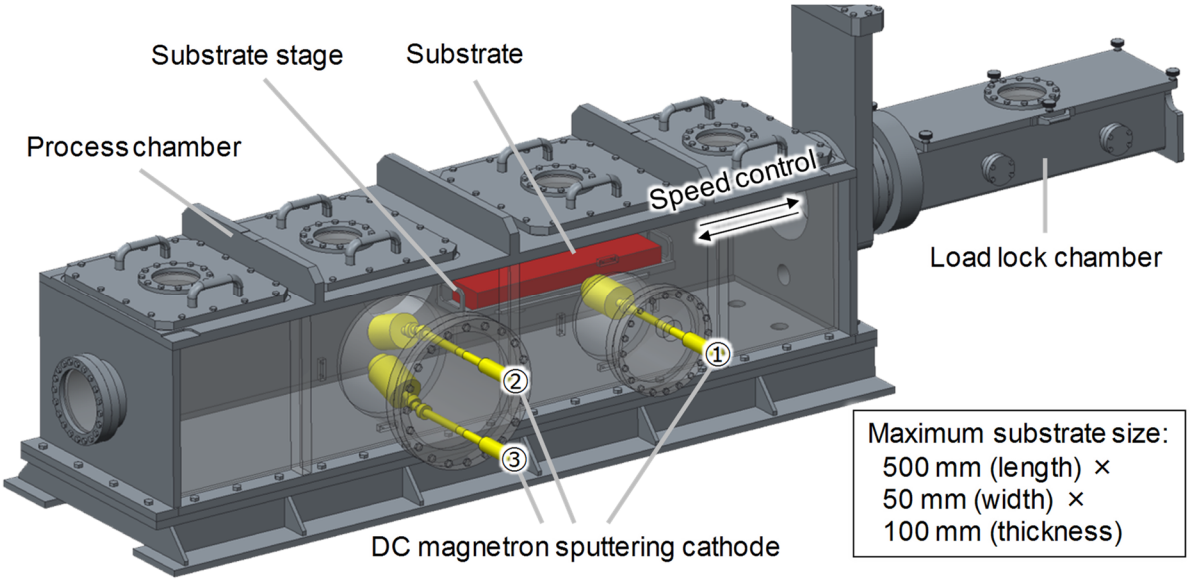


Fig. 4.1. Schematic of thin film deposition apparatus.


Fig. 4.2. Photograph of thin film deposition apparatus.

The measured film thickness distributions of the Pt and C films are shown in Figs. 4.3 and 4.4, which were obtained using the deposition conditions listed in Table 4.1.

Table 4.1. Deposition conditions for Pt and C deposition spots.

| Sample | DC input power (W) (Sputter gun 1 / 2 / 3) | Deposition time (min) | Ar flow rate (sccm) (Sputter gun 1 / 2 / 3) | Ar pressure (Pa) |
|---|---|---|---|---|
| Pt | 10 / 0 / 0 | 40 | 16 / 10 / 10 | 0.11 |
| C | 0 / 120 / 120 | 40 | 16 / 10 / 10 | 0.11 |

In Figs. 4.3 and 4.4, the horizontal direction corresponds to the longitudinal direction of the substrate. The slit used to limit the extent of the deposition region had dimensions of 30 mm (length direction) × 10 mm (width direction). The measured deposition distributions give deposition rates of Pt and C of 2.53 nm/min and 1.71 nm/min, respectively. The deposition rate of C was significantly lower than that of Pt, even at higher input powers, due to the difference between the Pt and C sputtering rates and the different responses of Pt and C to the Ar atom impacts [78,79]. At the C deposition spot, the entire substrate was distorted convexly, as can be seen in Fig. 4.4, due to the film stress caused by the subsequent Pt deposition. This substrate deflection should be corrected when evaluating the C deposition distribution, and the corrected distribution is shown by the dashed line in Fig. 4.4(a).

### 4.1.2 Differential Deposition Test for Mirror Shape Modification

XFEL sub-10-nm focusing mirrors must have extremely accurate surface shapes. As described in Chapter 3, the required shape accuracy across the entire mirror substrate is typically ~1 nm (PV). In addition, the spatial wavelength components of several parts of the mirror length are particularly important to obtain an ideally focused beam. The remaining residual shape errors from the mirror manufacturing process distort the reflected wavefronts and ultimately determine the quality of the focused beam. Therefore, it was planned to obtain the final shape correction by the differential deposition of a Pt thin film, since it has very high reliability and

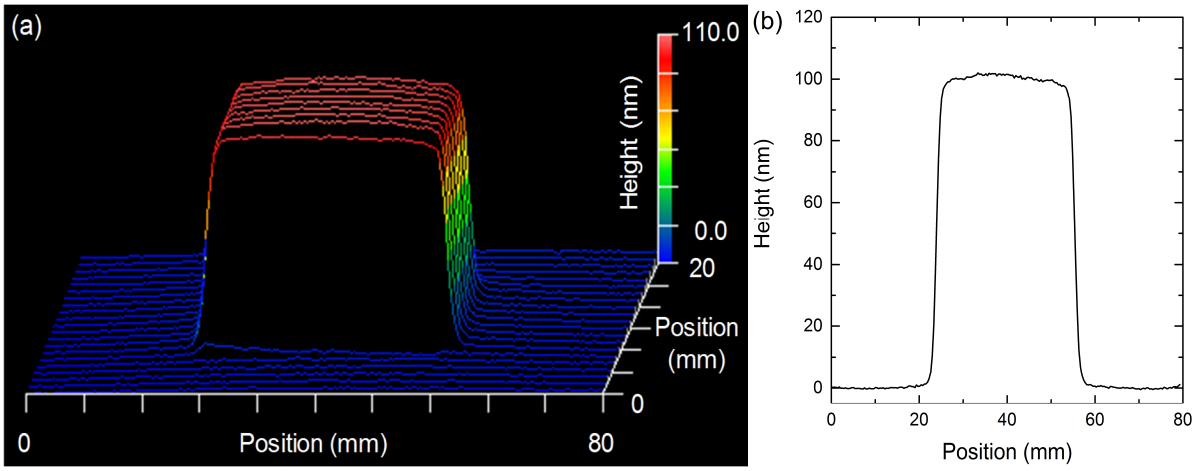


Fig. 4.3. (a) Thickness distribution of Pt deposition spot. (b) Thickness profile along center line of (a).

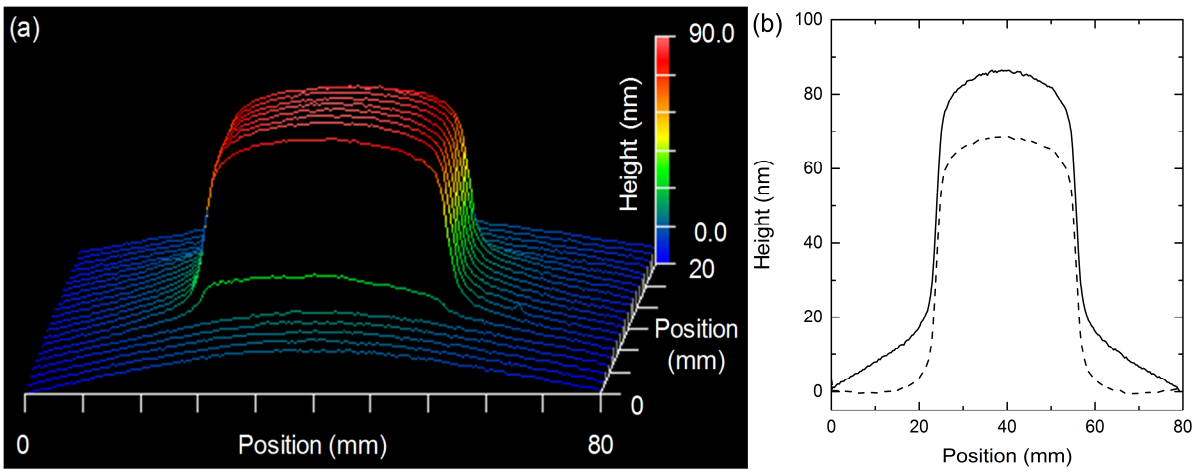


Fig. 4.4. (a) Thickness distribution of C deposition spot. (b) Thickness profile along center line of (a). In (b), dashed line represents correct profile after correcting substrate deflection.

precision despite the relative simplicity of the method.

A differential deposition test was performed using the deposition apparatus. In this test, the spatial wavelengths of the created shape were set to 10–20 mm with a slit size of 2 mm (length direction) × 10 mm (width direction). The creation of shapes with shorter spatial wavelengths is also possible by using narrower length direction slits. The scan speed of the substrate stage was calculated by deconvoluting the deposition spot and the designed film thickness distribution. The thickness profile of the Pt deposition spot for the differential deposition is shown in Fig. 4.5. The deposition conditions were a 20 W input power and 20 sccm Ar flow rate for a deposition time of 20 min. As shown in Fig. 4.5, a sufficiently short horizontal distribution was obtained. The designed and measured thickness distributions agree well, as shown in Fig. 4.6. The residual errors are 1.46 nm (PV) and 0.28 nm (RMS), without low-pass filtering, which include measurement errors, as shown in Fig. 4.7. Eventually, the deposition error was considered to be less than 1 nm (PV), as can be seen from the data obtained by using a 200 Hz low-pass filter (LPF) that are shown in Fig. 4.7.

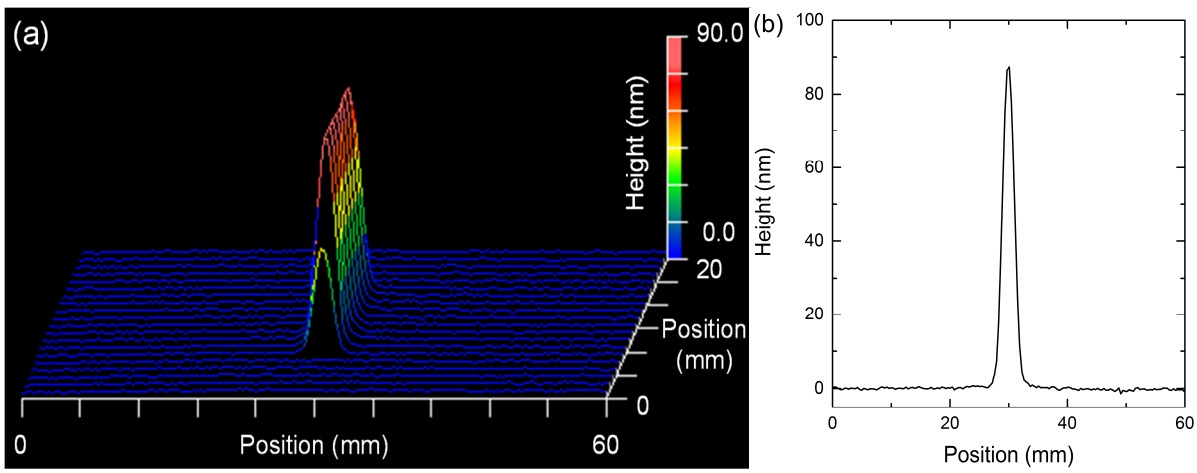


Fig. 4.5. Thickness distribution of Pt deposition spot for differential deposition. (a) Thickness distribution of deposition spot. (b) Thickness profile along center line of (a).

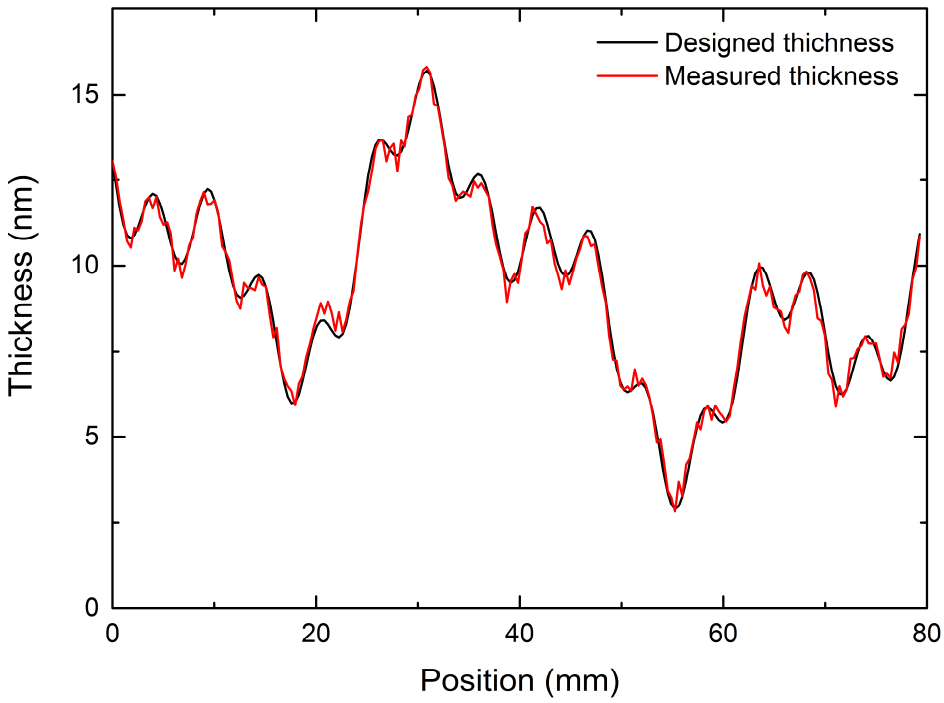


Fig. 4.6. Designed and measured thickness distributions.

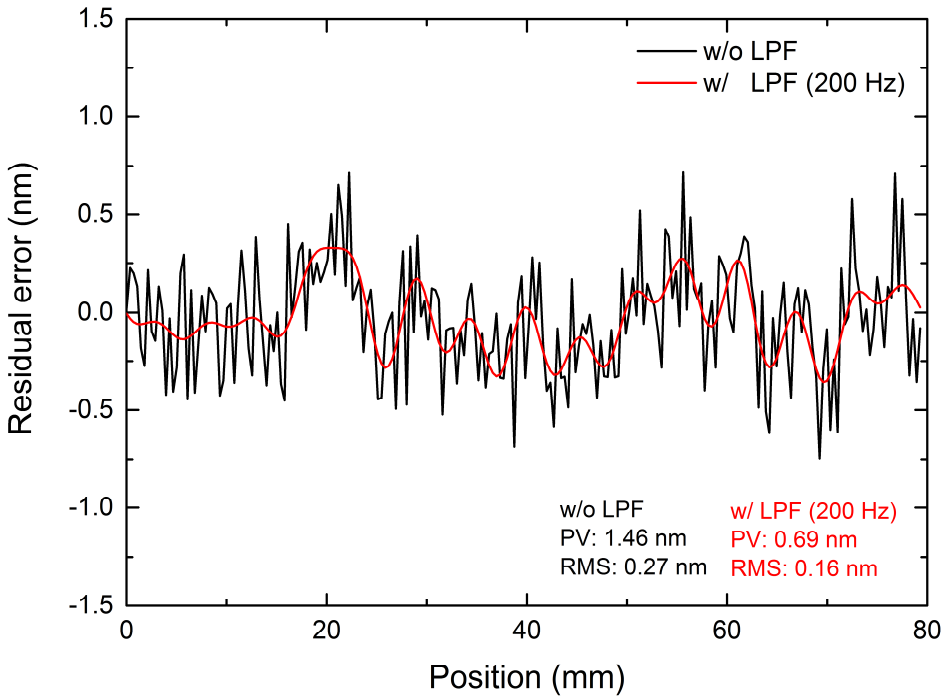


Fig. 4.7. Residual errors of differential deposition with and without LPF. PV and RMS errors are represented.

## 4.2 Evaluation of Breakdown Threshold using Focused XFEL[80]

An experiment was performed at SACLA using 1 μm focusing optics [26] at a photon energy of 10 keV, a pulse duration of <10 fs [47], and a repetition rate of 10 Hz. The experimental system is shown in Figs. 4.8 and 4.9. The test sample was a Pt/C multilayer with 40 bilayers having a multilayer period of 3 nm with a ratio of the Pt layer thickness to the multilayer period $\gamma = 0.5$, deposited on a commercially available Si (100) wafer using a DC magnetron sputtering system. The sample was placed at the focal point and was pre-aligned to the first-order Bragg condition at a reduced X-ray intensity. The irradiation tests were performed using 100-shot exposures in a fluence range of 0.01–10 μJ/μm$^2$ using Si attenuators of various thicknesses. The pulse energy fluctuation over 100 shots was approximately 10%.

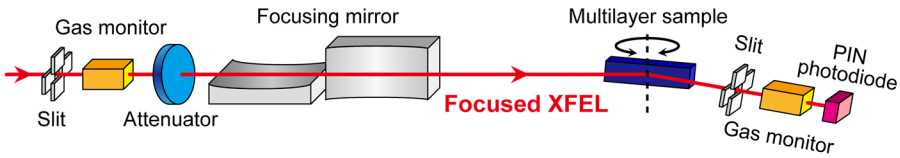


Fig. 4.8. Schematic of experimental system for evaluation of breakdown threshold of Pt/C multilayer.

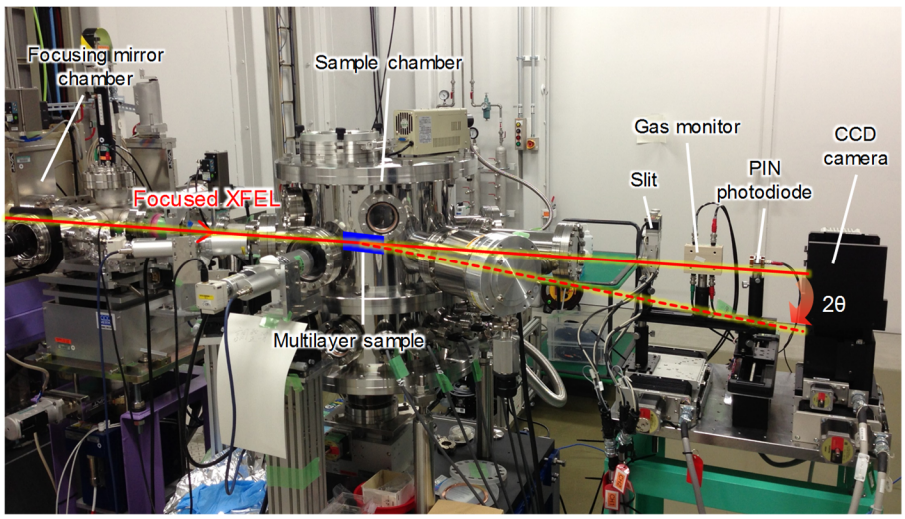


Fig. 4.9. Photograph of experimental system for evaluation of breakdown threshold of Pt/C multilayer.

The damage threshold was determined by comparing the reflectivities, measured in reduced intensity conditions, before and after the 100 shots of fluence-controlled irradiation. The changes in reflectivity during the 100-shot exposure were also monitored.

The reflectivities before and after the fluence-controlled irradiation are presented in Fig. 4.10. As shown, the reflectivity does not change at fluences less than 0.051 μJ/μm$^2$; however, a notable decrease is apparent as the fluence exceeds this value, corresponding to the damage threshold of the Pt/C multilayer.

Typical reflectivity changes during the 100-shot exposures in different fluence conditions are shown in Fig. 4.11(a). Images of the sample surfaces after exposure were obtained with an optical microscope (OM) and are shown in Fig. 4.11(b). At a fluence of 0.051 μJ/μm$^2$, no damage is apparent in either the reflectivity data or the OM image. However, at fluences considerably greater than the damage threshold, a scratch is noticeable in the OM image, with a corresponding rapid decrease to almost zero reflectivity. Interestingly, only the first pulse exhibits the original reflectivity because the temporal duration of the X-ray pulses was much faster than the changes in the multilayer structure. At a fluence of 0.11 μJ/μm$^2$, just slightly larger than the damage threshold, there is a slight decrease in the reflectivity, with little damage observable in the OM image.

To investigate the detailed mechanisms behind the changes observed at the last condition, $\theta$-2$\theta$ scans were performed before and after irradiation at a reduced intensity and indicated a shift of the Bragg angle from 22.05 mrad to 21.98 mrad, together with a decrease in the reflectivity, as shown in Fig. 4.12(a). This shift corresponds to an expansion of the multilayer period by approximately 0.3% on average over the irradiated area. Cross-sectional transmission electron microscopy (TEM) images of a central part of the footprint were obtained before and after irradiation and are shown in Figs. 4.12(c) and 4.12(b), respectively, indicating that the multilayer expanded by approximately 10% and that the expansion was widely distributed across its footprint. The expansion may originate from intermixing at the interface and the introduction of vacancies into the Pt layer, although further investigation is required to clarify this phenomenon.

The damage threshold fluence $F_{\mathrm{th}}$ can be converted to the damage threshold dose $D_{\mathrm{th}}$ for a single atom using the following expression [68,81,82]:

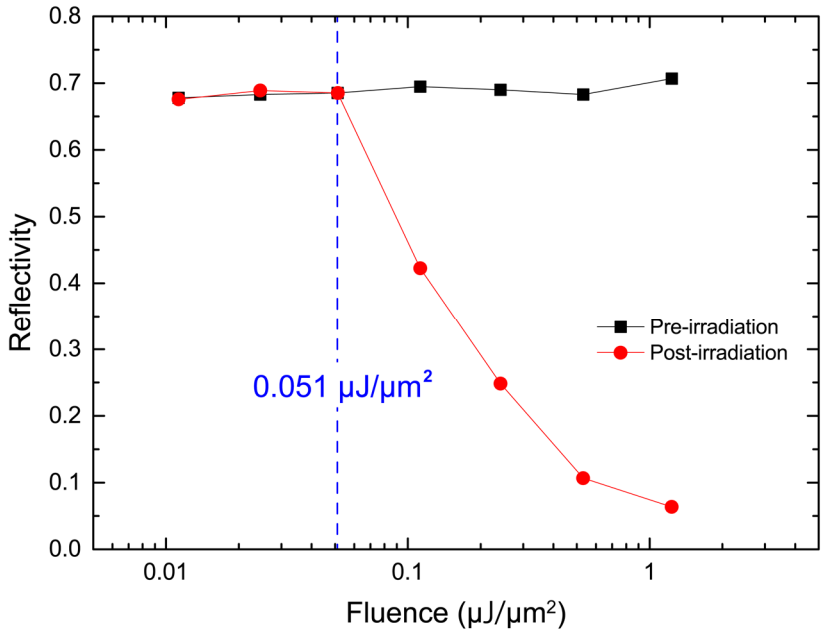


Fig. 4.10. Change in reflectivity versus irradiation fluence.

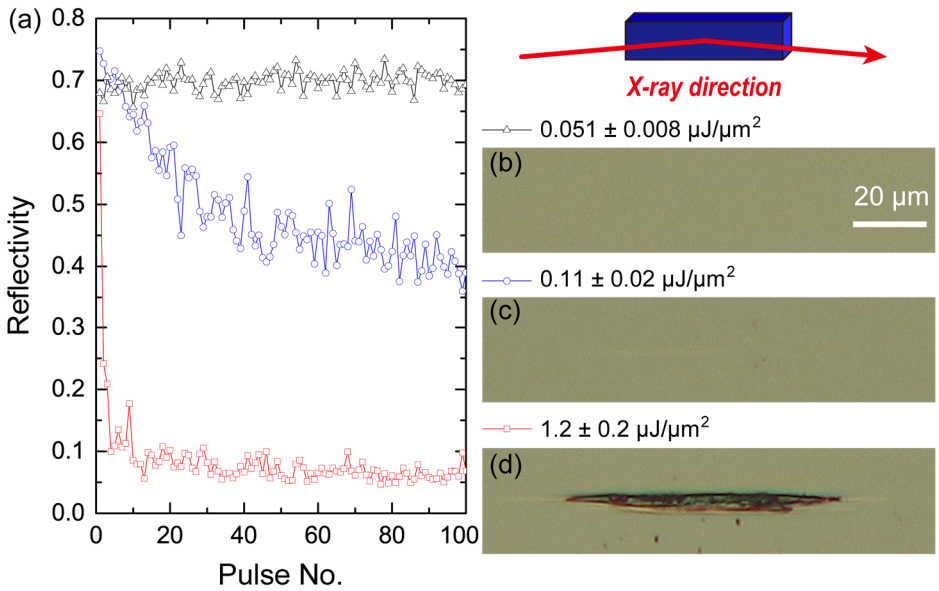


Fig. 4.11. (a) Changes in reflectivity versus number of pulses at each irradiation fluence. (b)–(d) OM images of sample surface after 100 pulses of irradiation.

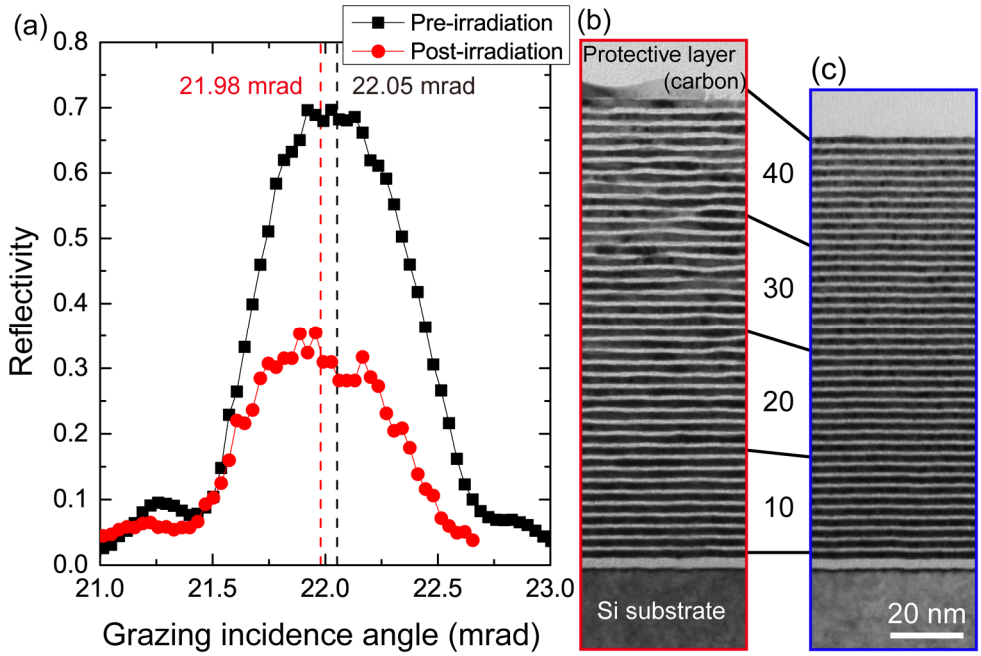


Fig. 4.12. (a) Bragg angle shift measurement by $\theta$-$2\theta$ scan near first-order Bragg angle. Measured pre- and post-irradiation Bragg angles were 22.05 mrad and 21.98 mrad, respectively. (b), (c) Cross-sectional bright-field TEM images of irradiated and non-irradiated areas, respectively. Dark and bright layers correspond to Pt and C layers, respectively.

$$D_{\mathrm{th}} = \frac{F_{\mathrm{th}}(1-R)\sin\theta}{dQ_{\mathrm{Pt}}}, \tag{4.1}$$

where $R$ and $\theta$ are the reflectivity and grazing incidence angle, respectively. In this study, $R$ and $\theta$ were estimated to be 0.76 and 21.6 mrad, respectively, which were theoretically determined based on the multilayer design parameters. Here, $Q_{\mathrm{Pt}}$ is the approximate quantity of Pt atoms, which is given by

$$Q_{\mathrm{Pt}} = \frac{N_{\mathrm{A}}\rho_{\mathrm{Pt}}}{A_{\mathrm{Pt}}}\gamma + \frac{N_{\mathrm{A}}\rho_{\mathrm{C}}}{A_{\mathrm{C}}}(1-\gamma)\frac{\rho_{\mathrm{C}}}{\rho_{\mathrm{Pt}}}, \tag{4.2}$$

where $N_{\mathrm{A}}$, $\rho$, and $A$ are Avogadro's constant, density, and atomic weight, respectively, and the subscripts Pt and C denote the Pt and C layers, respectively. The quantity of C atoms is included as a converted quantity using a ratio of the general electron penetration depth, which is approximately inversely proportional to the density [83]. Moreover, the energy deposition depth $d$ is given by

$$d = \sqrt{d_{\mathrm{x}}^2 + d_{\mathrm{e}}^2}, \tag{4.3}$$

where $d_{\mathrm{x}}$ and $d_{\mathrm{e}}$ are the X-ray penetration depth and electron collision range [84], respectively. In this case, $d_{\mathrm{e}}$ was assumed to be 70 nm, which is twice the $d_{\mathrm{e}}$ value of a Pt single layer (35 nm [85]), because electrons penetrate the C layers more easily than the Pt layers. An estimate of $d_{\mathrm{x}}$ was obtained using an XSW field intensity of $1/e$. The XSW field intensity was calculated using Eq. (2.21), with the assumption that the sample was surrounded by a vacuum and that the parameters of the materials retained their bulk properties [86]. The calculated XSW field intensity is shown in Fig. 4.13, where Fig. 4.13(b) shows $d_{\mathrm{x}}$ to be 22.5 nm at the Bragg angle. According to Eq. (4.1), $D_{\mathrm{th}}$ was calculated to be 0.58 eV/atom, which is in reasonable agreement with the measured threshold dose of a Pt single layer (0.52 eV/atom [74]).

The typical beam size of SACLA at a photon energy of 10 keV is 200 μm in diameter (FWHM), with a pulse energy of 400 μJ, implying that the fluence should reach 0.01 μJ/μm$^2$. This fluence is sufficiently lower than the damage threshold of the Pt/C multilayer. Thus, we confirmed the feasibility of utilizing multilayered Pt/C films as optical components in XFELs.

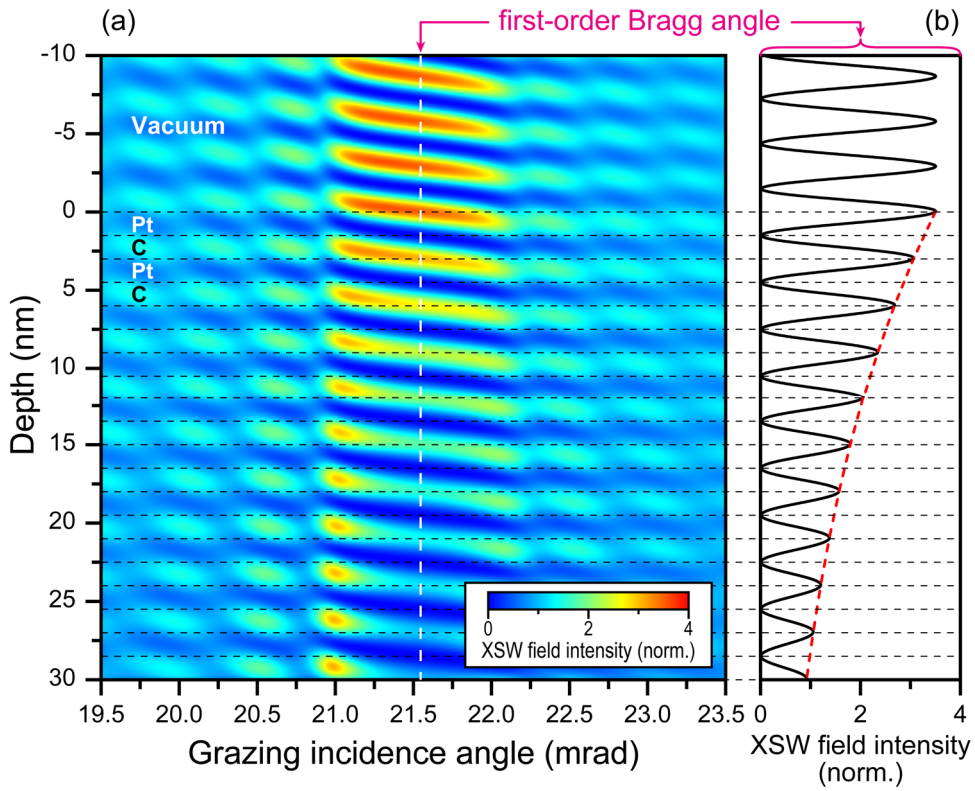


Fig. 4.13. Calculated XSW field-intensity distribution in multilayer structure versus (a) grazing incidence angle and depth of multilayer medium and (b) line profile at first-order Bragg angle.

## 4.3 Evaluation in Actual Operating Conditions using Unfocused XFEL[87]

Two Pt/C multilayer samples, fabricated by the DC magnetron sputtering system on Si (100) wafer substrates, were evaluated. Number of bilayers $N$, designed and measured multilayer periods $d$, and designed and measured ratio $\gamma$ of the Pt layer thickness to the multilayer period of the multilayer samples are shown in Table 4.2.

Table 4.2. Details of Pt/C multilayer samples.

| Sample | $N$ | Design | | Measured (Cu-Kα) | |
|---|---|---|---|---|---|
| | | $d$ (nm) | $\gamma$ | $d$ (nm) | $\gamma$ |
| A | 45 | 5.0 | 0.5 | 4.78 | 0.508 |
| B | 45 | 2.5 | 0.5 | 2.45 | 0.527 |

An X-ray reflectometer (Rigaku SmartLab) was used to estimate the thicknesses, since X-ray reflectrometry is a non-destructive and non-contact method for thickness determination of thin films. The experimental setup consisted of a Cu-Kα X-ray source ($\lambda$ = 0.154 nm) and a $\theta$-2$\theta$ goniometer stage to change the grazing incidence angle on the sample surface, as shown in Fig. 4.14. The intensities of the X-rays reflected by the sample were monitored at various grazing

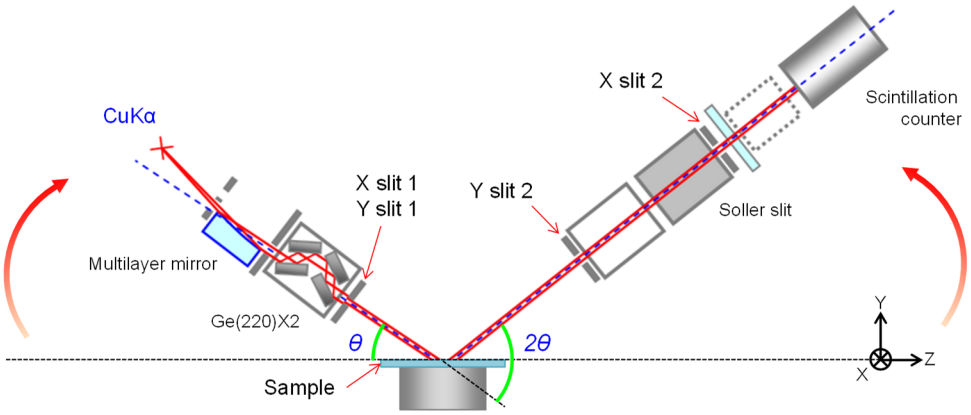


Fig. 4.14. Schematic of X-ray reflectometer.

incidence angles.

To ensure that the multilayer films would function in typical operating conditions, multilayer films A and B were evaluated with the non-monochromatic XFEL at a photon energy of 10 keV, a pulse duration of <10 fs [47], a repetition rate of 10 Hz, a mean pulse energy of 130 μJ, and a beam diameter (FWHM) of 300 μm. In this evaluation, the fluence of the incident beam was designed to be ~0.0014 μJ/μm$^2$. In the first-order Bragg angle, the change of reflectivity of film B was determined after X-ray irradiation for 5 hours. Irradiation damage was expected to be induced in the B multilayer due to its very large first-order Bragg angle. Post-irradiation, the cross-section of an irradiated region of film B was compared with that of a non-irradiated region by TEM.

Figure 4.15 shows the measured X-ray reflectivities of samples A and B as functions of the grazing incidence angle of the XFEL. The solid lines represent the measured reflectivities, and the dashed lines show the curve fitting results. The experimental data from samples A and B show that their reflectivities of the first-order Bragg peak were 78.3% and 51.8%, respectively. Since sufficiently high reflectivities were obtained, these samples function well as multilayer films. The periods of the multilayers and the ratios of Pt layer thickness to multilayer period were estimated by using the curve fitting results and are shown in Table 4.3.

Table 4.3. Multilayer periods and ratios of Pt layer thickness to multilayer period of Pt/C multilayer samples. Thicknesses of fabricated samples were measured by using X-ray reflectometer and XFEL.

| **Sample** | **Measured (Cu-Kα)** | | **Measured (XFEL)** | | **Deviation of multilayer period (%)** |
|---|---|---|---|---|---|
| | ***d* (nm)** | ***γ*** | ***d* (nm)** | ***γ*** | |
| A | 4.78 | 0.508 | 4.74 | 0.513 | 0.84 |
| B | 2.45 | 0.527 | 2.42 | 0.528 | 1.22 |

The calculated multilayer periods agree with the results obtained from the X-ray reflectometer to within 1%.

The reflectivity of film B in the first-order Bragg peak is shown in Fig. 4.16, with no change during the 5 hours of measurements. After 50 min, 100 min, 200 min, and 300 min, the angle

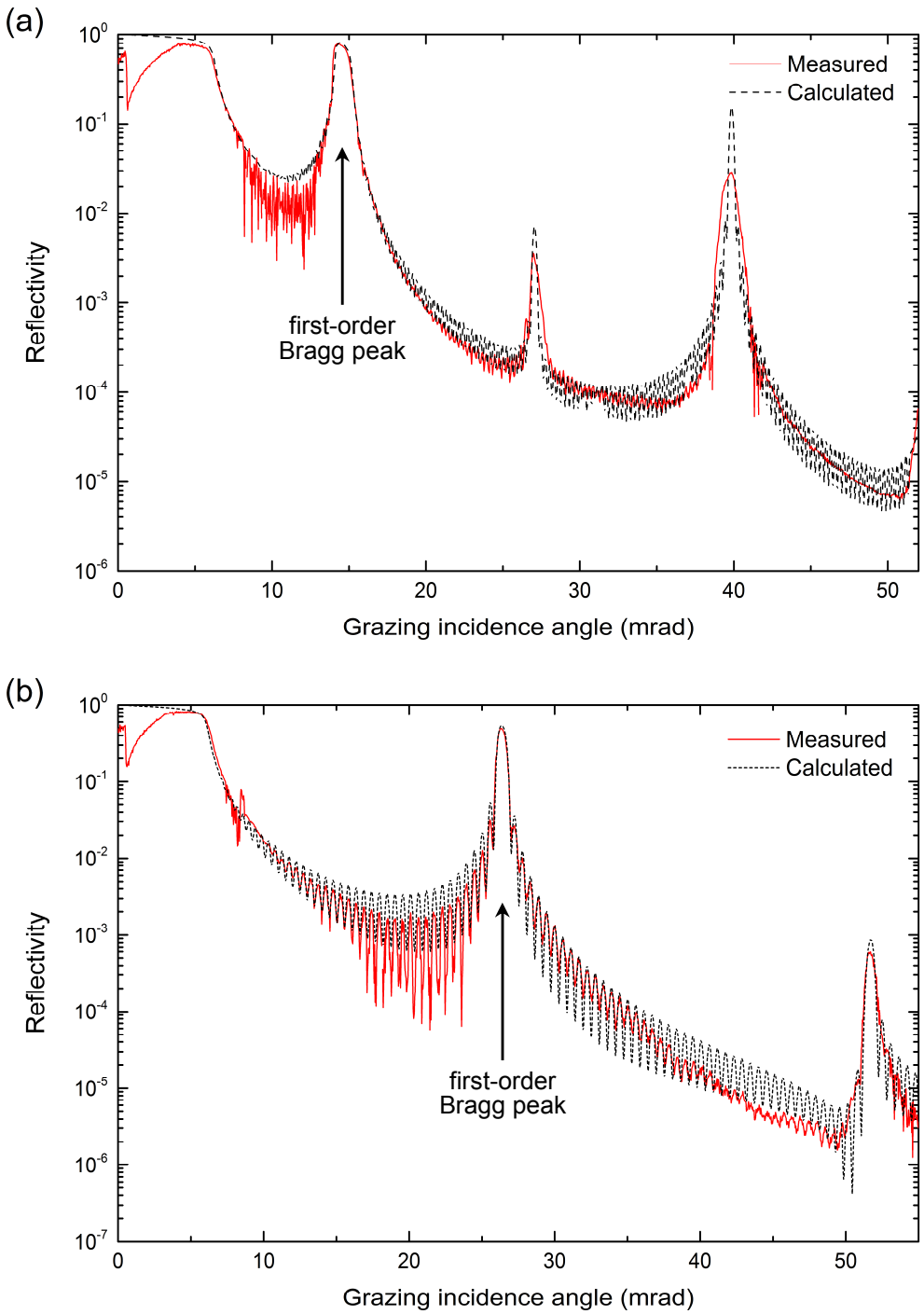


Fig. 4.15. X-ray reflectivities of Pt/C multilayer samples (a) A and (b) B versus grazing incidence angle. Solid and dashed lines show experimental data and calculated fit curves, respectively. X-ray reflectivities of first-order Bragg peaks are (a) 78.3% and (b) 51.8%.

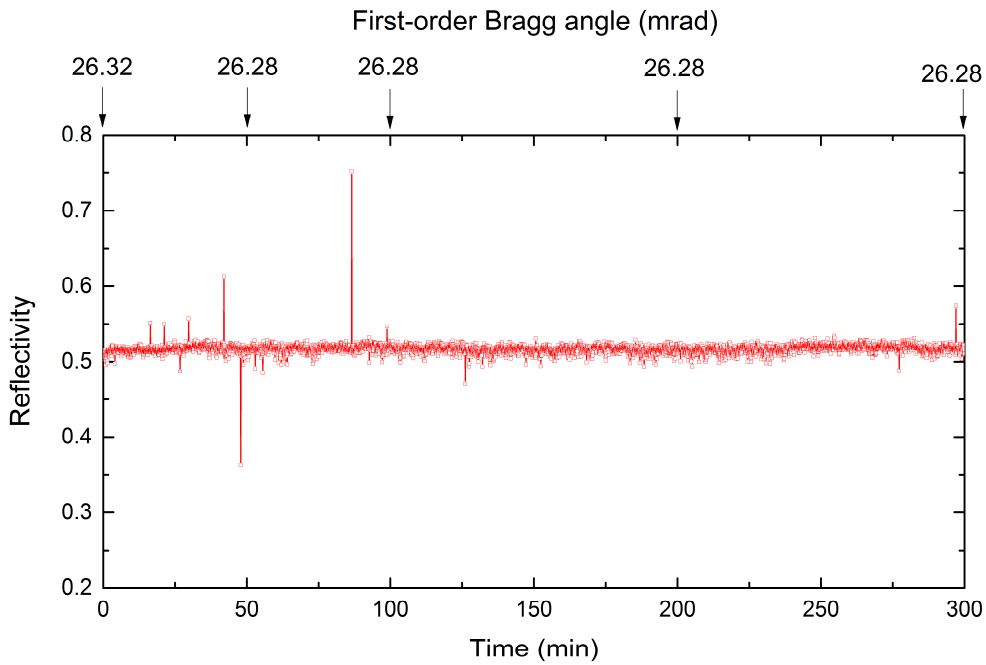


Fig. 4.16. X-ray reflectivity versus time, with annotations indicating measured first-order Bragg peak angles of sample B at various times.

of the first-order Bragg peak was measured, and the results are presented in Fig. 4.16. As shown, the angle of the first-order Bragg peak also did not change.

Figure 4.17 depicts the cross-sectional TEM images of the surface and substrate sides of the non-irradiated and irradiated regions of film B. The dark and bright layers correspond to the Pt and C layers, respectively. No evidence of XFEL irradiation damage is evident. The multilayer periods and the ratios of Pt layer thickness to multilayer period were estimated from these images. The resulting values were somewhat larger than those obtained from the X-ray reflectometer and the XFEL, possibility due to slight inclination of the cross-sections.

The reflectivity and TEM images do not display any observable changes throughout the 5 hours irradiation period. Thus, the unfocused XFEL irradiation did not seriously damage the multilayer film samples.

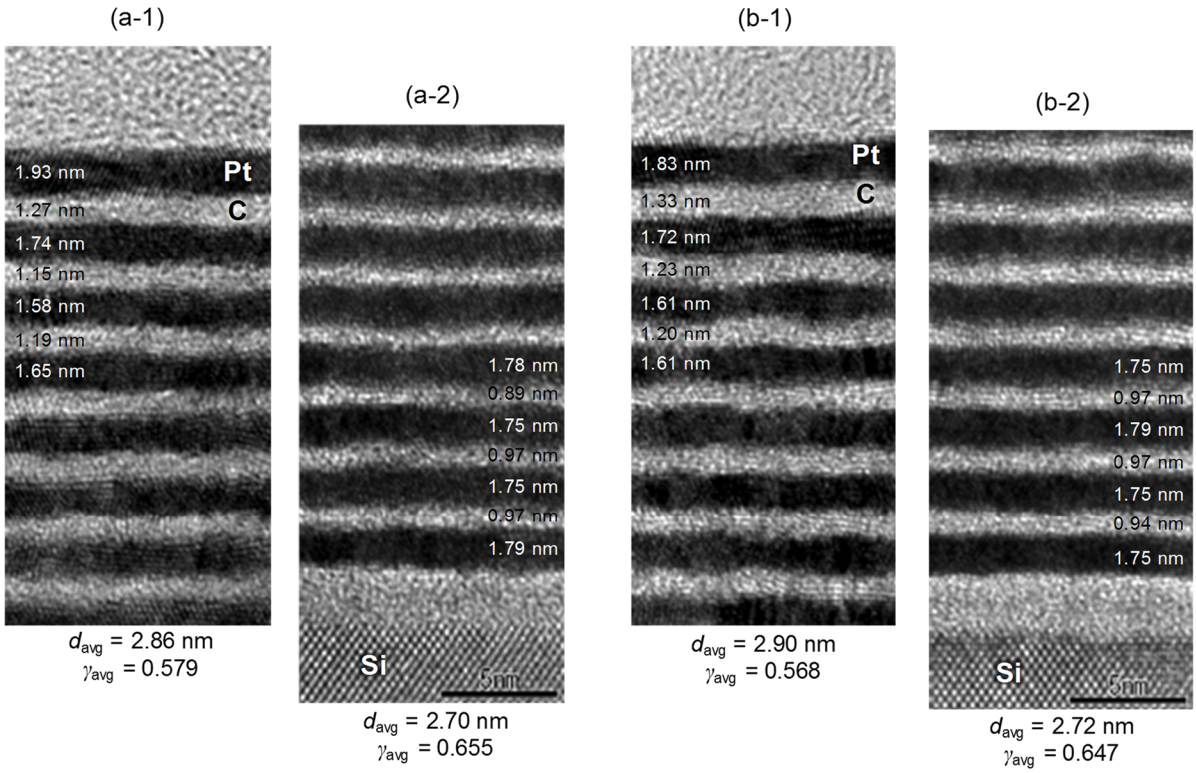


Fig. 4.17. Cross-sectional bright-field TEM images of film B. (a) and (b) show non-irradiated and irradiated sections, respectively, and "-1" and "-2" in figure part names denote surface side and substrate side, respectively. Dark and bright layers correspond to Pt and C layers, respectively. $d_{avg}$ is average multilayer period, and $\gamma_{avg}$ is average ratio of Pt layer thickness to multilayer period.

## 4.4 Summary

In hard X-ray focusing, multilayer mirrors are required, because reflection at high grazing incidence angles is necessary. To fabricate laterally graded multilayer mirrors for X-ray focusing, a thin film deposition system was developed in this study. Then, an arbitrarily shaped mirror was fabricated using the differential deposition technique to estimate the accuracy of the deposition apparatus. The deposition apparatus was found to be capable of sub-nanometer accuracy, which is sufficiently high for multilayer mirror fabrication and mirror shape modification.

We also evaluated the feasibility of using Pt/C multilayers for XFEL focusing applications. The X-ray reflectivity, surface, and cross-section of a multilayer film were measured to observe the irradiation damage. We determined the damage threshold of the Pt/C multilayer using a 1 μm focused hard XFEL beam with a photon energy of 10 keV and found that the damage threshold of the Pt/C multilayer with a bilayer period of 3 nm was 0.051 $\mu J/\mu m^2$, confirming that it could be employed in XFEL focusing optics. Moreover, no damage to the multilayer was observed during testing in the conditions in which it was designed to be used. Our calculated value of the threshold atomic dose in the multilayer was similar to that of the bulk material. The obtained threshold should be a useful criterion for designing multilayer optics in XFEL sub-10-nm focusing and related fields.

# Chapter 5

# IMPROVEMENT OF X-RAY REFLECTIVITY IN MULTILAYER FILMS

*The achievement of high photon densities using reflective optics requires the use of multilayer films in the hard X-ray regime. One important property of multilayer films used as optical elements is X-ray reflectivity, which is related to focusing efficiency. Since the X-ray reflectivity of a multilayer film is mainly related to the X-ray wavelength and the composition of the film, it is necessary to design multilayer films in accordance with the wavelength to be used, by varying the base materials, component ratio, and number of layers [88]. Additionally, compatibility between the different materials in a multilayer film is important to suppress interdiffusion and interface roughness between the layers. To improve the reflectivities of Pt/C hard X-ray multilayers, we evaluated the effects of thinning and C-doping their Pt layers.*

## 5.1 Determination of Critical Pt Layer Thickness

To confirm the Pt/C multilayer reflectivity improvements realized by thinning their Pt layers, the changes in reflectivity with varying period $d$ and number of bilayers $N$ were calculated as functions of the ratio $\gamma$ of the Pt layer thickness to the total bilayer thickness, and the results are shown in Fig. 5.1. A Cu-Kα X-ray source was used with a photon energy of 8.048 keV. The multilayer period of such a laterally graded multilayer is typically in the range of 3–9 nm [89]. At least 30 bilayers are required since the reflectivity of short-period multilayers is saturated.

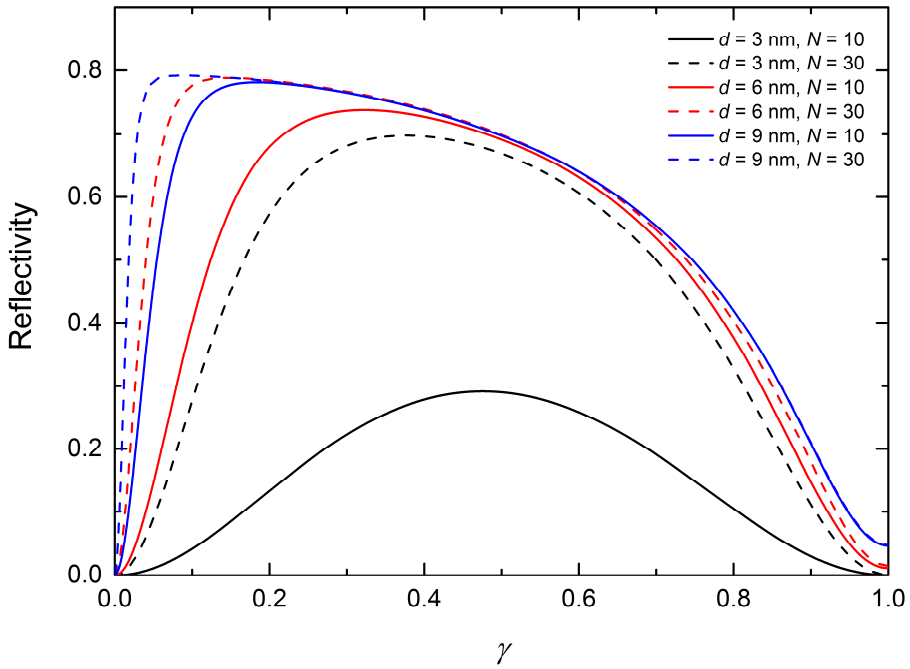


Fig. 5.1. Calculated X-ray reflectivities of Pt/C multilayers with varying $d$ and $N$ as functions of $\gamma$ at photon energy of 8.048 keV.

In the case of a long-period multilayer, as the Pt layer thickness is reduced, the reflectivity improves if there are a sufficient number of bilayers to reflect the incident X-rays.

Pt layer thinning can increase the reflectivities of long-period multilayers. However, since it is not possible to reduce the Pt layer thickness indefinitely, the critical Pt layer thickness was evaluated by using the reflectivities of Pt/C multilayers. Although the reflectivity can be increased by reducing the Pt layer thickness, caution must be exercised so that a continuous film is not formed when the Pt layers are too thin.

The measured thicknesses of the Pt layers used in this study were 1.0 mm, 1.1 mm, 1.2 mm, and 1.4 nm; the multilayer period was 4 nm; and the number of bilayers was 30. The measured and calculated X-ray reflectivities are shown in Fig. 5.2. Initially, the calculated reflectivity increases as the Pt thickness decreases; however, when the Pt thickness becomes less than 1.2 nm, the measured reflectivity drops off significantly. The reason for this reflectivity reduction is that continuous Pt layers are not formed when their thicknesses are less than 1.2 nm. Thus, we confirmed that the critical Pt layer thickness is 1.2 nm, which is reasonably comparable to the results of previous research [33], in which the critical thickness was determined by

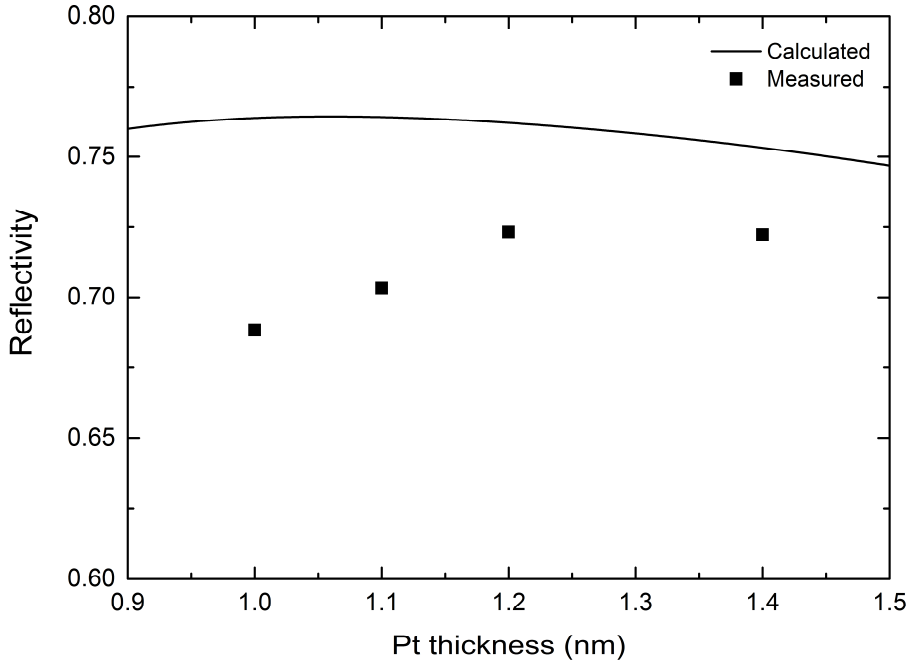


Fig. 5.2. Critical Pt layer thickness measured by X-ray reflectivity of Pt/C multilayers in 30-bilayer stack with $d$ = 4 nm.

measuring the electrical resistance of a single Pt layer. To obtain the highest reflectivity, the optimal Pt layer thickness in the Pt/C multilayer structure was 1.2 nm.

The reflectivities of Pt/C multilayers with fixed Pt layer thickness $d_{Pt}$ = 1.2 nm or with fixed $\gamma$ = 0.5 were calculated and measured at various incidence angles, and the results are compared in Fig. 5.3. Again, 30 bilayers were used, and the X-ray wavelength was 0.154 nm. As shown, the calculated reflectivity is higher with $d_{Pt}$ = 1.2 nm than with $\gamma$ = 0.5. The experimentally measured reflectivity also increases when the theoretically obtainable reflectivity increases.

## 5.2 X-ray Reflectivity Improvement in Pt/C Multilayers by C-Doping of Pt Layers

The X-ray reflectivity of a multilayer film depends strongly on the quality of the interfaces between the individual layers [90–93]. Furthermore, the reflectivity reduction induced by

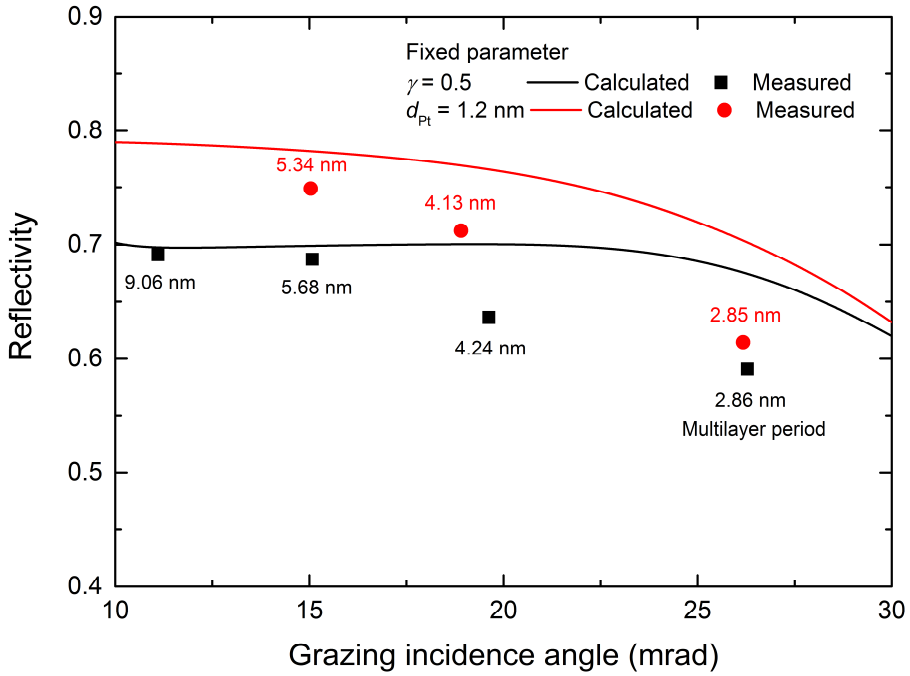


Fig. 5.3. Calculated and measured X-ray reflectivities of Pt/C multilayers with fixed $\gamma = 0.5$ (black) or fixed $d_{Pt} = 1.2$ nm (red).

interface roughness becomes more significant as the multilayer period decreases because the ratio of the interface roughness to the multilayer period directly affects the reflectivity through the Debye–Waller factor (DWF) [94]. One reason for interface roughness is crystallization during multilayer deposition [92,93]. In a short-period multilayer (shorter than several nanometers), the metal layer, *e.g.*, the Pt layer, retains its amorphous structure. However, Pt atoms tend to form closely packed structures and are covered by surfaces with relatively low surface energies, such as (111) surfaces, which is the most significant cause of interface roughening. Crystalline metals can generally be made amorphous by the addition of non-metals or metalloids such as B, C, P, or Si [95]. Thus, in this section, we address whether the doping of C atoms into Pt layers at concentrations of 1–15 v/v % can effectively reduce their roughnesses; we also discuss the controllability that can be achieved by this method.

### 5.2.1 Roughness Improvement by Crystallization Suppression[96]

Pure Pt and C-doped Pt (PtC) films were fabricated by DC magnetron sputtering. The Pt and PtC films were deposited on Si (100) substrates. To confirm the crystallization suppression, the surface morphologies of the Pt and PtC films were measured by an atomic force microscope (AFM, Digital Instruments D3100) in air. Scan areas of 500 nm × 500 nm and 5 μm × 5 μm were used for both types of film. The thickness of each film was 50 nm; this relatively large thickness was chosen to enhance the difference between the surface roughnesses of the Pt films with and without C-doping. Figure 5.4 presents AFM images of the deposited Pt films with C concentrations of 0–15 v/v %. Figure 5.5 shows the relationship between the RMS roughness of the film surface and the C concentration; the surface roughness decreases with increasing C concentration. A level of C-doping as low as 1 v/v % can reduce the RMS roughness by 0.1 nm. The surface roughness of the PtC film with 15 v/v % C is equivalent to that of the substrate, so the roughness induced by crystallization during deposition is almost completely suppressed.

The X-ray diffraction spectrum of each film was measured using a Cu-Kα X-ray source; the results are shown in Fig. 5.6. The sharp diffraction peak is from the Si substrate, while the X-ray diffraction spectra of the deposited Pt and PtC films have high-intensity peaks at (111) and (222). The films with lower C concentrations are more likely to have their (111) orientations parallel to their surfaces. This result clearly shows that C-doping can effectively suppress Pt crystallization during film deposition.

The grain sizes of the polycrystalline Pt and PtC films were estimated from the widths of their diffraction peaks at (111) by applying the Scherrer equation [97,98],

$$D = \frac{0.9\lambda}{\beta \cos\theta}, \tag{5.1}$$

where $D$ is the grain size, $\lambda$ is the X-ray wavelength, $\beta$ is the line broadening at FWHM in radians, and $\theta$ is the Bragg angle ($\theta$ of Pt(111) is 0.347 rad). The FWHM of the Pt film is 30.1 mrad, which is almost the same as those of the PtC films. The grain size is 5 nm, which is nearly the same as the spatial wavelength of the AFM image shown in Fig. 5.6.

To obtain the electron diffraction patterns and TEM images of the Pt and PtC films, a 10-nm-thick C film was deposited on a NaCl (100) substrate, and 50-nm-thick Pt and PtC films were deposited on this film. Then, the thin film formed on the NaCl substrate was peeled off

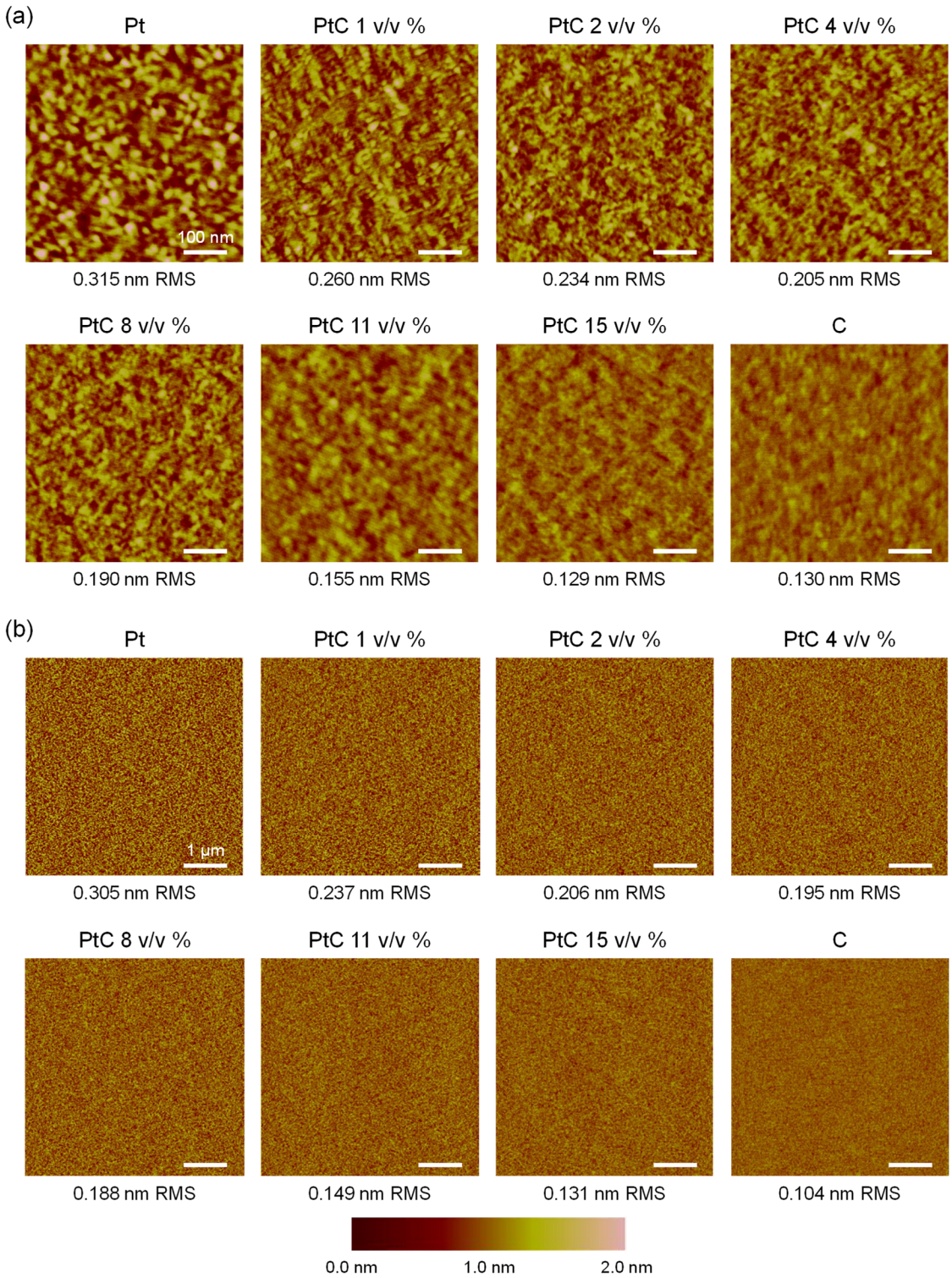


Fig. 5.4. AFM images of surfaces of deposited Pt and PtC films with 0–15 v/v % C. Scanned areas are (a) 500 nm × 500 nm and (b) 5 μm × 5 μm.

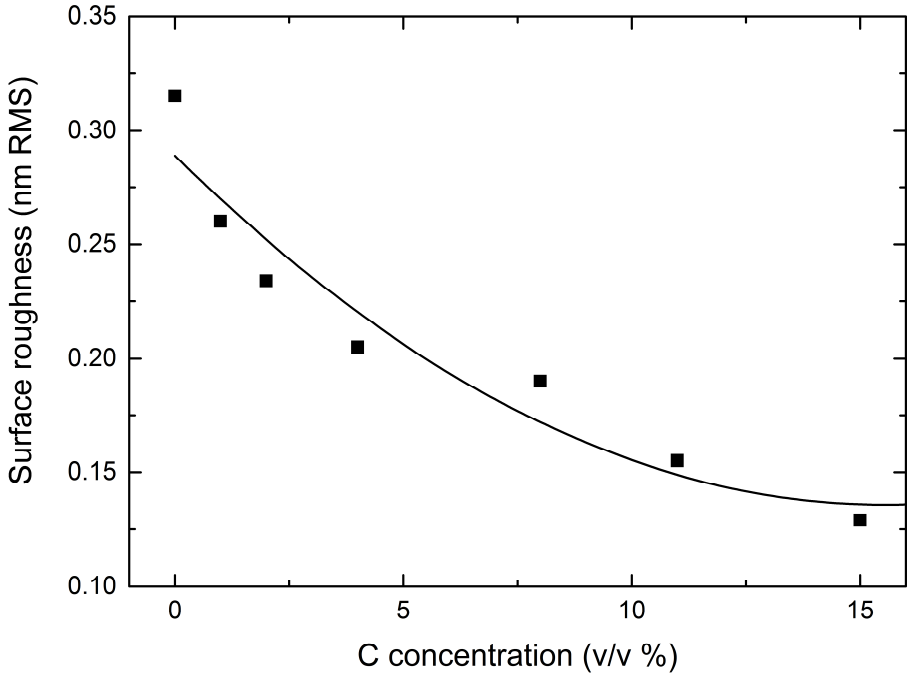


Fig. 5.5. RMS film surface roughness versus C concentration in PtC film.

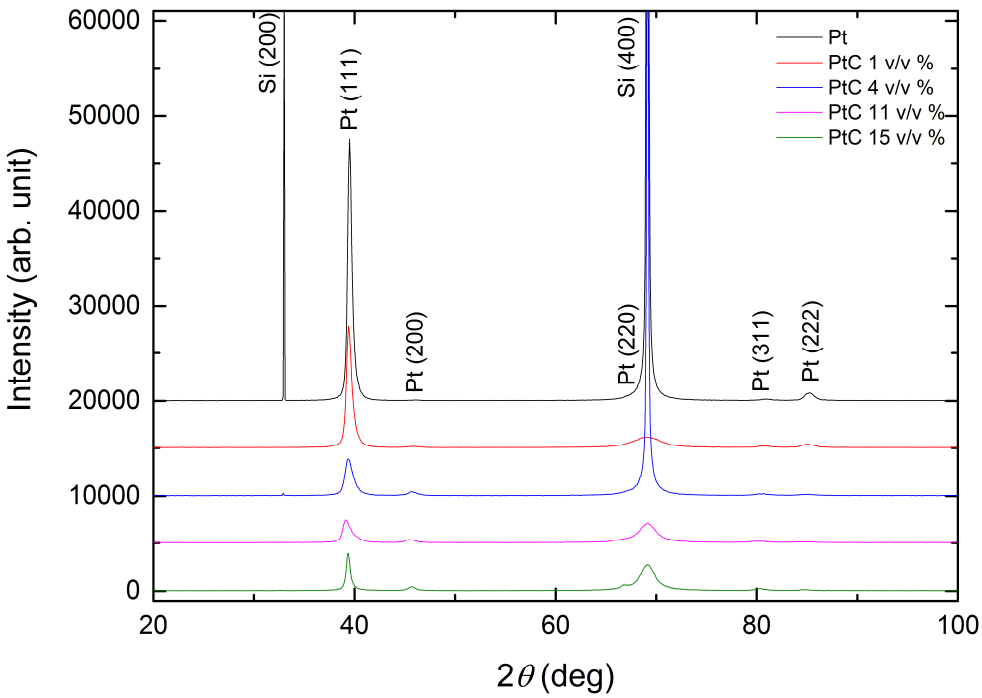


Fig. 5.6. X-ray diffraction spectra of Pt and PtC films.

and placed on the TEM grid. Electron diffraction patterns, bright-field TEM images, and dark-field TEM images were obtained and are shown in Fig. 5.7. The electron diffraction patterns of the deposited Pt and PtC films have significant high-intensity peaks at (220), most likely because Pt has its (111) orientation parallel to its surface. Moreover, the intensity of the (220) peak decreases as the C concentration increases. This result shows that C-doping can effectively suppress Pt crystallization during film deposition. From the bright-field TEM images, it can be seen that the grain size becomes smaller as the C content increases. The dark-field TEM images depict only the grains of Pt (220). The grains of the C-doped samples are smaller than those of the Pt film, and the grains were evenly distributed.

### 5.2.2 X-ray Reflectivity Improvement[99]

The reflectivities of the Pt/C and PtC/C multilayers were compared when $d_{Pt}$ was 1.2 nm. The C concentration in the PtC layer was 4 v/v %, which is sufficient to suppress Pt layer crystallization. The calculated and measured reflectivities are shown in Fig. 5.8, which was obtained using 30 bilayers and an X-ray wavelength of 0.154 nm. The calculated reflectivities of the films are similar. However, the measured reflectivity is higher for the PtC/C multilayer.

The interface roughness of each sample was calculated using the DWF,

$$DWF = \exp\left[-\left(\frac{2\pi m\sigma}{d}\right)^2\right], \tag{5.2}$$

where $m$ is the Bragg index, $d$ is the multilayer period, and $\sigma$ is the RMS interface roughness [94]. The DWF is essentially the relative reflectivity (the ratio of the measured and theoretical values). The calculated interface roughnesses are presented in Fig. 5.9, which shows that the average interface roughness of the PtC/C multilayer is lower than that of the Pt/C multilayer.

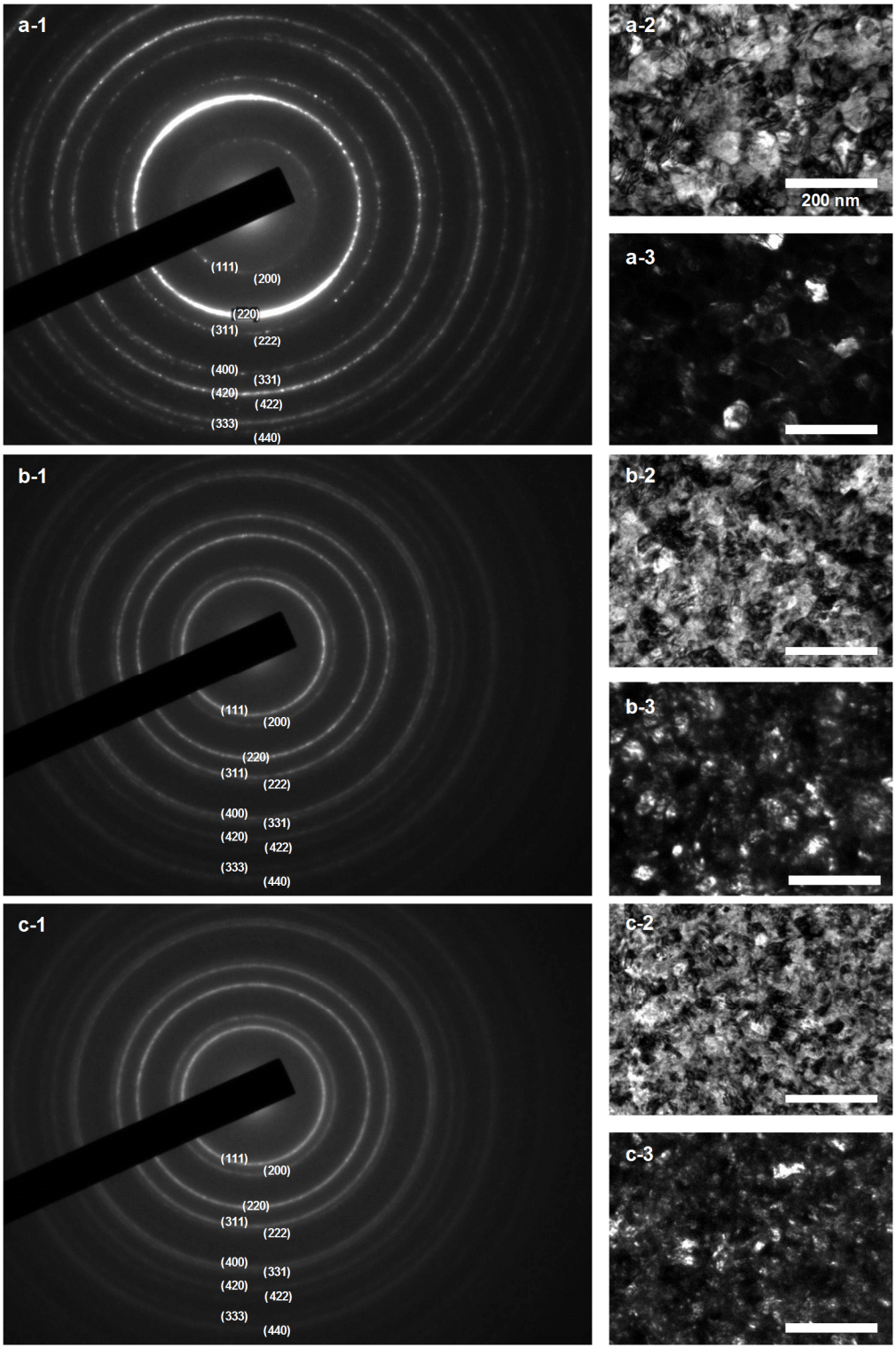


Fig. 5.7. Electron beam diffraction patterns (-1) and bright-field (-2) and dark-field (-3) TEM images of single-layer films. (a), (b), and (c) refer to pure Pt, PtC (3 v/v %), and PtC (11 v/v %) samples, respectively.

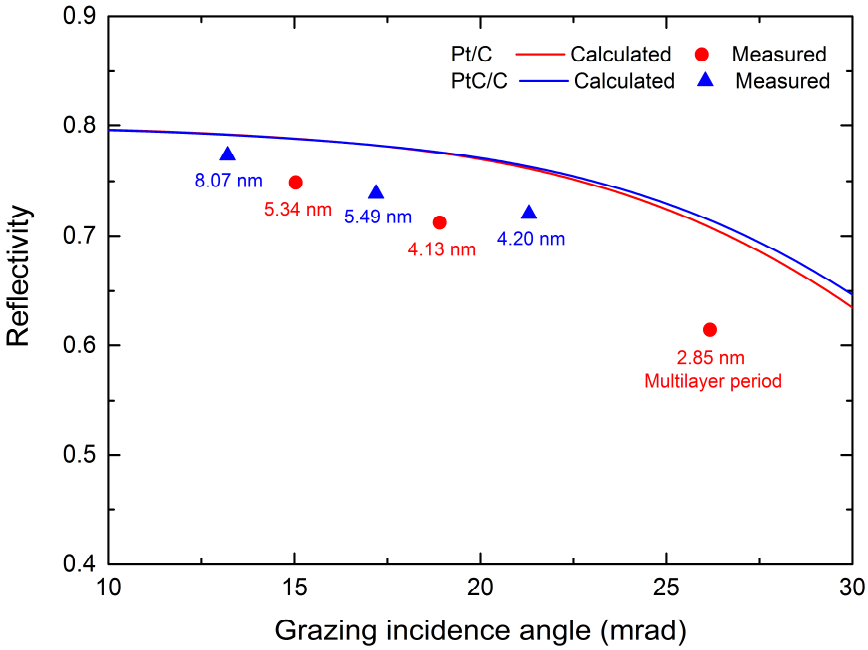


Fig. 5.8. Calculated and measured X-ray reflectivities of Pt/C and PtC/C multilayers using $N = 30$, Pt (or PtC) thickness of 1.2 nm, and C concentration in PtC of 4 v/v %.

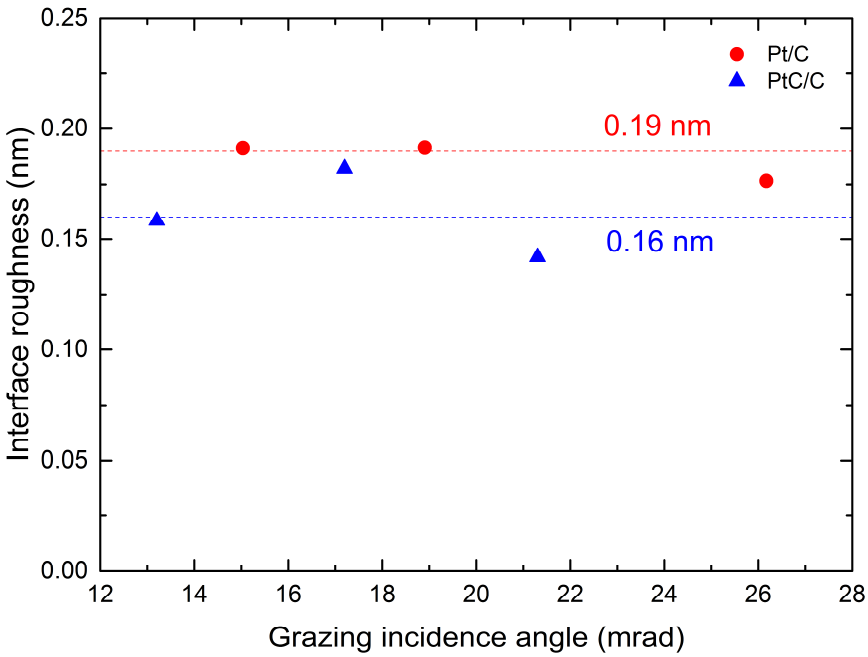


Fig. 5.9. Interface roughnesses calculated using DWF for Pt/C and PtC/C multilayers.

## 5.3 Summary

To develop a Pt/C multilayer film with improved X-ray reflectivity, we evaluated the effects of Pt layer thinning and C-doping of the Pt layers.

Pt layer thinning effectively reduced the absorption of hard X-rays by the Pt, especially in the long-period multilayers. In this study, the critical Pt layer thickness was determined by using the X-ray reflectivity of the Pt/C multilayer because it is not possible to reduce the Pt layer thickness indefinitely. We determined the critical Pt layer thickness to be ~1.2 nm, at which the theoretically obtainable X-ray reflectivity was increased, and the measured X-ray reflectivity was increased by ~10%.

Since admixtures of metals and nonmetals, or metalloid elements such as C, generally suppress the crystallization of metal films during deposition, we compared single-layer films of pure Pt to single-layer films of C-doped Pt to evaluate the effectiveness of C-doping in suppressing Pt crystallization. C concentrations ranging from 0 v/v % to 15 v/v % were employed, and the surface roughnesses, X-ray diffraction spectra, and electron beam diffraction spectra of the resulting films were measured. We concluded that the surface roughness decreased with increasing C concentration in the Pt layers and that the Pt crystallization during deposition was also suppressed; these factors can be used to achieve improvements in interface quality and reflectivity. Furthermore, we found that C-doping effectively increased the reflectivity of the total X-ray reflection optical system.

# Chapter 6

# NANOFOCUSING OF X-RAY FREE-ELECTRON LASERS

*The use of focusing optics enables enhancement of X-ray intensity, which can expand the range of applications of XFELs. At SACLA [17], a 50 nm focusing beam with a power density of $10^{20}$ W/cm$^2$ has been achieved using total reflection mirror optics [18]. To achieve higher power densities of ~$10^{22}$ W/cm$^2$, multilayer mirrors have been developed for use as XFEL sub-10-nm focusing optics. To investigate XFEL nanobeam focusing, a wavefront measurement method was developed. Using this method, correct mirror alignment was achieved, and the residual surface shape errors of the mirror optics were measured. Then, the XFEL sub-10-nm focusing optics were commissioned at SACLA.*

## 6.1 XFEL Sub-10-nm Focusing Optics and Focusing Strategy

The optical configuration and parameters of a sub-10-nm focusing system are shown in Fig. 6.1 and Table 6.1, respectively. To achieve a sub-10-nm spot size, a shorter focal length and larger numerical aperture are theoretically required. However, short focal lengths have several demerits, such as the risk of incurring debris from samples and limited application variations. For the focal length to be sufficiently long, the incident beam must be several millimeters in diameter. However, such a large numerical aperture cannot be obtained by using the conventional single-stage focusing system due to the small divergence of the XFEL beam,

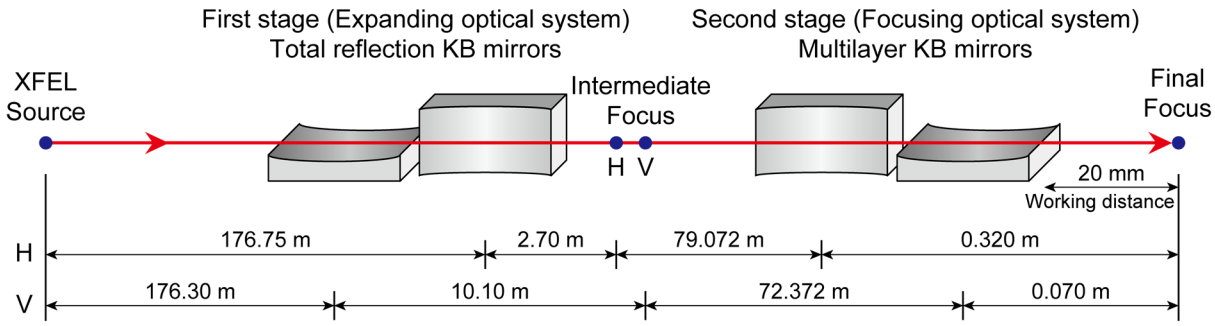


Fig. 6.1. Schematic of optical configuration of two-stage XFEL sub-10-nm focusing system.

Table 6.1. Optical parameters of XFEL sub-10-nm focusing system at SACLA.

| | **Upstream focusing mirrors** | | **Downstream focusing mirrors** | |
|---|---|---|---|---|
| | **Vertical direction** | **Horizontal direction** | **Horizontal direction** | **Vertical direction** |
| Surface shape | Elliptical cylinder | Elliptical cylinder | Elliptical cylinder | Elliptical cylinder |
| Substrate material | Quartz | Quartz | Quartz | Quartz |
| Coating material | None | None | $[Pt/C]_{30}$ | $[Pt/C]_{30}$ |
| Coating thickness (nm) | None | None | 93.6–217.5 | 86.1–273.0 |
| Substrate size ($mm^3$) | 400×50×50 | 400×50×50 | 380×50×50 | 100×50×50 |
| Grazing incidence angle on mirror center (mrad) | 1.50 | 1.50 | 14.6 | 13.2 |
| Focal length (m) | 10.10 | 2.70 | 0.320 | 0.070 |
| Distance from source (m) | 176.30 | 176.75 | 79.072 | 72.372 |
| Semi-major axis (m) | 93.200 | 89.725 | 39.696 | 36.221 |
| Semi-minor axis (mm) | 63.296 | 32.768 | 73.438 | 29.710 |

which is on the order of microradians. At SACLA, which is a compact facility, the maximum beam size is ~500 μm (FWHM) at the farthest experimental hutch. To overcome this limitation, this focusing system has adopted a two-stage reflective focusing system, which was also adopted for the 50 nm focusing at SACLA. In the first (upstream) stage, non-coated total reflection KB mirrors are used to pre-focus and expand the incident beam. In the second (downstream) stage, multilayer coated KB mirrors focus the expanded beam. The geometric reduction ratios of the horizontal and vertical directions are 1/16175.8 and 1/18046.9, respectively. Therefore, if the XFEL source size is 100 μm (FWHM), the obtainable spot size becomes 6.2 nm (H) × 5.5 nm (V). Then, the theoretically obtainable diffraction-limited focal spot size is 5.3 nm (H) × 4.2 nm (V) at a photon energy of 9.1 keV, which was calculated by using wave-optics analysis. A photon energy of 9.1 keV was used to enable the application of nonlinear phenomena [20] for optical system alignment, such as astigmatism, and to confirm the focusing power density. The calculated focusing beam waists and profiles of the horizontal and vertical directions are shown in Figs. 6.2 and 6.3, respectively.

The grazing incidence angle and multilayer period of the sub-10-nm optics have the distributions shown in Fig. 6.4. The grazing incidence angle ranges of the second KB mirrors are 11.58–22.88 mrad (H) and 10.09–24.68 mrad (V). These grazing incidence angles significantly exceed the critical angle of Pt at which total reflection occurs (8.97 mrad) at a photon energy of 9.1 keV. In this optical design, the multilayer mirror is essential. The required accuracy of total multilayer film thickness is the same as that of the mirror shape, ~1 nm (PV), as was described in Chapter 3. The multilayer period ranges were calculated to be 3.12–7.25 nm (H) and 2.87–9.10 nm (V) by using Eq. (2.6). The ratio of the thicknesses of the Pt and C layers was chosen to be 1:1 to facilitate phase control of the reflected beam. A high-reflectivity C-doped Pt/C multilayer, which was introduced in Chapter 5, will be adopted for the second commissioning because the purpose of the first commissioning was primarily to measure the shape errors of the focusing mirrors.

Figure 6.5 shows the calculated multilayer X-ray reflectivity distribution for an interface roughness of 0.2 nm (RMS). The X-ray reflectivity continually increases towards its saturation value with increasing number of multilayers. Moreover, uniform and high X-ray reflectivity is evident across the entire mirror surface. However, practically, it is desirable to select the minimum number of multilayers within the range capable of obtaining a certain degree of

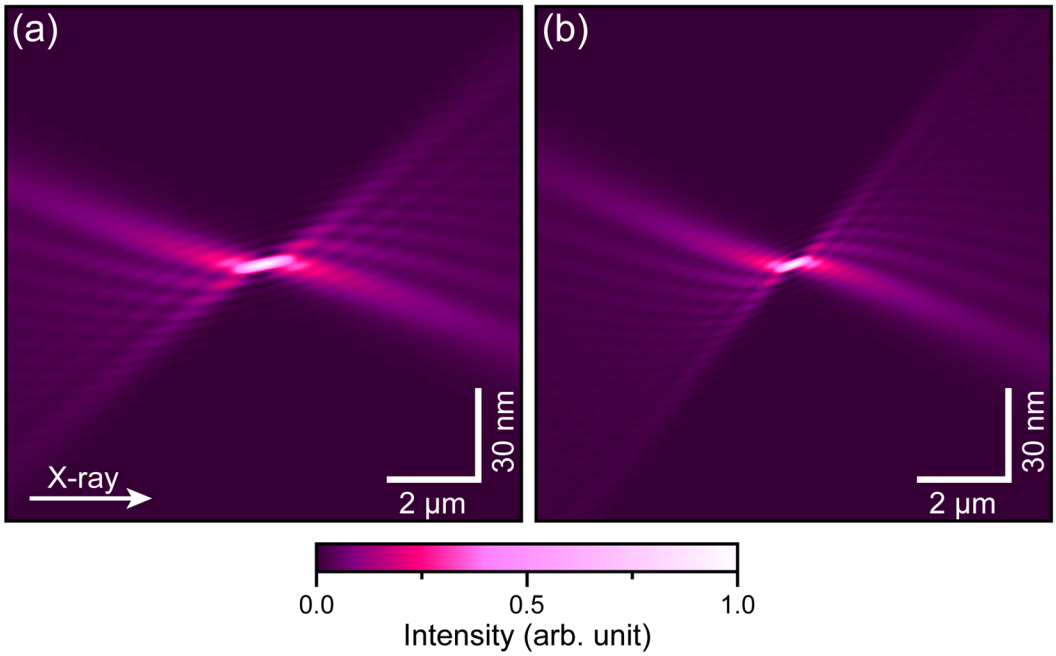


Fig. 6.2. Calculated (a) horizontal and (b) vertical focusing beam waists.

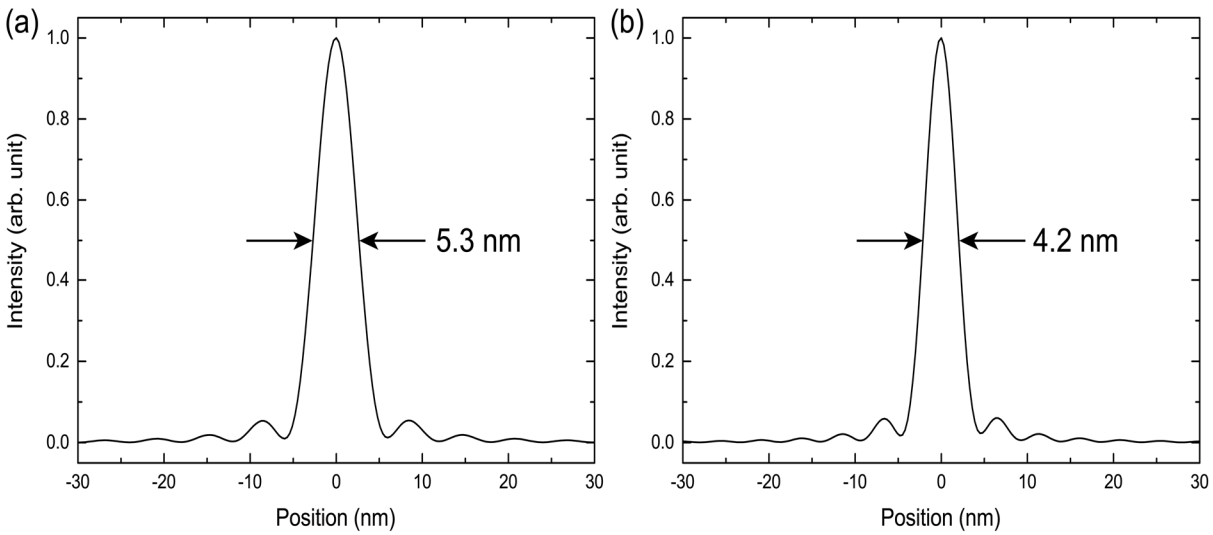


Fig. 6.3. Calculated (a) horizontal and (b) vertical focusing beam profiles.

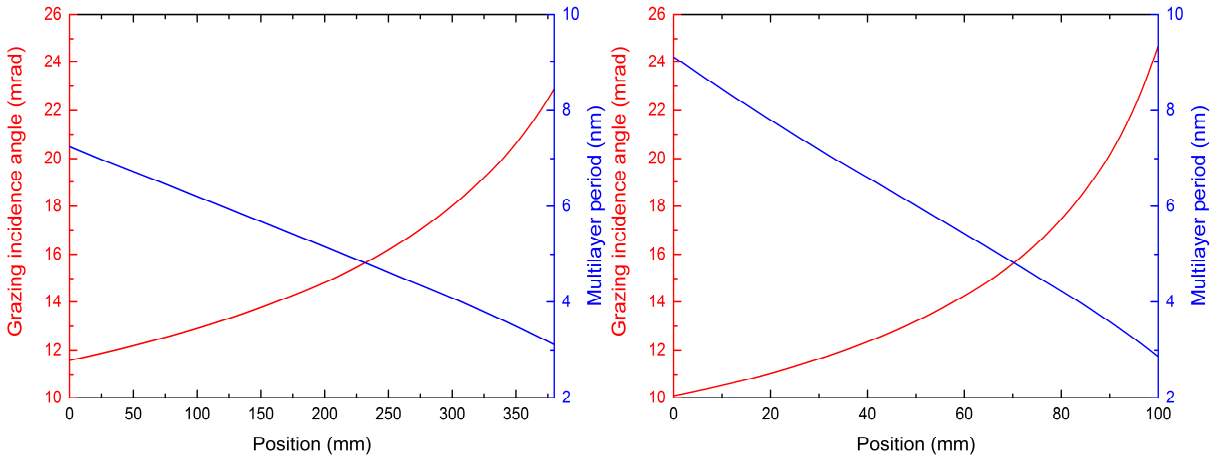


Fig. 6.4. Grazing incidence angle and multilayer period distributions of (a) horizontal and (b) vertical direction focusing mirrors.

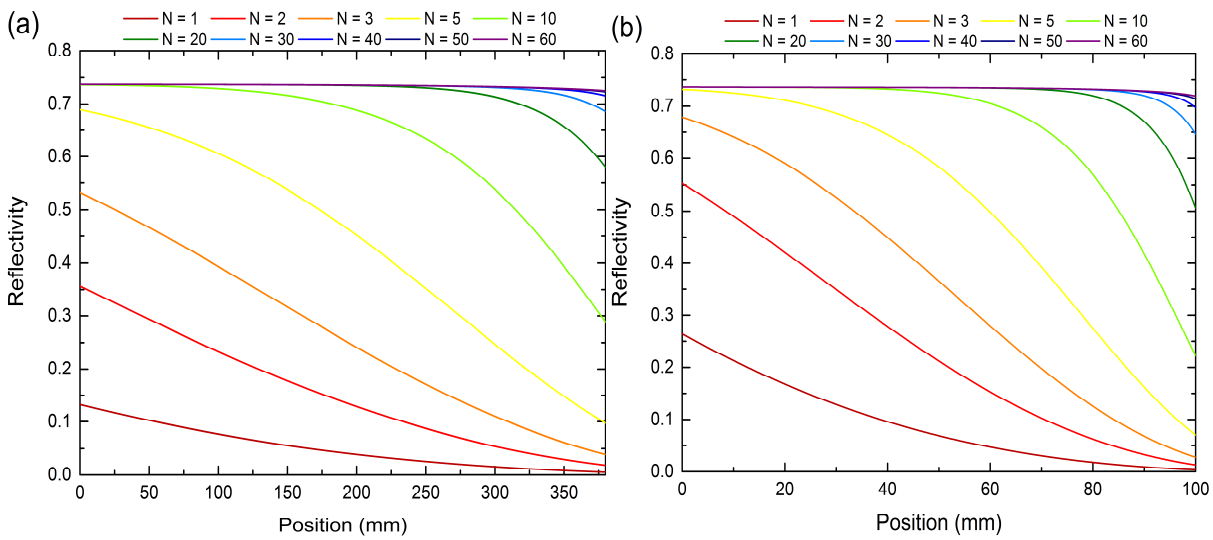


Fig. 6.5. X-ray reflectivity distributions of (a) horizontal and (b) vertical direction focusing mirrors.

uniformity and high reflectance from the entire mirror surface. Multilayer films with fully saturated reflectivity may have adverse effects, such as increasing the film stress and the shape error of the outermost surface due to the increased amount of film and changes in the deposition rate resulting from increased deposition time. We chose to use 30 multilayers based on the simulation results to obtain the reflectivity of 99.5% to the saturation value.

In this sub-10-nm focusing system, an at-wavelength wavefront measurement method, which will be described in the next section, was used to measure the final surface shape error, because it would have been difficult to define the absolute shape errors of the second KB mirrors by using only *ex-situ* measurements. The at-wavelength wavefront measurement method is an *in-situ* measurement method and is useful for determining the shape error, which degrades the focusing. In the first commissioning, the final shape error will be measured by using the X-ray wavelength that is actually used. Then, as shown in Fig. 6.6, the error will be corrected by using differential deposition on the surfaces of the second KB mirrors, because the repeatability of the multilayer deposition and the accuracy of the differential deposition are sufficiently high, as mentioned in Chapter 4. Finally, ideal sub-10-nm focusing will be achieved by using shape-error-corrected multilayer KB mirrors.

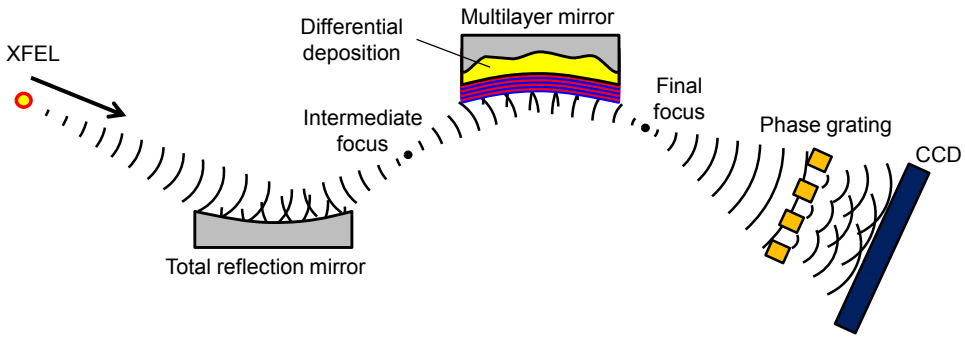


Fig. 6.6. Schematic of XFEL sub-10-nm focusing strategy.

## 6.2 Measurement of Focused X-ray Wavefront

The achievable focal spot size is significantly degraded by mirror shape errors and grazing incidence angle misalignment. For sub-10-nm focusing optics, to satisfy Rayleigh's criterion, the mirror shape and grazing incidence angle errors must not exceed 1 nm (PV) and 0.1 μrad, respectively. Generally, the alignment accuracy is evaluated by monitoring the beam profile using knife-edge scanning methods [100,101]. In this way, the alignment is optimized by an iterative procedure of beam profiling and grazing incidence angle adjustment. This procedure is very time-consuming and frequently introduces significant profiling error due to shape imperfections and/or vibrations of the scanned object. Accordingly, the grazing incidence angle alignment often determines the achievable focal spot size. To evaluate XFEL nanofocusing, a shot-by-shot method is essential to reduce the influence of focal position fluctuations during beam profiling.

To meet this requirement, we used single-grating interferometry [102–116], based on the Talbot effect [117]. Therefore, we tested the sensing capability of the coma aberration generated by the grazing-incidence-angle error of a focusing mirror. A schematic of the single-grating interferometer system is shown in Fig. 6.7, and the phase grating parameters are listed in Table 6.2.

Table 6.2. Phase grating parameters.

| **Parameters** | |
|---|---|
| Material | Tantalum |
| Thickness | 2.25 μm |
| Pitch | 3.0μm |
| Phase shift | $\lambda/2$ (at 9.1 keV) |
| Transmission | 80.5% (at 9.1 keV) |

The energy of the X-rays was 9.1 keV. A tantalum phase grating (3.0 μm pitch; NTT Advanced Technology Corporation) fabricated on a thin SiC membrane (thickness <1 μm) was used, and the grating thickness (2.25 μm) was chosen such that the grating would behave as a $\pi/2$ phase

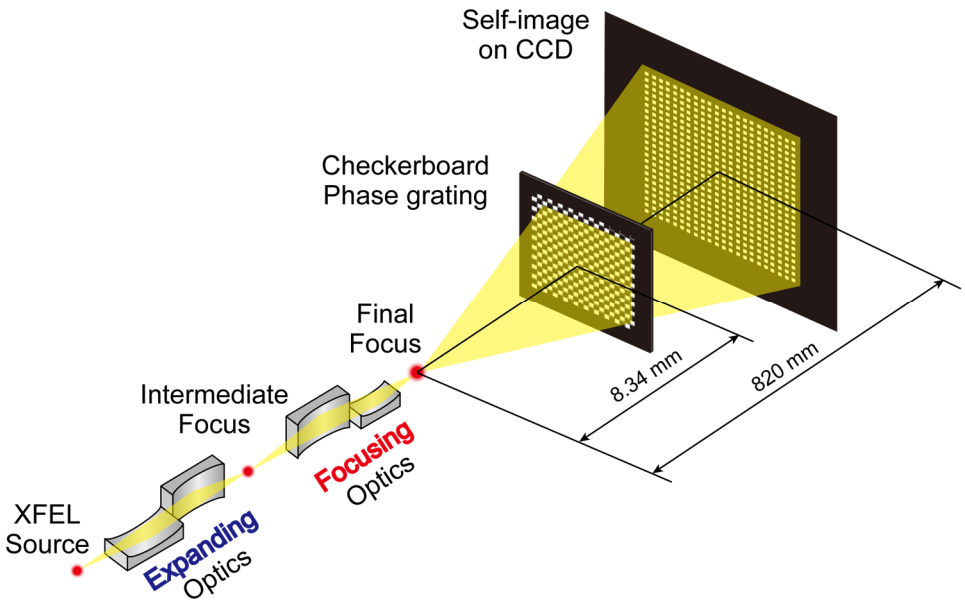


Fig. 6.7. Schematic of single-grating interferometer system.

shifter for 9.1 keV X-rays. The grating was placed 8.34 mm downstream from the final focal point. The formed self-image was recorded by a charge-coupled device (CCD) camera (C9300-124, Hamamatsu Photonics) placed 820 mm downstream of the final focal point. The effective pixel size and field of view of the camera were 9.0 μm and 36.00 mm × 24.05 mm, respectively. Self-images were obtained by single-shot irradiation.

To detect the coma aberration caused by grazing incidence angle error, we intentionally varied the grazing incidence angle around the optimal angle and measured the resulting wavefront shapes, which are shown in Fig. 6.8. To evaluate only the coma aberration induced by the grazing incidence angle error, best-fit quadratic functions were removed from the reconstructed wavefront shapes. The obtained wavefront shapes appear to be cubic functions, with no significant higher-order polynomial components below $\lambda/10$. We measured the PV heights of the cubic functions by changing the grazing incidence angle (pitched at 1 μrad) from -5 μrad to 5 μrad and found that the heights increased with increasing grazing incidence angle error. Figure 6.9 depicts the experimental and calculated results, which agree well. The phase difference at the minimum, for which the grazing incidence angle is optimal, is sufficiently small to satisfy Rayleigh's criterion. Single-grating interferometry is the only available method for evaluating aberration shot-by-shot.

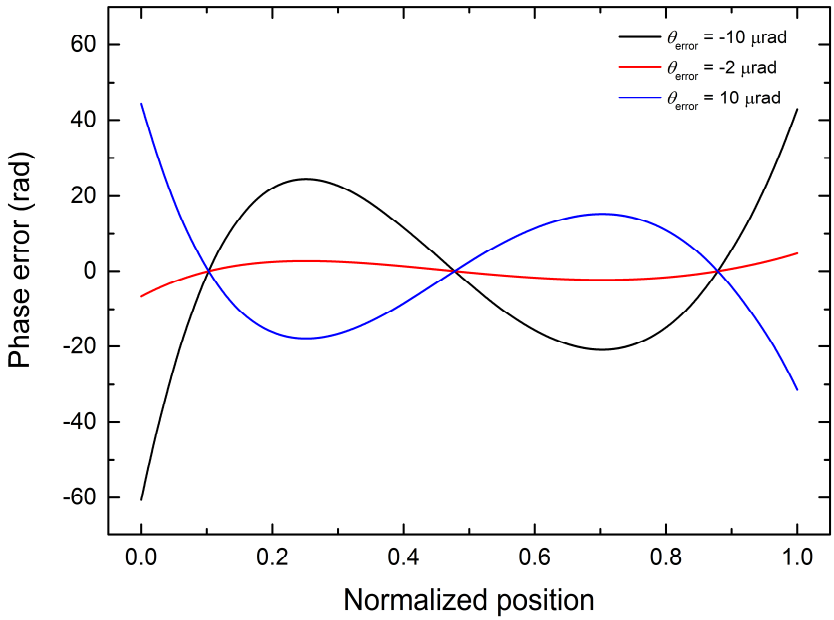


Fig. 6.8. Reconstructed wavefront aberration.

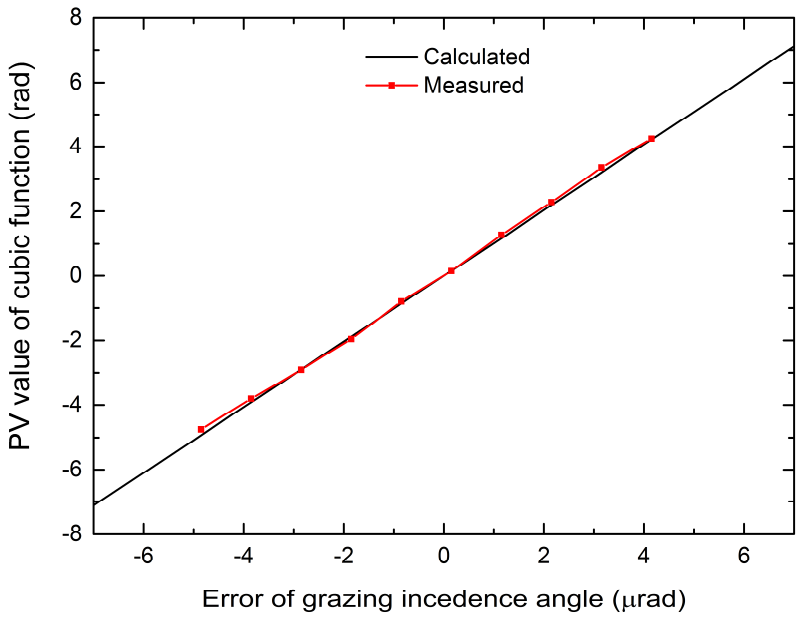


Fig. 6.9. Typical relationship between grazing incidence angle error and phase difference of cubic function (PV) from wavefront shape measured by grating interferometry.

## 6.3 Experimental Evaluation of Multilayers at SPring-8

To measure the mirror shape by using the wavefront measurement method, it is necessary to coat the multilayer on the mirror surface. If the multilayer film has multilayer period error, the relationship between the grazing incidence angle and the multilayer period (Bragg condition) is broken, and the reflectivity is reduced. When the multilayer period error is the range of -4–2%, more than 90% of the designed reflectivity can be achieved, as shown in Fig. 6.10. To evaluate the deposition accuracies of the multilayer films, their reflectivities were measured at SPring-8 BL29XUL using the experimental setup shown in Fig. 6.11. The intensities of the incident and reflected beams were measured by using an ion chamber and a PIN photodiode, respectively. The evaluated multilayer films were the same as those used for XFEL sub-10-nm focusing.

Figure 6.12 presents the measured reflectivities as functions of the grazing incidence angle at an X-ray photon energy of 9.1 keV. Grazing incidence angles that deviated from the ideal grazing incidence angle by between -0.5 mrad and 0.5 mrad were used. The reflectivity of the

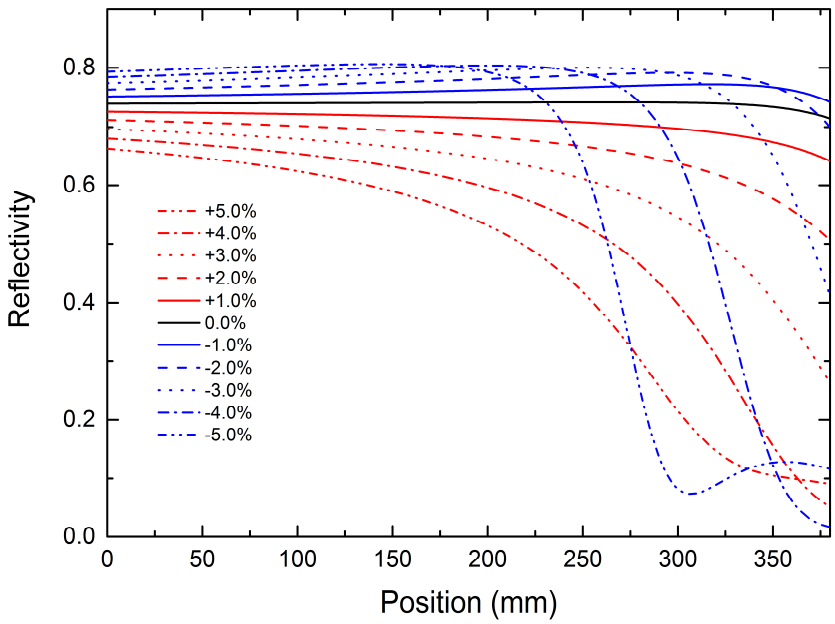


Fig. 6.10. Relationship between multilayer period error and reflectivity.

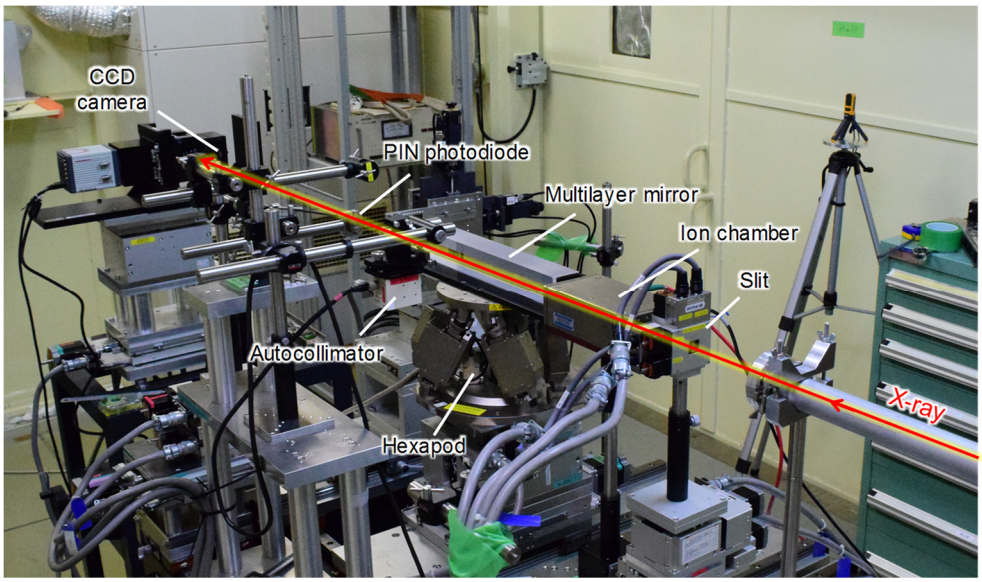


Fig. 6.11. Experimental setup for multilayer evaluation at SPring-8.

horizontal direction focusing mirror increases when the grazing incidence angle is shifted to the negative side, as shown in Fig. 6.12(a), because the multilayer period became longer than the design value. On the other hand, the reflectivity of the vertical direction focusing mirror is the highest at the ideal grazing incidence angle, as shown in Fig. 6.12(b), indicating that the multilayer period was fabricated at a value close to the design value.

Figure 6.13 depicts the measured reflectivities at the ideal grazing incidence angle and at X-ray photon energies ranging from 8.1 keV to 10.1 keV. The lines indicate the reflectivities at an arbitrary mirror position. Figures 6.13(a) and 6.13(b) show that the photon energies at which the horizontal and vertical direction focusing mirrors reflectivities are maximized are 8.909 keV and 9.096 keV, respectively. The corresponding multilayer period errors were determined to be +2.1% (H) and -0.4% (V). Thus, we succeeded in fabricating the multilayer within the allowable error range.

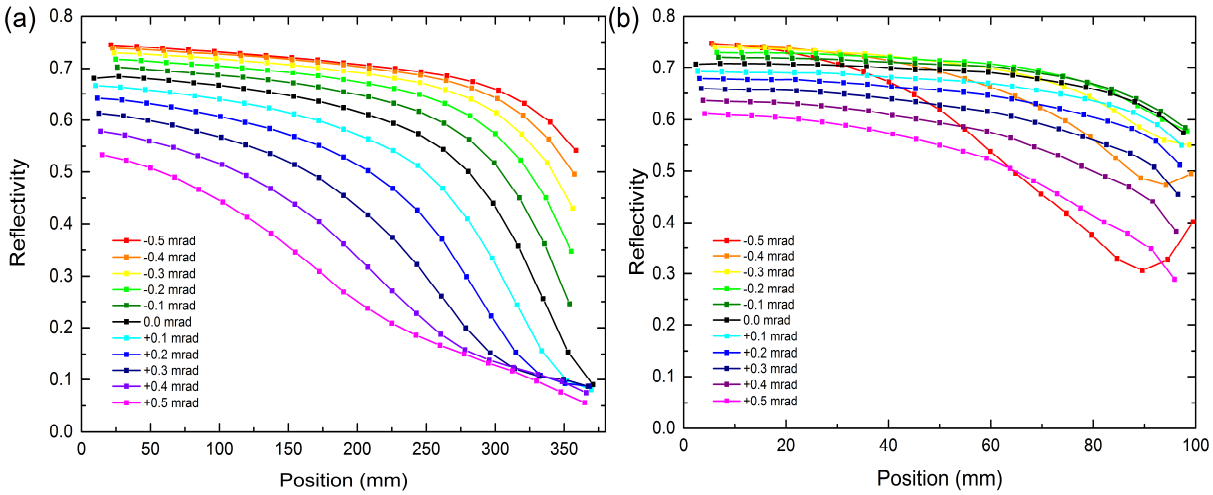


Fig. 6.12. X-ray reflectivities of (a) horizontal and (b) vertical direction focusing mirrors at various grazing incidence angles and X-ray photon energy of 9.1 keV.

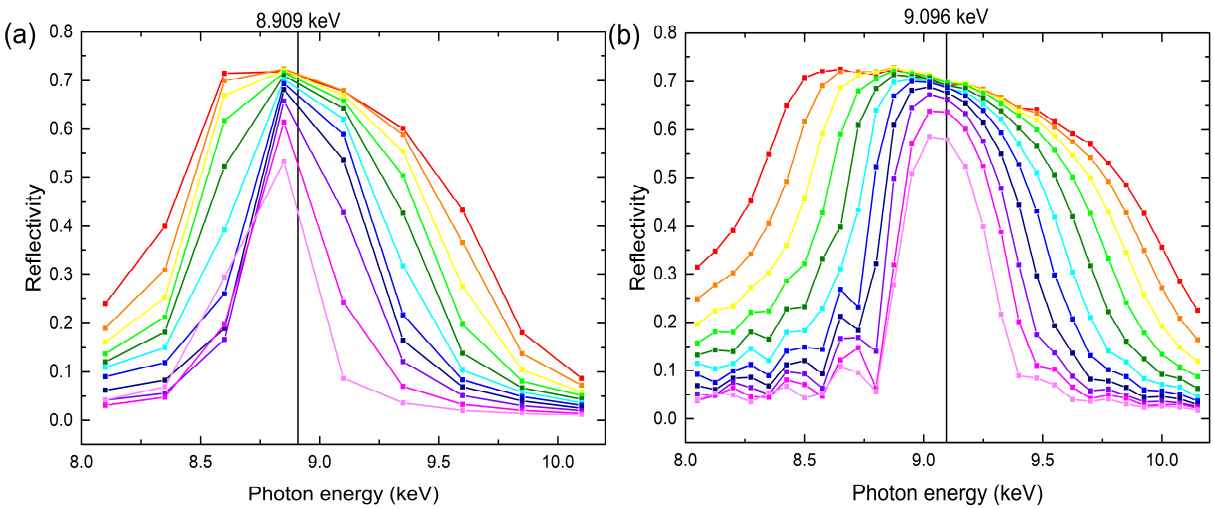


Fig. 6.13. X-ray reflectivities of (a) horizontal and (b) vertical direction focusing mirrors at various X-ray photon energies and ideal grazing incidence angle.

## 6.4 Nanofocusing Experiment at SACLA

The first commissioning of the sub-10-nm XFEL focusing system was performed at SACLA using the setup shown in Fig. 6.14. The mirror and sample chambers were divided to protect the mirror from debris and to increase the range of potential applications.

To investigate the focused beam profiles roughly, wire scan and knife-edge methods were applied, which are capable of micron-order evaluations. These methods are not suitable for sub-10-nm focusing, in which the beam profile would be estimated to be significantly larger because of focal point fluctuations. The measured results are shown in Fig. 6.15. The measured focused-beam size was 65 nm (H) × 49 nm (V) at a photon energy of 9.1 keV; this beam size is larger than the predicted focal spot size. As mentioned above, the knife-edge scan method is not suitable for evaluating sub-10-nm focusing optics. Grating interferometry, using a shot-by-shot method, was employed to understand the exact wavefront aberration. In this case, the cubic function corresponding to the coma aberration was minimized by precisely aligning the grazing incidence angle, and higher-order polynomial elements were extracted to investigate

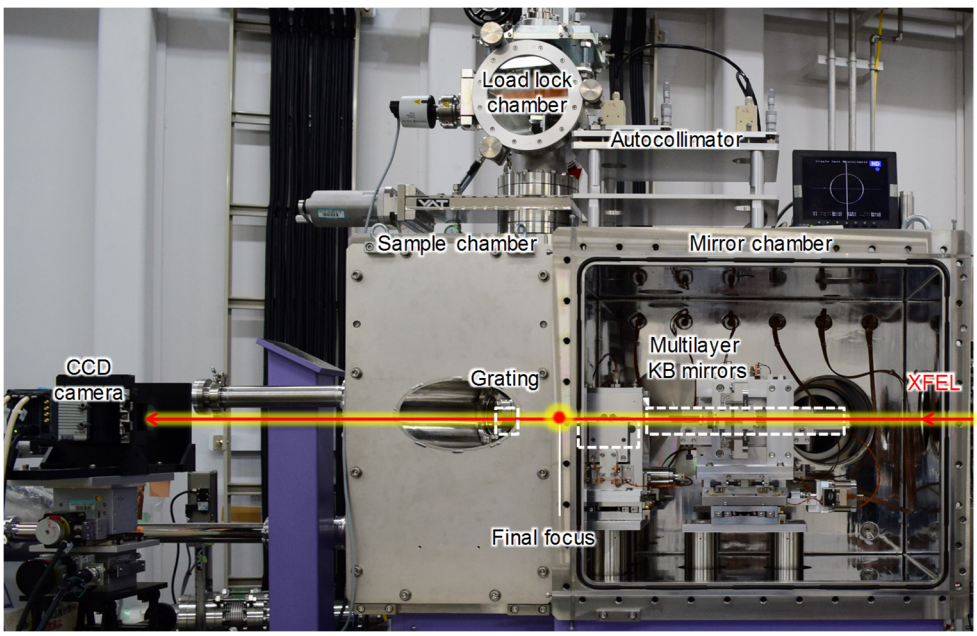


Fig. 6.14. Experimental setup for XFEL sub-10-nm focusing.

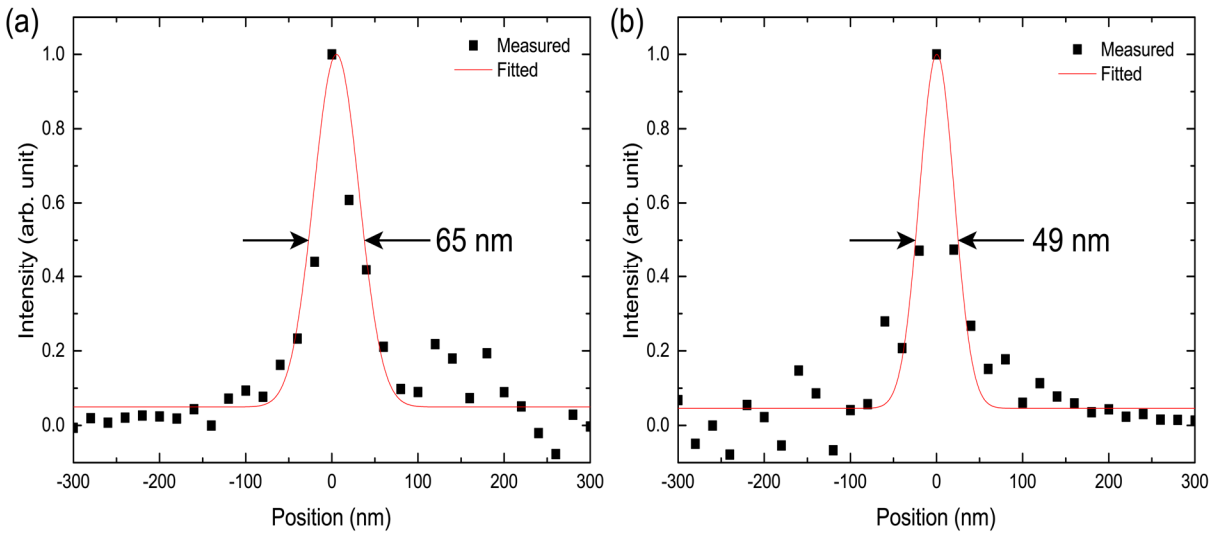


Fig. 6.15. (a) Horizontal and (b) vertical focused-beam profiles measured using wire scan method.

the wavefront error due to mirror shape imperfections. The results of this test are shown in Fig. 6.16. The mirror imperfections led to errors of several radians in both the horizontal and vertical directions, which exceed the errors allowed by Rayleigh's criterion. In two-stage optics for sub-10-nm focusing, the grazing incidence angles of the downstream mirrors are about 10 times larger than those of the upstream mirrors, which means that the shape errors of the downstream mirrors affect the wavefront error 10 times more than those of the upstream mirrors. Accordingly, we concluded that the wavefront error originated from the imperfections of the downstream mirrors. Meanwhile, using the obtained phase errors, the focusing beam waists and profiles were calculated and are shown in Fig. 6.17 and Fig. 6.18, respectively. The theoretically expected beam size is ~10 nm, which is the smallest beam size reported to date in XFEL focusing. Then, in the second commissioning, we endeavor to focus the XFEL to sub-10-nm size with a power density greater than $10^{22}$ W/cm$^2$, by using shape-error-corrected multilayer mirrors.

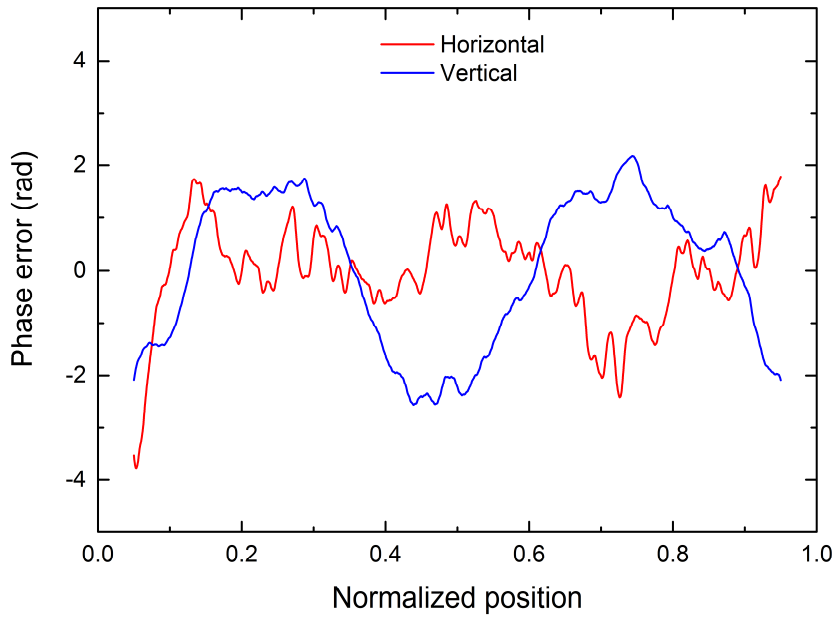


Fig. 6.16. Measured phase errors resulting from shape errors of sub-10-nm focusing mirrors.

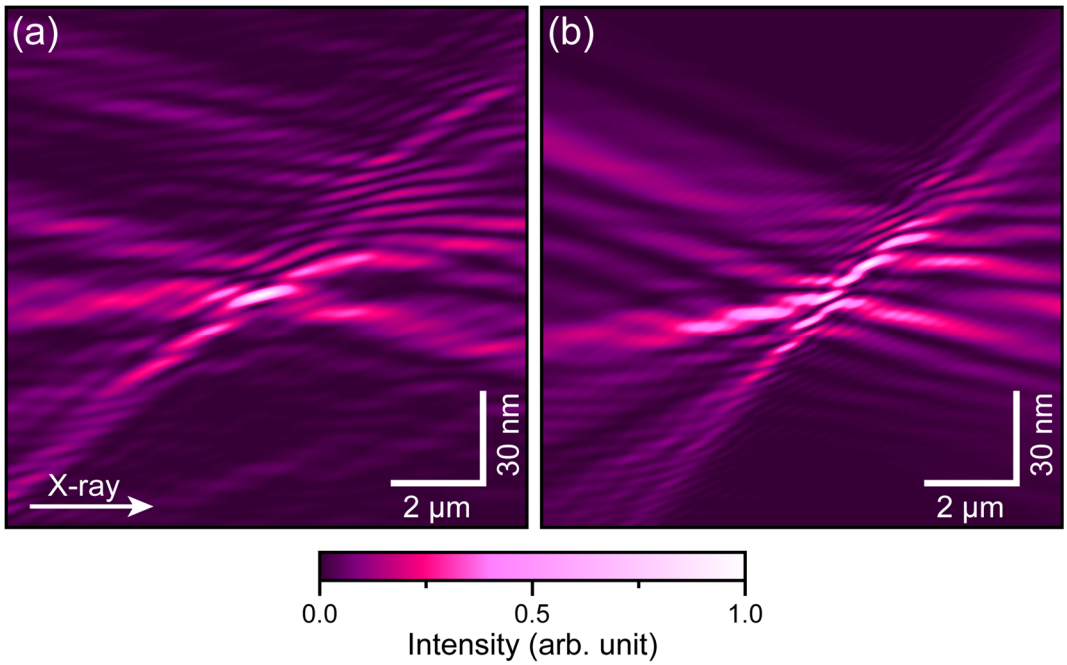


Fig. 6.17. (a) Horizontal and (b) vertical focusing beam waists expected based on measured phase errors.

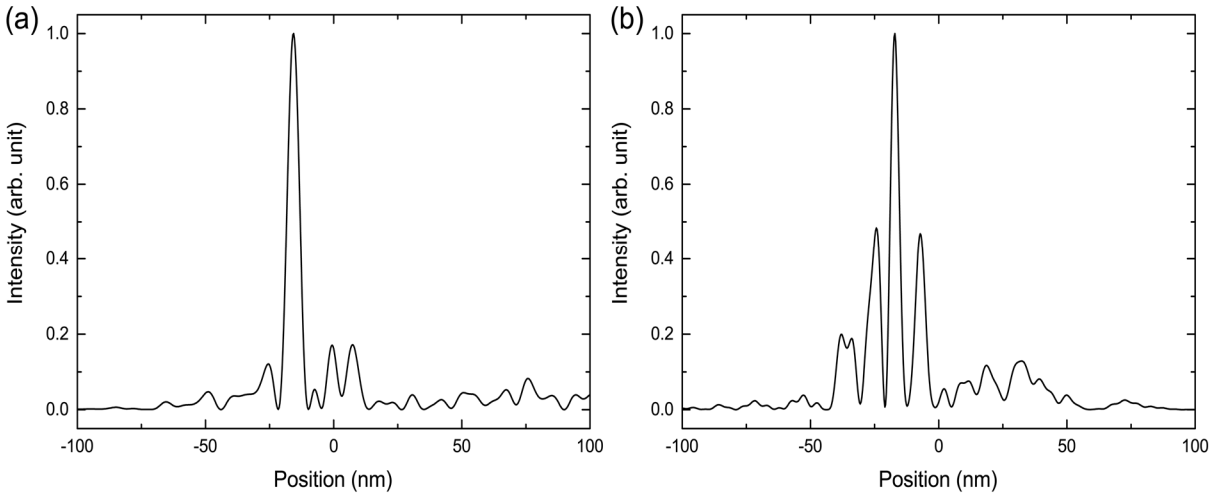


Fig. 6.18. (a) Horizontal and (b) vertical focusing beam profiles expected based on measured phase errors.

## 6.5 Summary

To achieve X-ray fields with higher power densities, sub-10-nm XFEL focusing was developed using a two-stage reflective focusing system. In the second (downstream) stage, multilayer coated KB mirrors were adopted, and the focused XFEL beam profiles were obtained. Using such optics, the theoretically obtainable diffraction-limited focal spot size is 5.3 nm (H) × 4.2 nm (V) at a photon energy of 9.1 keV. To investigate the focused state of the XFEL nanobeam, a wavefront measurement method was developed. In this way, the alignment was optimized by iterative beam profiling and grazing incidence angle adjustment. However, this procedure is very time-consuming and frequently introduces significant error in the beam profile due to shape imperfections and/or scanner vibrations. Accordingly, the grazing incidence angle error often determines the achievable focal-spot size.

The first commissioning of the sub-10-nm XFEL focusing system was performed at SACLA. To investigate the focused beam profiles roughly, wire scan and knife-edge methods were applied. The measured focused-beam size was 65 nm (H) × 49 nm (V), which includes imperfections and scanner vibrations. Therefore, grating interferometry, using a shot-by-shot

method, was employed to understand the exact wavefront aberration. The mirror imperfections led to errors of several radians in both the horizontal and vertical directions. The beam size was theoretically determined to be ~10 nm based on the obtained phase errors, which is the smallest beam size reported to date in XFEL focusing. Then, in the second commissioning, we endeavor to focus the XFEL to sub-10-nm size with a power density greater than $10^{22}$ W/cm$^2$, by using shape-error-corrected multilayer mirrors.

# Chapter 7

# CONCLUSIONS

In this study, to generate extremely intense X-ray fields that can be used to explore nonlinear phenomena in the hard X-ray regime, a sub-10-nm XFEL focusing system was developed using multilayer KB mirror optics. The design of this system required studies of the fabrication and measurement of mirror substrates with steeply curved surfaces, deposition of multilayers with high reflectivities and sufficient X-ray irradiation tolerances, and techniques for single-shot measurement of focused wavefronts. The main conclusions can be summarized as follows.

## XFEL Sub-10-nm Focusing Mirror Fabrication

XFEL sub-10-nm focusing mirrors have steeply curved surfaces that are difficult to measure using conventional shape measurement methods. The minimum radius of curvature is a few meters, and the slope range is several dozen milliradians. Furthermore, the required mirror surface accuracy, or Rayleigh criterion, is ~1 nm (PV). A laser autofocus microscope system was developed to provide measurements at this level of accuracy, featuring a position correction mechanism utilizing three heterodyne interferometers. A repeatability test demonstrated that the apparatus could be consistently adjusted to within 2 nm (PV).

The sub-10-nm focusing mirrors were fabricated using EEM and measured using MSI, RADSI, and the newly developed instrument. The residual shape errors typically obtained after deterministic figuring of the sub-10-nm focusing mirrors were ~3 nm (PV).

## Pt/C Multilayers with XFEL Irradiation Tolerance

In hard X-ray focusing, multilayer mirrors must be used because reflection at high grazing incidence angles is necessary. To fabricate laterally graded multilayer mirrors for X-ray focusing, a thin film deposition system was developed. An arbitrary shape was fabricated using the differential deposition technique to estimate the accuracy of the deposition apparatus. We confirmed that the deposition apparatus was capable of sub-nanometer accuracy, which is sufficiently high for the fabrication of multilayer mirrors and mirror shape modification.

We then evaluated the applicability of Pt/C multilayer films in XFEL focusing. The X-ray reflectivities, surfaces, and cross-sections of the multilayer films were measured to observe the irradiation damage. We measured the damage threshold of a Pt/C multilayer using a 1 μm focused hard XFEL beam with a photon energy of 10 keV and found that the damage threshold of the Pt/C multilayer film, which had a bilayer period of 3 nm, was 0.051 $\mu J/\mu m^2$, indicating that it could be employed in XFEL focusing optics. Moreover, damage to the multilayer was not observed in the conditions in which it was designed to be used. Our calculated value of the threshold atomic dose of the multilayer was similar to that of the bulk material. The obtained threshold should be a useful criterion for designing multilayer optics in sub-10-nm XFEL focusing and related fields.

## Pt/C Multilayers with High X-ray Reflectivities

To develop Pt/C multilayers with improved X-ray reflectivities, we evaluated the effects of Pt layer thinning and C-doping of the Pt layers.

Pt layer thinning effectively reduced the absorption of hard X-rays by the Pt, especially in long-period multilayers. The critical Pt layer thickness of ~1.2 nm was determined by using the X-ray reflectivity of the Pt/C multilayer because it is not possible to reduce the Pt layer thickness indefinitely. With this thickness, the theoretically obtainable X-ray reflectivity was increased, and the measured X-ray reflectivity was increased by ~10%.

Since admixtures of metals and nonmetals, or metalloid elements such as C, generally suppress the crystallization of metal films during deposition, we compared single-layer films of pure Pt to single-layer films of C-doped Pt to evaluate the effectiveness of C-doping in

suppressing Pt crystallization. C concentrations ranging from 0 v/v % to 15 v/v % were used, and the surface roughness, X-ray diffraction spectra, and electron beam diffraction spectra were measured. We concluded that the surface roughness decreased with increasing C concentration in the Pt layers, and that Pt crystallization during deposition was also suppressed, which can explain the observed improvements in interface quality and reflectivity. Furthermore, C-doping effectively heightened the reflectivity of the total X-ray reflection optics.

## XFEL Nanofocusing

To achieve higher power densities, sub-10-nm XFEL focusing was developed using the two-stage reflective focusing system. In the second (downstream) stage, multilayer coated KB mirrors were adopted, and the focused XFEL beam profiles were obtained. Using such optics, the theoretically obtainable diffraction-limited focal spot size is 5.3 nm (H) × 4.2 nm (V) at a photon energy of 9.1 keV. To investigate the focused state of the XFEL nanobeam, a wavefront measurement method was developed. In this way, the alignment was optimized by iterative beam profiling and grazing incidence angle adjustment. However, this procedure is very time-consuming and frequently introduces significant error in the beam profile due to shape imperfections and/or scanner vibrations. Accordingly, the grazing incidence angle error often determines the achievable focal-spot size.

The initial commissioning of the sub-10-nm XFEL focusing system was performed at SACLA. To investigate the focused beam profiles roughly, wire scan and knife-edge methods were applied. The measured focused-beam size was 65 nm (H) × 49 nm (V), which includes imperfections and vibrations of the scanner. Therefore, grating interferometry, using a shot-by-shot method, was employed to understand the exact wavefront aberrations. The mirror imperfections led to errors of several radians in both the horizontal and vertical directions. The beam size was theoretically determined to be ~10 nm based on the obtained phase errors, which is the smallest beam size reported to date in XFEL focusing.

## Prospects

Sub-10-nm XFEL beams with power densities greater than $10^{22}$ W/cm$^2$ will be generated using

shape-error-corrected multilayer mirrors. Such X-ray field intensities will enable the exploration of nonlinear phenomena in the hard X-ray regime. Moreover, further development of the elemental technologies involved can lead to the realization of focusing diameters at the wavelength level. Then, the electromagnetic field power density could possibly reach the Schwinger limit [118] (~$10^{29}$ W/cm$^2$), at which electron and positron pairs are generated from the vacuum. Additionally, in the field of biomolecular imaging, structural analyses of single molecules of protein before destruction may become possible by using single-shot XFEL pulses [119,120].

# BIBLIOGRAPHY


[1] W. C. Röntgen, "Ueber eine neue Art von Strahlen (On a New Kind of Rays)," Sitz. Ber. Phys. Med. Ges. Wuerzb. **9**, 132 (1895).

[2] W. Crookes, "On the Illumination of Lines of Molecular Pressure, and the Trajectory of Molecules," Phil. Trans. R. Soc. Lond. **170**, 135 (1879).

[3] W. Friedrich, P. Knipping, and M. von Laue, "Interferenzerscheinungen bei Röntgenstrahlen," Sitz. ber. Bayer. Akad. Wiss., 303 (1912).

[4] M. von Laue, "Eine quantitative Prüfung der Theorie für die Interferenzerscheinungen bei Röntgenstrahlen," Sitz. ber. Bayer. Akad. Wiss., 363 (1912).

[5] W. H. Bragg and W. L. Bragg, "The Reflection of X-rays by Crystals," Proc. R. Soc. Lond. A **88**, 428 (1913).

[6] J. D. Watson and F. H. C. Crick, "Molecular Structure of Nucleic Acids," Nature **171**, 737 (1953).

[7] J. P. Blewett, "Radiation Losses in the Induction Electron Accelerator," Phys. Rev. **69**, 87 (1946).

[8] F. R. Elder, A. M. Gurewitsch, R. V. Langmuir, and H. C. Pollock, "Radiation from Electrons in a Synchrotron," Phys. Rev. **71**, 829 (1947).

[9] See http://www.lightsources.org/regions for "Synchrotron radiation and free-electron laser facilities of the world" (last accessed January 1, 2016).

[10] D. H. Bilderback, S. A. Hoffman, and D. J. Thiel, "Nanometer spatial resolution achieved in hard x-ray imaging and Laue diffraction experiments," Science **263**, 201 (1994).

[11] Y. Suzuki, A. Takeuchi, H. Takano, and H. Takenaka, "Performance Test of Fresnel Zone Plate with 50 nm Outermost Zone Width in Hard X-ray Region," Jpn. J. Appl. Phys. **44**, 1994 (2005).

[12] C. G. Schroer, O. Kurapova, J. Patommel, P. Boye, J. Feldkamp *et al*., "Hard x-ray

nanoprobe based on refractive x-ray lenses," Appl. Phys. Lett. **87**, 124103 (2005).

[13] O. Hignette, P. Cloetens, G. Rostaing, P. Bernard, and C. Morawe, " Efficient sub 100nm focusing of hard x rays," Rev. Sci. Instrum. **76**, 063709 (2005).

[14] A. Jarre, C. Fuhse, C. Ollinger, J. Seeger, R. Tucoulou *et al*., "Two-dimensional hard x-ray beam compression by combined focusing and waveguide optics," Phys. Rev. Lett. **94**, 074801 (2005).

[15] H. Mimura, H. Yumoto, S. Matsuyama, Y. Sano, K. Yamamura *et al*., "Efficient focusing of hard x rays to 25 nm by a total reflection mirror," Appl. Phys. Lett. **90**, 051903 (2007).

[16] H. C. Kang, H. Yan, R. P. Winarski, M. V. Holt, J. Maser *et al*., "Focusing of hard x-rays to 16 nanometers with a multilayer Laue lens," Appl. Phys. Lett. **92**, 221114 (2008).

[17] T. Ishikawa, H. Aoyagi, T. Asaka, Y. Asano, N. Azumi *et al*., "A compact X-ray free-electron laser emitting in the sub-ångström region," Nature Photon. **6**, 540 (2012).

[18] H. Mimura, H. Yumoto, S. Matsuyama, T. Koyama, K. Tono *et al*., "Generation of $10^{20}$ W $cm^{-2}$ hard X-ray laser pulses with two-stage reflective focusing system," Nat. Commun. **5**, 3539 (2014).

[19] K. Tamasaku, E. Shigemasa, Y. Inubushi, T. Katayama, K. Sawada *et al*., "X-ray two-photon absorption competing against single and sequential multiphoton processes," Nature Photon. **8**, 313 (2014).

[20] H. Yoneda, Y. Inubushi, M. Yabashi, T. Katayama, T. Ishikawa *et al*., "Saturable absorption of intense hard X-rays in iron," Nat. Commun. **5**, 5080 (2014).

[21] H. Yoneda, Y. Inubushi, K. Nagamine, Y. Michine, H. Ohashi *et al*., "Atomic inner-shell laser at 1.5-ångström wavelength pumped by an X-ray free-electron laser," Nature **524**, 446 (2015).

[22] P. Emma, R. Akre, J. Arthur, R. Bionta, C. Bostedt *et al*., "First lasing and operation of an ångstrom-wavelength free-electron laser," Nature Photon. **4**, 641 (2010).

[23] C. David, S. Gorelick, S. Rutishauser, J. Krzywinski, J. Vila-Comamala *et al*., "Nanofocusing of hard X-ray free electron laser pulses using diamond based Fresnel zone plates," Sci. Rep. **1**, 57 (2011).

[24] D. Nilsson, F. Uhlén, A. Holmberg, H. M. Hertz, A. Schropp *et al*., "Ronchi test for characterization of nanofocusing optics at a hard x-ray free-electron laser," Opt. Lett. **37**, 5046 (2012).

[25] A. Schropp, R. Hoppe, V. Meier, J. Patommel, F. Seiboth *et al*., "Full spatial characterization of a nanofocused x-ray free-electron laser beam by ptychographic imaging," Sci. Rep. **3**, 1633 (2013).

[26] H. Yumoto, H. Mimura, T. Koyama, S. Matsuyama, K. Tono *et al*., "Focusing of X-ray free-electron laser pulses with reflective optics," Nature Photon. **7**, 43 (2013).

[27] M. Born and E. Wolf, *Principles of Optics*, 7 ed. (Cambridge University Press, Cambridge, 1999).

[28] P. Kirkpatrick and A. V. Baez, "Formation of Optical Images by X-Rays," J. Opt. Soc. Am. **38**, 766 (1948).

[29] K. Yamashita, M. Watanabe, O. Matsudo, J. Yamazaki, I. Hatsukade *et al*., "Characterization of platinum–carbon, tungsten–silicon, and tungsten–B4C multilayers," Rev. Sci. Instrum. **63**, 1217 (1992).

[30] P. Høghøj, E. Ziegler, J. Susini, A. K. Freund, K. D. Joensen *et al*., "Focusing of hard X-rays with a W/Si supermirror," Nucl. Instrum. Methods Phys. Res. B **132**, 528 (1997).

[31] D. L. Windt, F. E. Christensen, W. W. Craig, C. Hailey, F. A. Harrison *et al*., "Growth, structure, and performance of depth-graded W/Si multilayers for hard x-ray optics," J. Appl. Phys. **88**, 460 (2000).

[32] A. Paul and G. Lodha, "Interface roughness correlation due to changing layer period in Pt/C multilayers," Phys. Rev. B **65**, 245416 (2002).

[33] B. K. Gan, B. A. Latella, and R. W. Cheary, "Fabrication and characterisation of ultra-thin tungsten–carbon (W/C) and platinum–carbon (Pt/C) multilayers for X-ray mirrors," Appl. Surf. Sci. **239**, 237 (2005).

[34] S. M. Al-Marzoug and R. J. W. Hodgson, "Optimization of platinum–carbon multilayer mirrors for hard X-ray optics," Opt. Commun. **268**, 84 (2006).

[35] A. Biswas and D. Bhattacharyya, "Correlation of interface roughness for ion beam sputter deposited W/Si multilayers," J. Appl. Phys. **109**, 084311 (2011).

[36] P. Oberta, Y. Platonov, and U. Flechsig, "Investigation of multilayer X-ray optics for the 6 keV to 20 keV energy range," J. Synchrotron Radiat. **19**, 675 (2012).

[37] H. Jiang, Z. Wang, and J. Zhu, "Interface characterization of $B_4C$-based multilayers by X-ray grazing-incidence reflectivity and diffuse scattering," J. Synchrotron Radiat. **20**, 449 (2013).

[38] C. Morawe, R. Supruangnet, and J. C. Peffen, "Structural modifications in Pd/B4C multilayers for X-ray optical applications," Thin Solid Films **588**, 1 (2015).

[39] J. Als-Nielsen and D. McMorrow, *Elements of Modern X-ray Physics* (John Wiley & Sons, Ltd., 2001).

[40] L. G. Parratt, "Surface Studies of Solids by Total Reflection of X-Rays," Phys. Rev. **95**, 359 (1954).

[41] L. Nevot and P. Croce, "Caractérisation des surfaces par réflexion rasante de rayons X. Application à l'étude du polissage de quelques verres silicates," Rev. Phys. Appl. **15**, 761 (1980).

[42] B. Vidal and P. Vincent, "Metallic multilayers for x rays using classical thin-film theory," Appl. Opt. **23**, 1794 (1984).

[43] D. K. G. de Boer, "Glancing-incidence x-ray fluorescence of layered materials," Phys. Rev. B **44**, 498 (1991).

[44] S. K. Ghose and B. N. Dev, "X-ray standing wave and reflectometric characterization of multilayer structures," Phys. Rev. B **63**, 245409 (2001).

[45] B. N. Dev, A. K. Das, S. Dev, D. W. Schubert, M. Stamm *et al*., "Resonance enhancement of x rays in layered materials: Application to surface enrichment in polymer blends," Phys. Rev. B **61**, 8462 (2000).

[46] H. Kiessig, "Interference of X-rays on thin layers," Ann. Phys. **10**, 769 (1931).

[47] Y. Inubushi, K. Tono, T. Togashi, T. Sato, T. Hatsui *et al*., "Determination of the Pulse Duration of an X-Ray Free Electron Laser Using Highly Resolved Single-Shot Spectra," Phys. Rev. Lett. **109**, 144801 (2012).

[48] Y. Takahashi, A. Suzuki, N. Zettsu, T. Oroguchi, Y. Takayama *et al*., "Coherent diffraction imaging analysis of shape-controlled nanoparticles with focused hard X-ray free-electron laser pulses," Nano Lett. **13**, 6028 (2013).

[49] C. Song, K. Tono, J. Park, T. Ebisu, S. Kim *et al*., "Multiple application X-ray imaging chamber for single-shot diffraction experiments with femtosecond X-ray laser pulses," J. Appl. Cryst. **47**, 188 (2014).

[50] T. Kimura, Y. Joti, A. Shibuya, C. Song, S. Kim *et al*., "Imaging live cell in micro-liquid enclosure by X-ray laser diffraction," Nat. Commun. **5**, 3052 (2014).

[51] R. Xu, H. Jiang, C. Song, J. A. Rodriguez, Z. Huang *et al*., "Single-shot three-

dimensional structure determination of nanocrystals with femtosecond X-ray free-electron laser pulses," Nat. Commun. **5**, 4061 (2014).

[52] H. Fukuzawa, S. K. Son, K. Motomura, S. Mondal, K. Nagaya *et al*., "Deep Inner-Shell Multiphoton Ionization by Intense X-Ray Free-Electron Laser Pulses," Phys. Rev. Lett. **110**, 173005 (2013).

[53] K. Tamasaku, M. Nagasono, H. Iwayama, E. Shigemasa, Y. Inubushi *et al*., "Double Core-Hole Creation by Sequential Attosecond Photoionization," Phys. Rev. Lett. **111**, 043001 (2013).

[54] K. Sakurai, Ed., *Introduction to X-ray Reflectivity* (Kodansha Scientific, Tokyo, 2009).

[55] T. Namioka and K. Yamashita, Ed., *X-ray Imaging Optics* (Baifukan, Tokyo, 1999).

[56] K. Yamauchi, K. Yamamura, H. Mimura, Y. Sano, A. Saito *et al*., "Microstitching interferometry for x-ray reflective optics," Rev. Sci. Instrum. **74**, 2894 (2003).

[57] H. Mimura, H. Yumoto, S. Matsuyama, K. Yamamura, Y. Sano *et al*., "Relative angle determinable stitching interferometry for hard x-ray reflective optics," Rev. Sci. Instrum. **76**, 045102 (2005).

[58] T. Kimura, H. Ohashi, H. Mimura, D. Yamakawa, H. Yumoto *et al.*, "A stitching figure profiler of large X-ray mirrors using RADSI for subaperture data acquisition," Nucl. Instrum. Methods Phys. Res. A **616**, 229 (2010).

[59] P. Z. Takacs, S. Qian, and J. Colbert, "Design of a long trace surface profiler," Proc. SPIE **749**, 59 (1987).

[60] Y. Senba, H. Kishimoto, H. Ohashi, H. Yumoto, T. Zeschke *et al*., "Upgrade of long trace profiler for characterization of high-precision X-ray mirrors at SPring-8," Nucl. Instrum. Methods Phys. Res. A **616**, 237 (2010).

[61] F. Siewert, T. Noll, T. Schlegel, T. Zeschke, and H. Lammert, "The nanometer optical component measuring machine: a new sub-nm topography measuring device for X-ray optics at BESSY," AIP Conf. Proc. **705**, 847 (2004).

[62] K. Becker and E. Heynacher, "M400 - A coordinate measuring machine with 10 nm resolution," Proc. SPIE **802**, 209 (1987).

[63] See http://www.mitakakohki.co.jp/english/industry/mp-3/ for "Laser Probe Unit MP-3 of Mitaka Kohki Co., Ltd." (last accessed January 1, 2016).

[64] Y. Mori, K. Yamauchi, and K. Endo, "Elastic emission machining," Precis. Eng. **9**, 123

(1987).

[65] Y. Mori, K. Yamauchi, K. Yamamura, H. Mimura, A. Saito *et al*., "Development of plasma chemical vaporization machining and elastic emission machining systems for coherent x-ray optics," Proc. SPIE **4501**, 30 (2001).

[66] K. Yamauchi, H. Mimura, K. Inagaki, and Y. Mori, "Figuring with subnanometer-level accuracy by numerically controlled elastic emission machining," Rev. Sci. Instrum. **73**, 4028 (2002).

[67] H. Ohashi, "Surface Metrology of X-ray Optics for Synchrotron Radiation," J. Jpn. Soc. Precis. Eng. **76**, 1239 (2010).

[68] R. A. London, R. M. Bionta, R. O. Tatchyn, and S. Roesler, "Computational Simulations of High Intensity X-Ray Matter Interaction," Proc. SPIE **4500**, 51 (2001).

[69] S. P. Hau-Riege, H. N. Chapman, J. Krzywinski, R. Sobierajski, S. Bajt *et al.*, "Subnanometer-Scale Measurements of the Interaction of Ultrafast Soft X-Ray Free-Electron-Laser Pulses with Matter," Phys. Rev. Lett. **98**, 145502 (2007).

[70] S. P. Hau-Riege, R. A. London, A. Graf, S. L. Baker, R. Soufli *et al.*, "Interaction of short x-ray pulses with low-Z x-ray optics materials at the LCLS free-electron laser," Opt. Express **18**, 23933 (2010).

[71] A. R. Khorsand, R. Sobierajski, E. Louis, S. Bruijn, E. D. van Hattum *et al.*, "Single shot damage mechanism of Mo/Si multilayer optics under intense pulsed XUV-exposure," Opt. Express **8**, 700 (2010).

[72] J. Gaudin, O. Peyrusse, J. Chalupský, M. Toufarová, L. Vyšín *et al.*, "Amorphous to crystalline phase transition in carbon induced by intense femtosecond x-ray free-electron laser pulses," Phys. Rev. B **86**, 024103 (2012).

[73] J. Krzywinski, D. Cocco, S. Moeller, and D. Ratner, "Damage threshold of platinum coating used for optics for self-seeding of soft X-ray free electron laser," Opt. Express **23**, 5397 (2015).

[74] T. Koyama, H. Yumoto, Y. Senba, K. Tono, T. Sato *et al.*, "Investigation of ablation thresholds of optical materials using 1-microm-focusing beam at hard X-ray free electron laser," Opt. Express **21**, 15382 (2013).

[75] T. Koyama, H. Yumoto, K. Tono, T. Sato, T. Togashi *et al.*, "Damage threshold investigation using grazing incidence irradiation by hard x-ray free electron laser," Proc.

SPIE **8848**, 88480T (2013).

[76] T. Koyama, H. Yumoto, K. Tono, T. Togashi, Y. Inubushi *et al.*, "Damage to inorganic materials illuminated by focused beam of X-ray free-electron laser radiation," Proc. SPIE **9511**, 951107 (2015).

[77] A. Aquila, R. Sobierajski, C. Ozkan, V. Hájková, T. Burian *et al.*, "Fluence thresholds for grazing incidence hard x-ray mirrors," Appl. Phys. Lett. **106**, 241905 (2015).

[78] L. Eckertová, *Physics of Thin Films,* 2nd ed. (Plenum Press, New York, 1986).

[79] N. Laegreid and G. K. Wehner, "Sputtering Yields of Metals for Ar+ and Ne+ Ions with Energies from 50 to 600 ev," J. Appl. Phys. **32**, 365 (1961).

[80] J. Kim, A. Nagahira, T. Koyama, S. Matsuyama, Y. Sano *et al.*, "Damage threshold of platinum/carbon multilayers under hard X-ray free-electron laser irradiation," Opt. Express **23**, 29032 (2015).

[81] R. M. Bionta, "Controlling Dose to Low Z Solids at LCLS," LCLS Technical Note No. LCLS-TN-00-3 (2000).

[82] M. Yabashi, A. Higashiya, K. Tamasaku, H. Kimura, T. Kudo *et al.*, "Optics development for Japanese XFEL project," Proc. SPIE **6586**, 658605 (2007).

[83] P. J. Potts, *A Handbook of Silicate Rock Analysis* (Blackie, Glasgow, 1987).

[84] E. J. Kobetich and R. Katz, "Energy Deposition by Electron Beams and δ Rays," Phys. Rev. **170**, 391 (1968).

[85] K. Yamauchi, M. Yabashi, H. Ohashi, T. Koyama, and T. Ishikawa, "Nanofocusing of X-ray free-electron lasers by grazing-incidence reflective optics," J. Synchrotron Radiat. **22**, 592 (2015).

[86] B. L. Henke, E. M. Gullikson, and J. C. Davis, "X-ray interactions : Photoabsorption, Scattering, Transmission," At. Data Nucl. Data Tables **54**, 181 (1993).

[87] J. Kim, T. Koyama, H. Yumoto, A. Nagahira, S. Matsuyama *et al.*, "Damage characteristics of platinum/carbon multilayers under x-ray free-electron laser irradiation," Proc. SPIE **8848**, 88480S (2013).

[88] E. Spiller, *Soft X-Ray Optics* (SPIE Optical Engineering Press, Bellingham, 1994).

[89] C. Morawe, P. Pecci, J. C. Peffen, and E. Ziegler, "Design and performance of graded multilayers as focusing elements for x-ray optics," Rev. Sci. Instrum. **70**, 3227 (1999).

[90] E. Spiller, D. Stearns, and M. Krumrey, "Multilayer x-ray mirrors : Interfacial roughness,

scattering, and image quality," J. Appl. Phys. **74**, 107 (1993).

[91] H. Takenaka, T. Kawamura, Y. Ishii, and S. Asagiri, "Heat resistance of Mo/Si, $MoSi_2$/Si, and $Mo_5Si_3$/Si multilayer soft x-ray mirrors," J. Appl. Phys. **78**, 5227 (1995).

[92] J. Birch, F. Eriksson, G. A. Johansson, and H. M. Hertz, "Recent advances in ion-assisted growth of Cr/Sc multilayer X-ray mirrors for the water window," Vacuum **68**, 275 (2003).

[93] N. Ohnishi, Y. Nonomura, Y. Ogasaka, Y. Tawara, Y. Namba *et al*., "HRTEM analysis of Pt/C multilayers," Proc. SPIE **5168**, 508 (2004).

[94] T. W. Barbee, Jr., "Multilayer for x-ray optics," Proc. SPIE **563**, 2 (1985).

[95] F. E. Luborsky, *Amorphous Metallic Alloys* (Butterworth-Heinemann, London, 1983).

[96] J. Kim, S. Matsuyama, Y. Sano, and K. Yamauchi, "Improvement of Interface Roughness in Platinum/Carbon Multilayers for X-Ray Mirrors," Key Eng. Mater. **523**, 1076 (2012).

[97] P. Scherrer, "Bestimmung der Größe und der inneren Struktur von Kolloidteilchen mittels Röntgenstrahlen," Nachr. Ges. Wiss. Göttingen **2**, 98 (1918).

[98] A. L. Patterson, "The Scherrer Formula for X-Ray Particle Size Determination," Phys. Rev. **56**, 978 (1939).

[99] J. Kim, H. Yokoyama, S. Matsuyama, Y. Sano, and K. Yamauchi, "Improved reflectivity of platinum/carbon multilayers for X-ray mirrors by carbon doping into platinum layer," Curr. Appl. Phys. **12**, S20 (2012).

[100] A. H. Firester, M. E. Heller, and P. Sheng, "Knife-edge scanning measurements of subwavelength focused light beams," Appl. Opt. **16**, 1971 (1977).

[101] Y. Suzuki and F. Uchida, "Hard x-ray microprobe with total-reflection mirrors," Rev. Sci. Instrum. **63**, 578 (1992).

[102] T. Weitkamp, B. Nöhammer, A. Diaz, C. David, and E. Ziegler, "X-ray wavefront analysis and optics characterization with a grating interferometer," Appl. Phys. Lett. **86**, 054101 (2005).

[103] Y. Takeda, W. Yashiro, Y. Suzuki, S. Aoki, T. Hattori *et al*., "X-Ray Phase Imaging with Single Phase Grating," Jpn. J. Appl. Phys. **46**, L89 (2007).

[104] W. Yashiro, Y. Takeda, and A. Momose, "Efficiency of capturing a phase image using cone-beam x-ray Talbot interferometry," J. Opt. Soc. Am. A **25**, 2025 (2008).

[105] A. Diaz, C. Mocuta, J. Stangl, M. Keplinger, T. Weitkamp *et al*., "Coherence and wavefront characterization of Si-111 monochromators using double-grating interferometry," J. Synchrotron Radiat. **17**, 299 (2010).

[106] S. Rutishauser, I. Zanette, T. Weitkamp, T. Donath, and C. David, "At-wavelength characterization of refractive x-ray lenses using a two-dimensional grating interferometer," Appl. Phys. Lett. **99**, 221104 (2011).

[107] H. Wang, K. Sawhney, S. Berujon, E. Ziegler, S. Rutishauser *et al*., "X-ray wavefront characterization using a rotating shearing interferometer technique," Opt. Express **19**, 16550 (2011).

[108] S. Yuan, K. A. Goldberg, V. V. Yashchuk, R. Celestre, W. R. McKinney *et al*., "Cross-check of ex-situ and in-situ metrology of a bendable temperature stabilized KB mirror," Nucl. Instrum. Methods Phys. Res. A **635**, S58 (2011).

[109] S. Berujon and E. Ziegler, "Grating-based at-wavelength metrology of hard x-ray reflective optics," Opt. Lett. **37**, 4464 (2012).

[110] S. Matsuyama, H. Yokoyama, R. Fukui, Y. Kohmura, K. Tamasaku *et al*., "Wavefront measurement for a hard-X-ray nanobeam using single-grating interferometry," Opt. Express **20**, 24977 (2012).

[111] S. Rutishauser, L. Samoylova, J. Krzywinski, O. Bunk, J. Grunert *et al*., "Exploring the wavefront of hard X-ray free-electron laser radiation," Nat. Commun. **3**, 947 (2012).

[112] R. Fukui, J. Kim, S. Matsuyama, H. Yumoto, Y. Inubushi *et al*., "A precision grazing-incidence angle error measurement of a hard x-ray condenser mirror using single-grating interferometry," Synchrotron Radiat. News **26**, 13 (2013).

[113] D. J. Merthe, K. A. Goldberg, V. V. Yashchuk, W. R. McKinney, R. Celestre *et al*., "In situ fine tuning of bendable soft x-ray mirrors using a lateral shearing interferometer," Nucl. Instrum. Methods Phys. Res. A **710**, 82 (2013).

[114] D. J. Merthe, V. V. Yashchuk, K. A. Goldberg, M. Kunz, N. Tamura *et al*., "Methodology for optimalin situalignment and setting of bendable optics for nearly diffraction-limited focusing of soft x-rays," Opt. Eng. **52**, 033603 (2013).

[115] H. Wang, S. Berujon, I. Pape, S. Rutishauser, C. David *et al*., "X-ray wavefront characterization of a Fresnel zone plate using a two-dimensional grating interferometer," Opt. Lett. **38**, 827 (2013).

[116] H. Wang, S. Berujon, I. Pape, S. Rutishauser, C. David *et al*., "At-wavelength metrology using the moiré fringe analysis method based on a two dimensional grating interferometer," Nucl. Instrum. Methods Phys. Res. A **710**, 78 (2013).

[117] H. F. Talbot, "Facts relating to optical science," Philos. Mag. **9**, 401 (1836).

[118] J. Schwinger, "On Gauge Invariance and Vacuum Polarization," Phys. Rev. **82**, 664 (1951).

[119] R. Neutze, R. Wouts, D. van der Spoel, E. Weckert, and J. Hajdu, "Potential for biomolecular imaging with femtosecond X-ray pulses," Nature **406**, 752 (2000).

[120] A. Doerr, "Diffraction before destruction," Nat. Methods **8**, 283 (2011).

# LIST OF PUBLICATIONS


[1] **J. Kim**, A. Nagahira, T. Koyama, S. Matsuyama, Y. Sano, M. Yabashi, H. Ohashi, T. Ishikawa, and K. Yamauchi
"Damage threshold of platinum/carbon multilayers under hard X-ray free-electron laser irradiation"
*Optics Express* **23**(22), 29032–29037 (2015).

[2] T. Koyama, H. Yumoto, K. Tono, T. Togashi, Y. Inubushi, T. Katayama, **J. Kim**, S. Matsuyama, M. Yabashi, K. Yamauchi, and H. Ohashi
"Damage to inorganic materials illuminated by focused beam of X-ray free-electron laser radiation"
*Proceedings of SPIE* **9511**, 951107 (2015).

[3] H. Mimura, H. Yumoto, S. Matsuyama, T. Koyama, K. Tono, Y. Inubushi, T. Togashi, T. Sato, **J. Kim**, R. Fukui, Y. Sano, M. Yabashi, H. Ohashi, T. Ishikawa, and K. Yamauchi
"Generation of $10^{20}$ $Wcm^{-2}$ hard X-ray laser pulses with two-stage reflective focusing system"
*Nature Communications* **5**, 3539 (2014).

[4] R. Fukui, **J. Kim**, S. Matsuyama, H. Yumoto, Y. Inubushi, K. Tono, T. Koyama, T. Kimura, H. Mimura, H. Ohashi, M. Yabashi, T. Ishikawa, and K. Yamauchi
"A Precision Grazing-incidence Angle Error Measurement of a Hard X-ray Condenser Mirror Using Single-grating Interferometry"
*Synchrotron Radiation News* **26**(5), 13–16 (2013).

[5] T. Koyama, H. Yumoto, K. Tono, T. Sato, T. Togashi, Y. Inubushi, T. Katayama, **J. Kim**, S. Matsuyama, H. Mimura, M. Yabashi, K. Yamauchi, and H. Ohashi
"Damage threshold investigation using grazing incidence irradiation by hard X-ray free electron laser"
*Proceedings of SPIE* **8848**, 88480T (2013).

[6] **J. Kim**, T. Koyama, H. Yumoto, A. Nagahira, S. Matsuyama, Y. Sano, M. Yabashi, H. Ohashi, T. Ishikawa, and K. Yamauchi
"Damage characteristics of platinum/carbon multilayers under X-ray free-electron laser irradiation"
*Proceedings of SPIE* **8848**, 88480S (2013).

[7] T. Koyama, H. Yumoto, Y. Senba, K. Tono, T. Sato, T. Togashi, Y. Inubushi, T. Katayama, **J. Kim**, S. Matsuyama, H. Mimura, M. Yabashi, K. Yamauchi, H. Ohashi, and T. Ishikawa
"Investigation of ablation thresholds of optical materials using 1-μm-focusing beam at hard X-ray free electron laser"
*Optics Express* **21**(13), 15382–15388 (2013).

[8] K. Ogi, **J. Kim**, K. Ono, and N. Uda
"Impact damage and residual tensile strength of a CF-SMC composite"
*Advanced Composite Materials* **22**(1), 29–47 (2013).

[9] H. Yumoto, H. Mimura, S. Matsuyama, T. Koyama, Y. Hachisu, T. Kimura, H. Yokoyama, **J. Kim**, Y. Sano, K. Tono, T. Togashi, Y. Inubushi, T. Sato, T. Tanaka, M. Yabashi, H. Ohashi, H. Ohmori, T. Ishikawa, and K. Yamauchi
"Micro-focusing of hard x-ray free electron laser radiation using Kirkpatrick-Baez mirror system"
*Journal of Physics: Conference Series* **425**(5), 052022 (2013).

[10] T. Koyama, H. Yumoto, Y. Senba, K. Tono, T. Sato, T. Togashi, Y. Inubushi, **J. Kim**, T. Kimura, S. Matsuyama, H. Mimura, M. Yabashi, K. Yamauchi, H. Ohashi, and T. Ishikawa
"Damage study of optical substrates using 1-μm-focusing beam of hard X-ray free-electron laser"
*Journal of Physics: Conference Series* **463**, 012043 (2013).

[11] H. Yumoto, H. Mimura, T. Koyama, S. Matsuyama, K. Tono, T. Togashi, Y. Inubushi, T. Sato, T. Tanaka, T. Kimura, H. Yokoyama, **J. Kim**, Y. Sano, Y. Hachisu, M. Yabashi, H. Ohashi, H. Ohmori, T. Ishikawa, and K. Yamauchi
"Focusing of X-ray free-electron laser pulses with reflective optics"
*Nature Photonics* **7**(1), 43–47 (2013).

[12] **J. Kim**, H. Yokoyama, S. Matsuyama, Y. Sano, and K. Yamauchi
"Improved reflectivity of platinum/carbon multilayers for X-ray mirrors by carbon doping into platinum layer"
*Current Applied Physics* **12**(S3), S20–S23 (2012).

[13] **J. Kim**, S. Matsuyama, Y. Sano, and K. Yamauchi
"Improvement of interface roughness in platinum/carbon multilayers for X-ray mirrors"
*Key Engineering Materials* **523–524**, 1076–1079 (2012).

[14] S. Matsuyama, N. Kidani, H. Mimura, **J. Kim**, Y. Sano, K. Tamasaku, Y. Kohmura, M. Yabashi, T. Ishikawa, and K. Yamauchi
"Development of a one-dimensional Wolter mirror for achromatic full-field X-ray microscopy"
*Proceedings of SPIE* **8139**, 813905 (2011).

[15] K. Yamauchi, H. Mimura, T. Kimura, H. Yumoto, S. Handa, S. Matsuyama, K. Arima, Y. Sano, K. Yamamura, K. Inagaki, H. Nakamori, **J. Kim**, K. Tamasaku, Y. Nishino, M. Yabashi, and T. Ishikawa
"Single-nanometer focusing of hard x-rays by Kirkpatrick-Baez mirrors"
*Journal of Physics: Condensed Matter* **23**(39), 394206 (2011).

# LIST OF PRESENTATIONS

**Presentations in International Conferences**

[1] **J. Kim**, A. Nagahira, A. Nishihara, S. Matsuyama, H. Yumoto, T. Koyama, Y. Sano, H. Ohashi, M. Yabashi, T. Ishikawa, and K. Yamauchi
"X-ray mirror surface metrology using optical and at-wavelength techniques for hard XFEL single-nanometer focusing"
*12th International Conference on Synchrotron Radiation Instrumentation (SRI 2015)*, NY Marriott Marquis, New York, NY, USA, July 6–10, 2015 (Poster presentation, THU-P-015)

[2] **J. Kim**, S. Matsuyama, Y. Sano, and K. Yamauchi
"Development of high-precision figure measurement system for x-ray optics using laser focus microscope"
*SPIE Optics + Photonics 2014*, San Diego Convention Center, San Diego, CA, USA, August 17–21, 2014 (Oral presentation, 9160-11)

[3] **J. Kim**, A. Nagahira, S. Matsuyama, T. Koyama, H. Yumoto, Y. Sano, M. Yabashi, H. Ohashi, T. Ishikawa, and K. Yamauchi
"XFEL-induced damage to optical thin film for X-ray mirrors under grazing incidence condition"
*International Workshop on Atomically Controlled Fabrication Technology*, Osaka University Nakanoshima Center, Osaka, Japan, February 5–6, 2014 (Poster presentation, P5)

[4] **J. Kim**, A. Nagahira, S. Matsuyama, R. Fukui, A. Nishihara, T. Koyama, H. Yumoto, Y. Sano, H. Ohashi, S. Goto, M. Yabashi, T. Ishikawa, and K. Yamauchi

"Damage characteristics of platinum/carbon multilayers for hard X-ray free-electron laser focusing"
*The 25th Synchrotron Radiation Users' Workshop & KOSUA meeting*, POSCO International Center, Pohang, Republic of Korea, November 21, 2013 (Poster presentation, PP-10)

[5] **J. Kim**, T. Koyama, H. Yumoto, A. Nagahira, S. Matsuyama, Y. Sano, M. Yabashi, H. Ohashi, T. Ishikawa, and K. Yamauchi
"Damage characteristics of platinum/carbon multilayers under focused X-ray free-electron laser irradiation"
*SPIE Optics + Photonics 2013*, San Diego Convention Center, San Diego, CA, USA, August 25–29, 2013 (Oral presentation, 8848-26)

[6] **J. Kim**, S. Matsuyama, Y. Sano, and K. Yamauchi
"Improvement of interface roughness in Pt/C multilayers for X-ray mirrors"
*14th International Conference on Precision Engineering*, Awaji Yumebutai International Conference Center, Hyogo, Japan, November 8–10, 2012 (Oral presentation, E11)

[7] **J. Kim**, A. Nagahira, S. Matsuyama, Y. Sano, and K. Yamauchi
"Study of Pt/C multilayers for X-ray mirrors improvement of reflectivity"
*Fifth international symposium on atomically controlled fabrication technology*, Osaka University Nakanoshima Center, Osaka, Japan, October 22–24, 2012 (Poster presentation, P33)

[8] **J. Kim**, H. Yokoyama, S. Matsuyama, Y. Sano, and K. Yamauchi
"Reflectivity improvement using PtC/C multilayers for X-ray mirrors"
*Fourth international symposium on atomically controlled fabrication technology*, Osaka University Nakanoshima Center, Osaka, Japan, October 31–November 2, 2011 (Poster presentation, P13)

**Presentation in Domestic Conferences**

[1] **金章雨**, 松山智至, 佐野泰久, 山内和人
"X 線集光ミラー形状測定のための姿勢補正機構を有する三次元測定機の開発"
*2015 年度精密工学会春季大会学術講演会 (2015 JSPE Spring Conference)*, Toyo University, Tokyo, March 17–19, 2015 (Oral presentation, R37)

[2] **金章雨**, 長平良綾香, 西原明彦, 松山智至, 佐野泰久, 山内和人
"Sub-10 nm 集光用 X 線ミラーのための高精度形状計測装置の開発"
*第 28 回日本放射光学会年会放射光科学合同シンポジウム (The 28th Annual Meeting of the Japanese Society for Synchrotron Radiation Research – JSR 15)*, Ritsumeikan University, Shiga, January 10–12, 2015 (Poster presentation, 12P015)

[3] **金章雨**, 長平良綾香, 松山智至, 福井亮介, 西原明彦, 小山貴久, 湯本博勝, 佐野泰久, 大橋治彦, 後藤俊治, 矢橋牧名, 石川哲也, 山内和人
"硬 X 線自由電子レーザーシングルナノ集光用 Pt/C 多層膜の破壊特性評価"
*第 27 回日本放射光学会年会放射光科学合同シンポジウム (The 27th Annual meeting of the Japanese Society for Synchrotron Radiation Research – JSR 14)*, International Conference Center Hiroshima, Hiroshima, January 11–13, 2014 (Oral presentation, 3D002)

[4] **金章雨 (Invited)**, 長平良綾香, 松山智至, 福井亮介, 西原明彦, 小山貴久, 湯本博勝, 佐野泰久, 矢橋牧名, 大橋治彦, 石川哲也, 山内和人
"硬 X 線ナノ集光ミラー用 Pt/C 多層膜の作製と評価"
Satellite Meeting of the 12th Symposium on X-ray Imaging Optics,
*X線ナノ集光技術研究会 2013 (X-ray nano-focusing technology workshop 2013)*, Osaka University Nakanoshima Center, Osaka, November 17, 2013 (Oral presentation, p19-20)

[5] **金章雨**, 長平良綾香, 小山貴久, 湯本博勝, 松山智至, 佐野泰久, 矢橋牧名, 大橋治彦, 石川哲也, 山内和人
"X 線自由電子レーザーを用いた硬 X 線集光用 Pt/C 多層膜の特性評価"

*2013 年度精密工学会秋季大会学術講演会 (2013 JSPE Autumn Conference)*, Kansai University, Osaka, September 12–14, 2013 (Oral & Poster presentations, L37 & P-36)

[6] **金章雨**, 福井亮介, 松山智至, 小山貴久, 湯本博勝, 佐野泰久, 大橋治彦, 後藤俊治, 矢橋牧名, 石川哲也, 山内和人
"X 線自由電子レーザー集光用 Pt/C 多層膜の性能評価"
*第 26 回日本放射光学会年会放射光科学合同シンポジウム (The 26th Annual meeting of the Japanese Society for Synchrotron Radiation Research – JSR 13)*, Nagoya University, Aichi, January 12–14, 2013 (Poster presentation, 14P021)

[7] **金章雨**, 横山光, 松山智至, 佐野泰久, 山内和人
"PtC/C 多層膜を用いた硬 X 線集光用ミラーの反射率改善"
*2012 年度精密工学会春季大会学術講演会 (2012 JSPE Spring Conference)*, Tokyo Metropolitan University, Tokyo, March 14–16, 2012 (Oral presentation, O36)

[8] **金章雨**, 横山光, 松山智至, 佐野泰久, 香村芳樹, 玉作賢治, 矢橋牧名, 石川哲也, 山内和人
"PtC/C 多層膜を用いた X 線集光用ミラーの反射率改善"
*第 25 回日本放射光学会年会放射光科学合同シンポジウム (The 25th Annual meeting of the Japanese Society for Synchrotron Radiation Research – JSR 12)*, Tosu-Shimin-Bunka-Kaikan, Saga, January 6–9, 2012 (Poster presentation, 9P002)

[9] **金章雨**, 横山光, 松山智至, 三村秀和, 佐野泰久, 香村芳樹, 石川哲也, 山内和人
"硬 X 線集光用多層膜ミラーの開発"
*2011 年度精密工学会秋季大会学術講演会 (2011 JSPE Autumn Conference)*, Kanazawa University, Ishikawa, September 20–22, 2011 (Oral presentation, I75)